University of Utrecht

Debye Institute

Cold Atom Nanophotonics Group

An Optical Conveyor for Light-Atom Interaction

Author:
S. Greveling B.Sc.

Supervisors:
B. O. Mussmann M.Sc.
A. J. van Lange M.Sc.
Dr. D. van Oosten

December 22, 2013

Abstract

In the Cold Atom Nanophotonics group, the interaction between ^{87}Rb and surface plasmons will be investigated. For that reason, atoms need to be positioned in the near field of a gold film. This is the most challenging part as the near field extend to a distance of $\sim \lambda/2$ above a sample surface, where λ denotes the wavelength of light. The first step is to trap and cool the atoms using a magneto-optical trap. From this trap the atoms are loaded into a far detuned optical dipole trap. By displacing the focus of this trap towards the sample, the atoms are displaced. When the atoms are directly above the sample they are loaded into a red-detuned optical conveyor, which displaces the atoms towards the sample surface to a height of $\lambda/2$. Using two synchronized pairs of rotating mirrors, the optical conveyor is translated in two-dimensions over the sample surface to position the atoms above the correct structure.

In this thesis we describe the optical dipole trap that we used to trap 2.1×10^5 atoms. We have measured the atomic lifetime in the optical dipole trap for different trap depths. Using a laser power of 10.4 W, we obtained a lifetime of up to 6.4 ± 2.9 s. Our magneto-optical trap contains $(4.0 \pm 0.2) \times 10^{10}$ atoms. We achieved a transfer efficiency from the magneto-optical trap into the optical dipole trap of $\sim 4 \times 10^{-4}$ %. In future experiments this transfer efficiency can be increased by readily implementing changes to the loading procedure of the dipole trap.

For the movement of the atoms towards the sample surface, we will use a red-detuned optical conveyor. In this optical conveyor atoms are trapped at the anti-nodes of a standing wave. To displace these anti-nodes, we give the beam producing the standing wave a slight frequency offset. We tested this method interferometrically. We conclude that we can displace the anti-nodes over a distance of > 2 mm with an accuracy of 150 nm. The accuracy is most likely due to mechanical vibrations. We developed a feedback mechanism to increase the accuracy of the displacement of the anti-nodes.

Finally, we designed a setup for the optical conveyor. This setup includes the translation of the optical conveyor in two-dimensions. It is to be implemented into the experiment.

Contents

1 Introduction

The interesting fields of nano-plasmonics and ultracold atoms have gained great popularity over the past decades. The popularity for nano-plasmonics can be found in its possible applications which have the potential to revolutionize the telecommunications industry [1,2]. The ultracold atoms have been a "hot" topic ever since the first Bose-Einstein condensate was achieved, which in 2001 was awarded with the Nobel Prize in Physics [3]. In 1997 the field was also awarded the Nobel Prize in Physics for the development of methods to cool and trap atoms using laser light [3,4].

In the field of nano-plasmonics, the interaction of light with metal structures on the nanoscale is studied [1, 2]. The coupling between electromagnetic waves and collective charge oscillations give rise to surface plasmon polaritons, which can extend both inside the metal and on the interface of the metal [1,2,5]. What makes these plasmons so interesting is their ability to confine light to nanoscale regions, much smaller than the wavelength of light. By controlling light on the nanoscale, possible applications for nano-plasmonics range from biomedical sensors to plasmon-assisted solar energy conversion [5,6].

In the field of ultracold atoms, optical and magnetic fields are used to trap and cool atoms [3,7–9]. Temperatures associated with this cooling are typically in the range of 10 µK, allowing for great control and manipulation of the atoms [3]. Because of these low temperatures, atoms are described quantum mechanically, making ultracold atoms a beautiful field for the study of for example Bose-Einstein condensates, degenerate Fermi gasses and quantum information processing [3,10,11].

In our experiment, we will for the first time combine the interesting fields of nano-plasmonics and ultracold atoms by controlling and studying the coupling between atoms and light close to a plasmonic nanostructure sample. The atoms are placed close to the sample surface where they are trapped optical in the evanescent field of nanoplasmonic structures [12]. With this experimental setup we could for instance investigate what influence an atom has on the optical properties of a nanohole and vice versa.

For the cooled atoms, isotope 87 of Rubidium (Rb) is used. This isotope has a positive scattering length which means that it is mutually repulsive at low temperatures [13]. ^{87}Rb also has strong absorption lines at wavelengths that can be reached with commercially available diode lasers.

We need a way to accurately and reproducibly position the atoms above the sample surface. The first step is to obtain a source of cold ^{87}Rb. To this end, an ampul of natural Rb is heated to obtain a vapor of Rb. The atoms in this vapor are cooled and collected in a two-dimensionally shaped cigar using a 2D-magneto-optical trap [3,7–9,14–16]. From this trap, the atoms are pushed into a 3D-magneto-optical trap (3D-MOT). In this trap the atoms are confined in three dimensions at the center

of the vacuum chamber. The theory and experimental setup of the magneto-optical trap are discussed in Section 2.

The sample cannot be placed under the cloud of cooled atoms as this will block one of the lasers used to produce the 3D-MOT. The atoms are therefore displaced towards the sample. From the 3D-MOT, the atoms are therefore loaded into a far detuned optical dipole trap. Since the optical dipole trap is red-detuned, atoms are attracted to high intensities i.e. the focus of the optical dipole trap [17]. By displacing the focus of the optical dipole trap, the atoms will also be displaced.

With the optical dipole trap the atoms are positioned above the sample. Using a vertically aligned optical conveyor, the atoms are moved down towards the sample surface. The optical conveyor consists of two counter-propagating beams with identical wavelengths [18–20]. Due to their interference a standing wave is formed. Using red-detuned lasers, the atoms are attracted to intensity maxima i.e. the anti-nodes of the standing wave. By changing the frequency of one of the two counterpropagating beams slightly, the standing wave and thus the anti-nodes will move [18–20]. With the optical conveyor the atoms are positioned at $\lambda/2$ above the sample surface, where λ denotes the wavelength of the lasers.

With the optical conveyor we position the atoms vertically with respect to the sample surface. However, we also want to be able to move the atoms in two-dimensions over the sample surface. This means we need to translate the optical conveyor in the plane of the sample while keeping the counterpropagating beams overlapped. This is the most unique and challenging part of the setup. The translation of a single laser beam in two dimensions is achieved using two mirror galvanometers. Each mirror galvanometer consists of a mirror mounted directly on the shaft of an electromotor. It thus rotates around its axis when applying a current to the motor. Appropriately placed lenses convert the change in angle to a change in position. By actively synchronizing the translation of the counterpropagating beams, they remain overlapped [21].

In this thesis we trap atoms in an optical dipole trap. We measure the lifetime of the atoms in this trap. In Section 3, the theory and experimental setup of the optical dipole trap are discussed. Also included is the description of the experimental control. The results of the atom lifetime are discussed in Section 4.

In addition, we have developed a method to displace the anti-nodes of the standing wave. We investigated this method of displacement both electronically and optically. In Section 5, the theory and experimental setups of the optical conveyor are discussed. A method to test the accuracy of the displacement of the anti-nodes and the results of these tests are discussed in Section 6. Furthermore, a detailed design of the final setup of the optical conveyor is presented in Section 7. This design includes the translation of the optical conveyor. The conclusions on both the optical dipole trap and optical conveyor are given in Section 8.

2 Magneto-Optical Trap: Theory and Setup

In the experiment, the optical dipole trap and optical conveyor can only capture atoms of a certain maximum temperature [15]. Hence, a cold and dense cloud of ^{87}Rb atoms is required. This cold cloud can be obtained using a magneto-optical trap (MOT). The MOT is the most commonly used method to trap and cool neutral atoms. Atoms are cooled and trapped by applying both optical and magnetic fields [3, 14]. Temperatures that can be reached with a MOT are in the order of 100 µK [14].

This section is divided into two parts. In Section 2.1, we will derive a velocity- and position dependent force which arise due to the effects of optical and magnetic fields on atoms. With these forces the operating principles of a MOT are explained. In Section 2.2, the experimental setup of the MOT is discussed.

2.1 Theory of magneto-optical trapping

The temperature of atoms is a measure of their kinetic energy. Cooling atoms is thus equivalent to slowing them down. Hence, by exerting a velocity dependent force in the direction opposite to the propagation direction of the atoms, they are slowed down. The faster the atom moves in one direction, the larger the force exerted on the atoms should be. In other words, one wants to exert a friction on the atoms. A velocity dependent force is obtained using Doppler cooling, discussed in Section 2.1.1. By only exerting a velocity dependent force, atoms are slowed down but not trapped in space. To confine atoms to a small region of space, a position dependent force on the atoms is also required. The position dependent force is obtained using an inhomogeneous magnetic field. Atoms further away from the zero point of the magnetic field should experience a larger force, pushing the atoms towards the zero point of the magnetic field. This position dependent force is discussed in Section 2.1.2.

2.1.1 Doppler cooling

For a two-level atom with a ground state and an excited state, the levels are coupled by a radiative transition. These levels are coupled with resonance frequency ω_0. The lifetime of the excited state is given by $1/\gamma$, where γ denotes the natural linewidth. When the atom is illuminated by a laser with frequency ω_L and intensity I, the atom absorbs and re-emits photons due to spontaneous emission. The scattering rate γ_p for an atom at rest is given by [15, 22]

$$\gamma_\mathrm{p} = \left(\frac{\gamma}{2}\right) \frac{s_0}{1 + s_0 + 4\left(\Delta/\gamma\right)^2}, \tag{2.1}$$

where $s_0 = I/I_\mathrm{sat}$ denotes the on-resonance saturation parameter, I_sat the saturation intensity of the atomic transition, and $\Delta = \omega_\mathrm{L} - \omega_0$ the detuning of the laser from

the atomic transition. For a high laser intensity, the scattering rate saturates due to the fact that stimulated emission will limit the population of the upper state to 50 %. This is captured in Equation 2.1 by the s_0 in the denominator. The maximum scattering rate is thus given by $\gamma/2$.

Imagine an atom moving with a velocity $\vec{v}$ inside the field of two counterpropagating laser beams. Both lasers are slightly red-detuned ($\Delta < 0$) with respect to the atomic transition. The frequency, intensity and polarization of both lasers are equal. In the reference frame of the atom, the moving atom experiences the frequency of the lasers to be different from ω_{L} due to the Doppler shift. When the atom and photons are moving in the same direction the frequency is red-shifted in the reference frame of the atom. When the atom and photons are counterpropagating, the frequency appears to be higher and is therefore blue-shifted. When counterpropagating, the frequency moves towards resonance. The detuning thus becomes smaller. As can be seen from Equation 2.1, the scattering rate is higher for small values of Δ and on resonance ($\Delta = 0$) the maximum amount of photons is scattered. Due to conservation of momentum, the atom is slowed down by the momentum $p = \hbar k_{\mathrm{L}}$ of the photon, where $\hbar$ denotes the reduced constant of Planck and k_{L} the wavenumber of the photon. Once excited, the atom falls back to the ground state by emitting a photon with a momentum equal to $\hbar k$, where k denotes the wavenumber of the emitted photon. However, the photon is emitted by spontaneous emission which is isotropic. Therefore, the net-effect of the force due to spontaneous emission is zero when averaged over many scattering events. The atom is thus slowed down by the absorption of photons.

The force $\vec{F}$ exerted by one laser on the atom in its reference frame is directly related to the scattering rate of photons [14]. The force is given by

$$\vec{F} = \frac{d\vec{p}}{dt} = \hbar\vec{k}\gamma_{\mathrm{p}}. \tag{2.2}$$

By taking the Doppler shift $\omega_{\mathrm{D}} = -\vec{k}\cdot\vec{v}$ into account in the scattering rate, the force on the atom is given by [14]

$$\vec{F}_{\pm} = \pm\hbar\vec{k}\left(\frac{\gamma}{2}\right)\frac{s_0}{1 + s_0 + 4\left[(\Delta \mp \omega_{\mathrm{D}})/\gamma\right]^2}, \tag{2.3}$$

where $\vec{F}_{\pm}$ denotes the force on the atom when moving in the same (+) and opposite (−) direction of the photons, respectively. Note that $\vec{k}$ opposite to $\vec{v}$ produces a positive Doppler shift. If we expand this expression for small Doppler shifts, we find the friction force [16]

$$\vec{F}_{\mathrm{OM}} = \vec{F}_{+} + \vec{F}_{-}, \tag{2.4}$$

$$\cong \frac{8\hbar k^2\Delta\vec{v}}{\gamma}\frac{s_0}{1 + s_0 + 4\left[\Delta/\gamma\right]^2}. \tag{2.5}$$

Until now we have used only one pair of counterpropagating laser beams to slow down atoms moving along the axis of the beams. Extending this by using a total of three orthogonal pairs of counterpropagating laser beams, every velocity component of the atom will be decreased. Many atoms can therefore be cooled and collected in a region of space, determined by the overlap volume of the lasers. This is known as an optical molasses (OM).

Temperatures associated with an optical molasses are limited because although atoms are cooled when absorbing photons, they are also heated because of the random recoil they obtain when emitting a photon. The minimum temperature for an optical molasses is called the Doppler temperature T_{D}. It is given by [16]

$$T_{\mathrm{D}} = \frac{\hbar\gamma}{2k_{\mathrm{B}}}, \tag{2.6}$$

where k_{B} denotes the Boltzmann constant. For ^{87}Rb the Doppler temperature is equal to $T_{\mathrm{D}} = 146\,\mu\mathrm{K}$ [22]. Despite the low temperatures obtainable with an optical molasses, the atoms are still able to diffuse out of the optical molasses region. A position dependent force is thus still required to trap the atoms. Such a force can be exerted on the atoms by introducing an inhomogeneous magnetic field.

2.1.2 Magnetic trapping

To understand magneto-optical trapping, let us assume the angular momentum of the ground states of the atom is $J = 0$ and of the excited state $J = 1$ [23]. In absence of a magnetic field, the $m_{\mathrm{j}} = -1, 0$ and $+1$ states can be coupled to the ground state. The polarization of the laser beam now determines which transition is excited. The $\Delta m_{\mathrm{j}} = -1$ and $\Delta m_{\mathrm{j}} = +1$ transitions are excited by left- (σ^-) and right-handed (σ^+) circularly polarized light, respectively. The $\Delta m_{\mathrm{j}} = 0$ transition can be excited using π-polarized light. For this polarization, the electric field component is parallel to the plane of incidence.

In the presence of a magnetic field, an energy shift occurs of the excited states due to the Zeeman effect. The energy shift ΔE is given by [24]

$$\Delta E = m_{\mathrm{j}} g_{\mathrm{j}} \mu_{\mathrm{B}} B, \tag{2.7}$$

where μ_{B} denotes the Bohr magneton, and B the applied magnetic field. The Landé g-factor g_{j} is given by [22]

$$g_{\mathrm{j}} = 1 + \frac{J(J+1) + S(S+1) - L(L+1)}{2J(J+1)}, \tag{2.8}$$

where L denotes the orbital angular momentum, S the spin angular momentum, and $J = L + S$ the total angular momentum of the atom.

As can be seen from Equation 2.7, the magnitude of the energy shift depends on the strength of the magnetic field. Let us consider an atom placed in an inhomogeneous magnetic field

$$B(z) = \frac{dB}{dz} z, \tag{2.9}$$

where dB/dz is the field gradient in the z-direction. The zero point of the magnetic field is chosen at $z = 0$. As illustrated in Figure 2.1, if the atom is on the right ($z > 0$) of the zero point of the magnetic field, the level $|J = 1, m_\mathrm{j} = -1\rangle$ is shifted downwards while $|J = 1, m_\mathrm{j} = +1\rangle$ is shifted upwards. If the polarization of the laser beam from the right is σ^- and the laser is red-detuned, the rate of absorption of the photons will thus increase. Because the level $|J = 1, m_\mathrm{j} = +1\rangle$ is shifted upwards, the rate of photon absorbtion for σ^+ polarized light is decreased. This results in a net force in the $-z$-direction. Analogous to an atom on the right ($z > 0$), an atom on the left ($z < 0$) experiences a force exerted in the $+z$-direction. This trapping mechanism results in a one-dimensional localization of the atom. Extending this localization to three-dimensions by using three pairs of counterpropagating beams with the appropriate polarization a MOT is obtained.

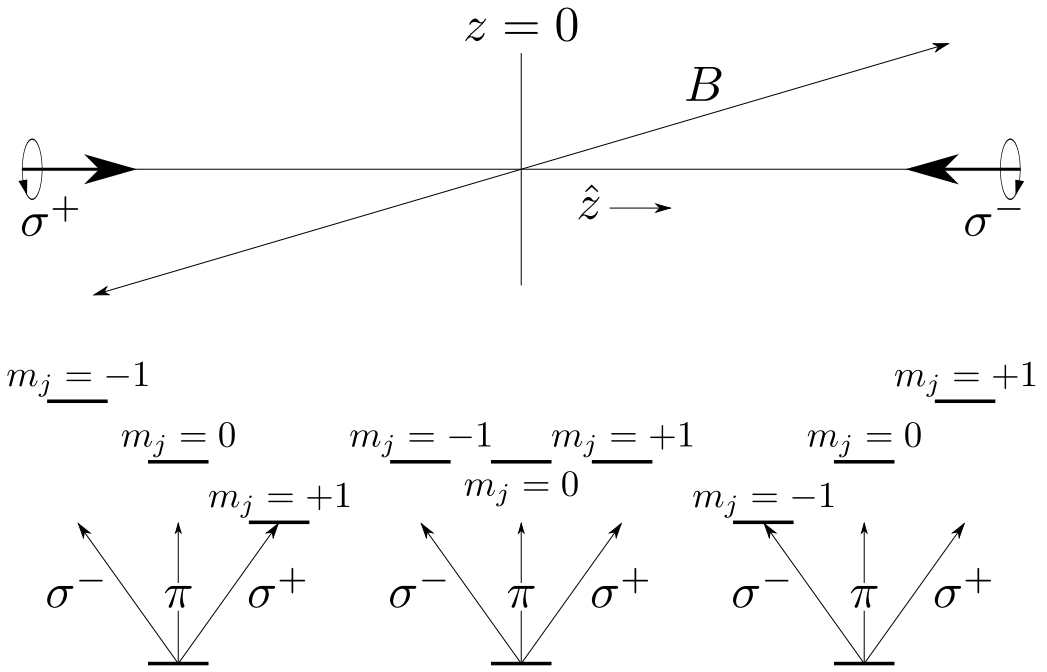

Figure 2.1: One-dimensional inhomogeneous magnetic field, which causes the energy levels, m_j to shift such that different types of polarization (σ^-, σ^+) are required to excite the atom. The magnitude of this shift depends on the position away from the zero point of the magnetic field.

Accounting for the Zeeman shift, the force on the atoms given by Equation 2.3 is

extended to

$$\overrightarrow{F}(z)_{\pm} = \pm\hbar\overrightarrow{k}\left(\frac{\gamma}{2}\right)\frac{s_0}{1+s_0+4\left[(\Delta\mp\omega_{\mathrm{D}}\pm\omega_{\mathrm{Z}})/\gamma\right]^2}, \tag{2.10}$$

where $\omega_{\mathrm{Z}} = \mu' B(z)/\hbar$ denotes the Zeeman shift, and $\mu' = (g_e m_e - g_g m_g)\mu_B$ the difference in Zeeman shift between the ground state (g) and excited state (e).

2.1.3 Multi-level atoms in a magneto-optical trap

Until this point, the working principle of the MOT has been explained using a two-level atom scheme. However, atoms are of course multi-level systems and to complicate matters further, alkali atoms have a nuclear spin. This means there are energy shifts, caused by the coupling of the spin $\vec{S}$ with the orbital angular momentum $\vec{L}$ and the interaction of the nuclear spin $\vec{I}$ with the total angular momentum of the electron $\vec{J} = \vec{L} + \vec{S}$ [24]. The energy level shifts are the fine- and hyperfine structures. They influence the cooling scheme. Hence, an extension of the two-level atom has to be made. The ^{87}Rb D_2 hyperfine structure is given in Appendix A.

Due to conservation of angular momentum not all transitions between hyperfine states are allowed. The allowed transitions are governed by the selection rules [24]. For hyperfine splitting, these rules are given by $\Delta F = 0, \pm 1$, except for the $F = 0 \longrightarrow F' = 0$ transition, where ΔF denotes the difference between the ground state F and excited level F' for the hyperfine levels. Note that the selection rule holds for both the excitation and decay of an atom. As we have seen in Section 2.1.1, atoms are cooled by absorbing photons. Once excited, atoms cannot absorb another photon and thus cannot be cooled in that period of time. For the cooling process it is most preferable to use the hyperfine transition from which the atom can only fall back to one hyperfine ground state. This way, the atom is immediately able to absorb another photon. This transition is referred to as the cooling transition or cycling transition.

For a multi-level scheme, the Zeeman shift also needs a small correction [22]. In the presence of hyperfine levels the Landé g-factor changes from g_{j} to

$$g_{\mathrm{F}} = g_{\mathrm{j}}\frac{F(F+1) - I(I+1) + J(J+1)}{2F(F+1)}. \tag{2.11}$$

2.2 Experimental setup

The atoms are initially trapped from a vapor, in which atoms typically have a velocity in the range of 500 m/s to 1000 m/s [15]. In our setup, we use a combination of a two-dimensional MOT (2D-MOT) with a three-dimensional MOT (3D-MOT). They are separated by a differential pumping section which helps to maintain a large pressure

difference between the 2D MOT and 3D MOT chamber. The 2D-MOT is used to decrease the initial velocity and to load the 3D-MOT. The vapor in the 2D-MOT chamber contains both species (isotopes 85 and 87) of Rubidium. However, only the ^{87}Rb atoms which are pre-cooled by the 2D-MOT are loaded into the 3D-MOT.

In this subsection the experimental setup is described. To this end, the subsection is divided into four parts. Firstly, in Section 2.2.1, the rubidium source is discussed. Secondly, in Section 2.2.2, the vacuum chambers used for both the 2D- and 3D-MOT are discussed. Subsequently, in Section 2.2.3, the magnetic fields are discussed which are used for the magneto optical trapping of atoms. Finally, in Section 2.2.4, the laser system used for cooling the atoms is discussed.

The vacuum setup of the 2D- and 3D-MOT is illustrated in Figure 2.2 and will be used in this subsection to indicate certain elements.

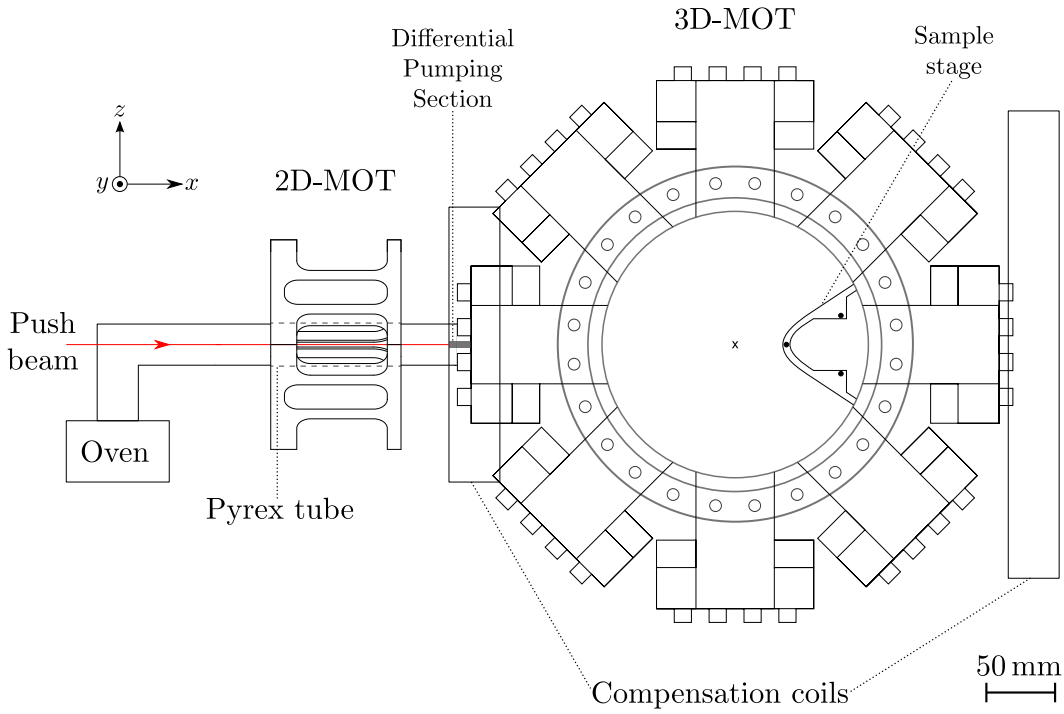

Figure 2.2: Top view of the setup. The oven is not to scale.

2.2.1 Rubidium source

For our rubidium source, an ampul containing 1 g of natural rubidium (Rb) is used, with a natural abundance of 72.17 % for ^{85}Rb and 27.83 % for ^{87}Rb [22]. In the experiment, Rb is evaporated in the oven by heating the ampul above its melting

point of 39.3 °C [22]. We use temperatures in the range of 60 °C to 90 °C. From the oven the atoms move into the 2D-MOT vacuum chamber. Since the completion of this work, the oven has been turned of, as enough Rb has been deposited in the 2D-MOT chamber.

2.2.2 Vacuum chambers

The experiment uses two connected vacuum chambers, an elongated pyrex tube for the 2D-MOT with a pressure of $\sim 10^{-7}$ mbar and a stainless steel chamber for the 3D-MOT with a pressure of $\sim 10^{-10}$ mbar. The pressure for both the 2D- and 3D-MOT is maintained by ion getter pumps.

The 3D-MOT chamber and the 2D-MOT pyrex tube are separated by means of a differential pumping section. It maintains the large pressure difference between the two vacua. Atoms from the 2D-MOT are pushed into the 3D-MOT chamber through the differential pumping section, which is a 5 cm long pipe with an inner diameter of 1.1 mm.

The loading rate of the 3D-MOT can drastically be increased by introducing a push beam. This beam is aligned through the 2D-MOT and the differential pumping section into the 3D-MOT chamber. The push beam is on-resonance with the ^{87}Rb atoms. As we have seen in Section 2.1.1, this results in a force acting on the ^{87}Rb atoms in the direction of propagating of the push beam. Thus, the atoms are accelerated from the 2D-MOT, through the differential pumping section, into the 3D-MOT chamber.

2.2.3 Magnetic fields

As indicated in Section 2.1.2, magnetic fields are required for the position-dependent force on the atoms. For the 2D-MOT, a quadrupole field in the y,z-plane is obtained using four rectangular coils. Each coil consists of 81 windings. The zero point of the magnetic field is along the x-axis. Thus, the Zeeman shift does not occur in the center of the trap. From the center, the magnetic field increases equally in the y,z-plane. With the position-dependent force obtained by the quadrupole field, the atoms in the 2D-MOT are collected in a cigar-shaped cloud along the x-axis. For the magnetic field of the 2D-MOT a current of 2.03 A is applied, yielding a field gradient of 7.70 G/cm. Note that in Figure 2.2 only the cage used to wind the solenoids is indicated. It is rotated by 45° with respect to the x,y-plane.

The quadrupole field for the 3D-MOT is obtained by placing two coils on top of each other in an anti-Helmholtz configuration. Each coil consists of 195 windings. Current runs through both coils in opposite directions, resulting in a zero point in the centre of the quadrupole field. Due to the Zeeman shift the atoms experience

a force directed towards the zero point. For the quadrupole field of the 3D-MOT a current of 15.0 A is used, resulting in a gradient of 16.01 G/cm. Note that the coils for the 3D-MOT are not shown in Figure 2.2.

The magnetic field of the 3D-MOT influences the magnetic field of the 2D-MOT as the gradient of the 3D-MOT is along the x-axis of the quadrupole field of the 2D-MOT. Left uncorrected this would impede the functions of the 2D-MOT. To counter the influence, a pair of compensation coils was designed. The first compensation coil has a diameter of 20 cm and consists of 320 windings. It is placed in between the 2D- and 3D-MOT. The second compensation coil, located at the far end of the setup as indicated in Figure 2.2, has of a diameter of 34 cm and 320 windings. The compensation coils are connected in series and carry a current of 2.3 A.

When current is run through the coils, the ohmic resistance causes heating [25]. To this end, all coils in the experiment, except for the compensation coils, are water cooled.

2.2.4 Diode lasers

A total of five diode lasers are used to obtain the 3D-MOT. The first laser is used as a reference for the offset-locks of the lasers used for the cooling. It is operated at the crossover transition (1,3). Two parts of the beam are split off using beam splitter cubes. Both parts are shifted to resonance by AOMs. These are used as the push beam and the probe beam which are required for a fast loading rate of the 3D-MOT and for absorption imaging of the atoms, respectively. Absorption imaging is discussed in more detail in Section 3.3.1. As can be seen from the hyperfine structure in Appendix A, the frequency needs to be shifted by 211.79 MHz. From this point forward, the first laser will be known as the reference & push laser.

Light on two transitions are required to obtain a MOT. A laser for the $F = 2 \longrightarrow F' = 3$ transition which is referred to as the cooling laser and a laser for the $F = 1 \longrightarrow F' = 2$ transition which is referred to as the re-pump laser. Note that for both the 2D and 3D-MOT we need a cooling and re-pump laser. The cooling lasers are slightly red detuned with respect to the $F = 2 \longrightarrow F' = 3$ transition. As discussed before, this is required for cooling and trapping. A re-pump lasers is required to excite atoms that have fallen into the dark state, thus enabling them again to participate in the cooling scheme.

In Table 2.1, an overview of the lasers used in the experiment is given. In the table, the transitions to which the laser is locked to is indicated. Also included is the detuning from that locking transition. In Table 2.1, the push and probe are denoted separately with respect to the reference beam due to their different detuning.

In Table 2.2, the detuning of both the 2D- and 3D-cool lasers are given with respect

to resonance $F' = 3$.

Laser	Locked to	Detuning to lock
Reference	Crossover (1,3)	0 MHz
Push and Probe	Crossover (1,3)	211.79 MHz
2D-Cool	Offset locked to reference	204 MHz
2D-Repump	$F = 2 \longrightarrow F' = 3$	0 MHz
3D-Cool	Offset locked to reference	193 MHz
3D-Repump	$F = 2 \longrightarrow F' = 3$	0 MHz

Table 2.1: Overview of the lasers including the transition to which they are locked to and the detuning from that transition.

Laser	Detuning to $F' = 3$
2D-cool	-8 MHz
3D-cool	-19 MHz

Table 2.2: Overview of the detuning from resonance ($F' = 3$) for both 2D- and 3D-cool lasers.

3 Optical Dipole Trap: Theory and Setup

With the cloud of cold ^{87}Rb atoms realized in Section 2, the next step in the experiment is to position the atoms above the sample surface. To this end, the atoms are first moved horizontally in the x-direction. This horizontal movement is achieved using an optical dipole trap (ODT).

This section can be divided into three parts. Firstly in Section 3.1, two important properties of dipole traps are obtained, namely the trap depth and the scattering rate. Secondly, the experimental setup is discussed in Section 3.2. Finally the experimental procedure and control is discussed in Section 3.3.

3.1 Theory of optical dipole trapping

As we have seen in Section 2.1, the MOT uses a radiation force to slow atoms down. In combination with a magnetic field, cold atoms can be collected in a small region of space. The ODT however uses a dipole force to confine the atoms. In short the mechanism works as follows. When an atom is placed into the field of a single laser beam, an atomic dipole moment is induced due to the electric field $\vec{E}$ of that beam. The atom will thus experience a force because of the interaction between the induced atomic dipole moment and the intensity gradient of the electric field. An important difference with respect to the MOT is that the ODT is detuned far from the atomic resonance, such that atoms have a low photon absorption rate. The ODT can therefore be considered a conservative force.

In this subsection, two important properties for ODTs are obtained; the trap depth and the photon scattering rate.

3.1.1 Classical Lorentz model

Very roughly speaking, an atomic dipole moment is induced because the electric field $\vec{E}$ is pulling the electrons and nucleus apart from each another while their mutual attraction is drawing them together. The positive and negative charges shift due to the forces acting on them, leaving the atom polarized. The induced dipole moment oscillates at the driving frequency ω_{L} and is given by [25]

$$\vec{p}(\vec{r},t) = \alpha(\omega_{\mathrm{L}})\vec{E}(\vec{r},t), \tag{3.1}$$

where $\vec{p}(\vec{r},t) = \hat{\mathbf{e}}\tilde{p}(\vec{r})\exp(-i\omega_{\mathrm{L}}t) + c.c.$ and $\vec{E}(\vec{r},t) = \hat{\mathbf{e}}\tilde{E}(\vec{r})\exp(-i\omega_{\mathrm{L}}t) + c.c.$ denote the atomic dipole moment and the electric field respectively, and $\alpha(\omega_{\mathrm{L}})$ the complex polarizability of the atom. For the atomic dipole moment and the electric field, $\tilde{p}$ and $\tilde{E}$ denote the amplitude, respectively, $\hat{\mathbf{e}}$ the polarization unit vector, and *c.c.* the complex conjugate.

The real part of the complex polarizability describes the in-phase component of the induced dipole moment with the electric field. It is responsible for the dispersive properties of the interaction. The imaginary part describes the out-of-phase component of the induced dipole moment with the electric field. This describes the work done by the electric field or in other words, the scattering of light. The real and imaginary part of the complex polarizability are thus used to determine the interaction potential and the photon scattering rate, respectively.

The force of a dipole in an electric field is given by [25]

$$\vec{F} = (\vec{p} \cdot \nabla)\, \vec{E}. \tag{3.2}$$

An expression for $(\vec{p} \cdot \nabla)\, \vec{E}$ is obtained using the vector dot product relation between vectors $\vec{A}$ and $\vec{B}$ [25]

$$\nabla \left(\vec{A} \cdot \vec{B}\right) = \vec{A} \times \left(\nabla \times \vec{B}\right) + \vec{B} \times \left(\nabla \times \vec{A}\right) + \left(\vec{A} \cdot \nabla\right) \vec{B} + \left(\vec{B} \cdot \nabla\right) \vec{A}. \tag{3.3}$$

For a permanent dipole ($\vec{p} = \text{const.}$), we obtain

$$\nabla \left(\vec{p} \cdot \vec{E}\right) = 0 + 0 + (\vec{p} \cdot \nabla)\, \vec{E} + 0, \tag{3.4}$$

where we used that the curl of an electrostatic field is zero since the magnetic field is zero.

For a permanent dipole the potential energy yields

$$U(\vec{r}) = -\int d\vec{r} F(\vec{r}) = -\vec{p} \cdot \vec{E}. \tag{3.5}$$

However, if $\vec{p}$ is not constant but is given by Equation 3.1, we obtain

$$\nabla \left(\vec{p} \cdot \vec{E}\right) = 2\alpha \vec{E} \left(\nabla \times \vec{E}\right) + 2\alpha \left(\vec{E} \cdot \nabla\right) \vec{E}, \tag{3.6}$$

$$= 0 + 2\,(\vec{p} \cdot \nabla)\, \vec{E}. \tag{3.7}$$

As can be seen from Equation 3.7, the potential energy of an induced dipole moment is half that of a permanent dipole. We obtain

$$U_{\text{dip}}(\vec{r}) = -\frac{1}{2} \left\langle \vec{p} \cdot \vec{E} \right\rangle = -\frac{1}{4} \operatorname{Re}(\alpha)\, |E(\vec{r})|^2, \tag{3.8}$$

where $\langle \ldots \rangle$ denotes the time average over the rapid oscillating terms. Note that the squared amplitude of the electric field is given by $|E(\vec{r})|^2 = E(\vec{r})E(\vec{r})^*$, where $E(\vec{r})^*$ denotes the complex conjugate of $E(\vec{r})$. By introducing the intensity of the light field in vacuum $I(\vec{r}) = \frac{1}{2}\epsilon_0 c |\tilde{E}(\vec{r})|^2$, the potential energy can be written as

$$U_{\text{dip}}(\vec{r}) = -\frac{1}{2\epsilon_0 c} \operatorname{Re}(\alpha)\, I(\vec{r}), \tag{3.9}$$

where ϵ_0 denotes the permittivity of vacuum, and c the speed of light in vacuum. The dipole potential thus depends on the real part of the complex polarizability and the intensity. Because of the conservative nature of the dipole force, it can be written as the negative gradient of the dipole potential. This results in

$$F_{\mathrm{dip}}\left(\vec{r}\right) = -\nabla U_{\mathrm{dip}}\left(\vec{r}\right) = -\frac{\mathrm{Re}\left(\alpha\right)}{2\epsilon_0 c}\nabla I\left(\vec{r}\right). \tag{3.10}$$

As can be seen from Equation 3.10, the dipole force is proportional to the gradient of the intensity. When the laser is red detuned with respect to the atomic transition, the real part of the polarizability is positive. The atoms are therefore attracted to regions of high intensity.

As mentioned earlier, the imaginary part of the complex polarizability is responsible for scattering. It is therefore used to derive the scattering rate. When light impinges on an atom, the corresponding scattering rate is obtained by dividing the absorbed power by the energy of the photons $E_{\mathrm{p}} = \hbar\omega_{\mathrm{L}}$. The absorbed power P_{abs} is given by [17]

$$P_{\mathrm{abs}} = \left\langle \dot{\vec{p}} \cdot \vec{E} \right\rangle = \frac{1}{2}\omega_{\mathrm{L}}\,\mathrm{Im}\left(|p|\,|E^*|\right) = \frac{\omega_{\mathrm{L}}}{\epsilon_0 c}\,\mathrm{Im}\left(\alpha\right) I. \tag{3.11}$$

The scattering rate thus results in

$$\Gamma_{\mathrm{sc}}\left(\vec{r}\right) = \frac{P_{\mathrm{abs}}}{\hbar\omega_{\mathrm{L}}} = \frac{1}{\hbar\epsilon_0 c}\,\mathrm{Im}\left(\alpha\right) I\left(\vec{r}\right). \tag{3.12}$$

Both the interaction potential and the scattering rate have been derived in terms of the field intensity $I(\vec{r})$ and the polarizability $\alpha(\omega)$. To obtain an expression for the polarizability, we consider the classical Lorentz oscillator model for our atom. In this model, the assumption is made that the nucleus of an atom is much more massive than an electron. Furthermore, we can treat the electron as being connected by a classical spring to an infinite mass which does not move. The electron has a mass m_{e} and elementary charge e. The equation of motion of the electron then becomes

$$F = m_{\mathrm{e}}\ddot{x}(t) = -m_{\mathrm{e}}\Gamma\dot{x}(t) - m_{\mathrm{e}}\omega_0^2 x(t) - eE(t). \tag{3.13}$$

In Equation 3.13, the frictional damping force is given by $m_{\mathrm{e}}\Gamma\dot{x}$, where $\Gamma = \frac{e^2}{m_{\mathrm{e}}}\frac{\omega_{\mathrm{L}}^2}{6\pi\epsilon_0 c^3}$ denotes the classical damping rate [23]. The restoring force of the oscillator is denoted by $m_{\mathrm{e}}\omega_0^2 x(t)$, where the spring constant is given by $m_{\mathrm{e}}\omega_0^2$. The driving force due to the electric field is given by $-eE(t)$. The solution of the second-order differential equation in Equation 3.13 is given by

$$x(t) = -\frac{eE(\vec{r},t)}{m_{\mathrm{e}}}\frac{1}{\omega_{\mathrm{L}}^2 - \omega_0^2 - \imath\omega_{\mathrm{L}}\Gamma}. \tag{3.14}$$

In the Lorentz model, the dipole moment is given by $\vec{p} = -e\vec{x}$. Hence, the complex polarizability is given by

$$\alpha(\omega_\mathrm{L}) = \frac{e^2}{m_\mathrm{e}} \frac{1}{\omega_0^2 - \omega_\mathrm{L}^2 - \imath\omega_\mathrm{L}\Gamma}. \tag{3.15}$$

With the introduction of an on-resonance damping rate γ given by

$$\gamma = \Gamma \left(\frac{\omega_0}{\omega_\mathrm{L}}\right)^2 = \frac{e^2}{m_\mathrm{e}} \frac{\omega_0^2}{6\pi\epsilon_0 c^3}, \tag{3.16}$$

the complex polarizability can be rewritten to

$$\alpha(\omega_\mathrm{L}) = 6\pi\epsilon_0 c^3 \frac{\gamma/\omega_0^2}{\omega_0^2 - \omega_\mathrm{L}^2 - \imath(\omega_\mathrm{L}^3/\omega_0^2)\gamma}. \tag{3.17}$$

The polarizability of the atom can also be determined semiclassical. This is done by considering the atom as a two-level quantum system with the classical radiation field. However, in an ODT the atom is kept in the ground state to decrease the photon scattering rate. Hence, the radiation force is minimized. ODTs are therefore operated at large detunings Δ. By doing so, saturation effects can be neglected. The semiclassical approach thus yields the same result as the classical approach.

Using the expression for the polarizability given by Equation 3.17 in combination with Equations 3.9 and 3.12, the following expressions for the interaction potential and the scattering rate are obtained;

$$U_\mathrm{dip}(\vec{r}) = \frac{3\pi c^2}{2\omega_0^3} \left(\frac{\gamma}{\omega_\mathrm{L} - \omega_0} - \frac{\gamma}{\omega_\mathrm{L} + \omega_0}\right) I(\vec{r}), \tag{3.18}$$

and

$$\Gamma_\mathrm{sc}(\vec{r}) = \frac{3\pi c^2}{2\hbar\omega_0^3} \left(\frac{\omega_\mathrm{L}}{\omega_0}\right)^3 \left(\frac{\gamma}{\omega_\mathrm{L} - \omega_0} - \frac{\gamma}{\omega_\mathrm{L} + \omega_0}\right)^2 I(\vec{r}). \tag{3.19}$$

As can be seen in Appendix A, the resonance frequency for ^{87}Rb equals $\omega_0 = 2\pi \cdot 384\,\mathrm{THz}$. Using a wavelength of $\lambda = 1070.6\,\mathrm{nm}$, the laser frequency equals $\omega_\mathrm{L} = \frac{2\pi c}{\lambda} = 2\pi \cdot 280\,\mathrm{THz}$. Note that with these values, we obtain a detuning which is much smaller than the resonance frequency. In this case, the rotating-wave approximation (RWA) can be applied to neglect any rapidly oscillating terms [17]. This means we neglect the $\frac{1}{\omega_\mathrm{L}+\omega_0}$ term with respect to the $\frac{1}{\omega_\mathrm{L}-\omega_0}$ term. Applying the RWA we obtain

$$U_\mathrm{dip}(\vec{r}) = \frac{3\pi c^2}{2\omega_0^3} \frac{\gamma}{\Delta} I(\vec{r}), \tag{3.20}$$

and

$$\Gamma_\mathrm{sc}(\vec{r}) = \frac{3\pi c^2}{2\hbar\omega_0^3} \left(\frac{\gamma}{\Delta}\right)^2 I(\vec{r}). \tag{3.21}$$

With Equations 3.20 and 3.21, the working principle of ODTs can be explained. As can be seen from Equation 3.20, the sign of the detuning determines the sign of the interaction potential. Potential minima's are therefore found at maxima and minima of the intensity for red and blue detuning, respectively.

We also note that the interaction potential scales with I/Δ, whereas the scattering rate scales with I/Δ^2. In order to trap atoms using an ODT, the scattering rate needs to be low to ensure that the atoms are not excited. This can be achieved by choosing a large detuning. This however also lowers the interaction potential which determines the trap depth. By increasing the intensity, while keeping I/Δ constant, the trap depth can be kept constant, while the scattering rate is reduced.

3.1.2 Multi-level atoms in an optical dipole trap

The interaction potential and scattering rate have been derived assuming a two-level system. Since atoms are multi-level systems, adjustments need to be made. This is achieved by evaluating the effect of the laser light as a second-order time-dependent perturbation. The shift of the ground state energy of level i is given by [17]

$$\Delta E_i(\vec{r}) = \frac{3\pi c^2}{2\omega_0^3}\gamma I(\vec{r}) \sum_j \frac{C_{ij}^2}{\Delta_{ij}}, \tag{3.22}$$

where C_{ij} denotes the Clebsch-Gordan coefficients of the transition between the ground state $|g_i\rangle$ and the excited state $|e_j\rangle$, and Δ_{ij} the detuning of the corresponding sub-levels i and j.

Using the energy shift from Equation 3.22, a general result is derived for the interaction potential and the scattering rate of the ground state $|F, m_F\rangle$. They are given by [17]

$$U_{\mathrm{dip}}(\vec{r}) = \frac{\pi c^2 \gamma}{2\omega_0^3}\left(\frac{2+\mathcal{P}g_{\mathrm{F}}m_{\mathrm{F}}}{\Delta_2} + \frac{1-\mathcal{P}g_{\mathrm{F}}m_{\mathrm{F}}}{\Delta_1}\right) I(\vec{r}), \tag{3.23}$$

and

$$\Gamma_{\mathrm{sc}}(\vec{r}) = \frac{\pi c^2 \gamma^2}{2\hbar\omega_0^3}\left(\frac{2+\mathcal{P}g_{\mathrm{F}}m_{\mathrm{F}}}{\Delta_2^2} + \frac{1-\mathcal{P}g_{\mathrm{F}}m_{\mathrm{F}}}{\Delta_1^2}\right) I(\vec{r}), \tag{3.24}$$

where Δ_1 and Δ_2 denote the detuning from the D_1 and D_2 line respectively, m_{F} the magnetic quantum number, and $\mathcal{P} = 0, \pm 1$ the polarization for linearly or circularly ($\sigma^{\pm}$) polarized light, respectively.

The result for the interaction potential in Equation 3.23 holds as long as the detuning is large with respect to the hyper-fine splitting of the excited state but is smaller then the fine splitting [17]. This is the case for detunings in the order of a couple of nanometers. In the case of very large detunings, which even exceeds the fine-structure splitting, Equation 3.23 is expanded linearly in terms of $\Delta'_{\mathrm{FS}}/\Delta$. The

hyperfine structure is neglected due to the very large detuning. In this case, the interaction potential can be given by [17]

$$U_{\mathrm{dip}}(\vec{r}) = \frac{3\pi c^2}{2\omega_0^3}\frac{\gamma}{\Delta}\left(1 + \frac{1}{3}\mathcal{P}g_{\mathrm{F}}m_{\mathrm{F}}\frac{\Delta'_{\mathrm{FS}}}{\Delta}\right) I\left(\vec{r}\right). \tag{3.25}$$

In our setup very large detunings are used ($\Delta \gg \Delta'_{\mathrm{FS}}$). As can be seen from Equation 3.25, using a different polarization, the trap depth either increases or decreases for σ^+ and σ^- circularly polarized light, respectively. However, in the case of linear polarized light, Equation 3.25 is equal to the result for a two-level system given by Equation 3.20.

3.1.3 Trap parameters of the optical dipole trap

For the ODT, a Ytterbium fiber laser (YLR-20-LP from IPG Photonics) is used with a wavelength of $\lambda = 1070.6\,\mathrm{nm}$ and power of $P = 20\,\mathrm{W}$.

In the experiment, atoms will be transferred from the ODT into a standing-wave trap. In a red-detuned standing-wave trap, atoms are attracted to the anti-nodes. By definition, the anti-nodes are separated from each other by $\lambda/2$. The focus of both beams is in the order of $50\,\mu\mathrm{m}$. The theory of the standing-wave trap is explained in more detail in Section 5. To increase the atom transfer efficiency from the ODT into the standing-wave trap, the focus of the ODT is elliptical. The ODT is tight in the vertical direction, so we minimize the number of anti-nodes that the atoms are loaded into. The spatial intensity distribution for a Gaussian beam along the z-axis is given by [23]

$$I(\vec{r}) = I(\rho, z) = I_0 \mathrm{e}^{\frac{-2\rho^2}{w(z)^2}}, \tag{3.26}$$

where I_0 denotes the intensity amplitude at the center of the beam, ρ the radial coordinate, and $w(z)$ the beam waist in the radial direction at which the field amplitude drops to 1/e at a position z. The peak intensity I_0 can be calculated by dividing the power P of the laser by the area of the focus $\frac{1}{2}\pi w_0$. Hence,

$$I_0 = \frac{2P}{\pi w_0^2}. \tag{3.27}$$

Note that in the case of an elliptical beam, the intensity changes differently for the x- and y-direction. For the determination of the trap depth, the intensity at the center of the trap is taken into account. In the center, the intensity of the trap is obtained by using the area of the elliptical focus $\frac{1}{2}\pi\omega_{0,x}\omega_{0,y}$.

For a Gaussian beam, the beam waist is given by [23]

$$w(z) = w_0\sqrt{1 + (z/z_{\mathrm{R}})^2} \tag{3.28}$$

where w_0 denotes the minimum beam radius, and $z_\mathrm{R} = \pi w_0^2/\lambda$ the Rayleigh range which denotes the distance at which the beam waist is doubled with respect to ω_0. Therefore, the Rayleigh range is also referred to as the depth of focus for Gaussian beams [23].

Using Equations 3.26 and 3.28, the trap depth and trap frequencies for the ODT can be determined. We define the trap depth $U_0 \equiv |U_\mathrm{dip}(0,0)|$ at the center of the focused beam. The trap frequencies are derived by approximating the dipole potential by an harmonic oscillator. This holds when the thermal energy $k_\mathrm{B}T$ is much smaller than the trap depth [17]. In our case the thermal energy is in the order of 100 µK, while the trap depth is in the order of 1 mK. The harmonic oscillator approximation is given by

$$U_\mathrm{dip}(\rho, z) \simeq -U_0 \left[1 - 2\left(\frac{\rho}{w_0}\right)^2 - \left(\frac{z}{z_\mathrm{R}}\right)^2\right]. \tag{3.29}$$

Note that Equation 3.29 holds in the case of a circular Gaussian beam. We extend the harmonic oscillator model for an elliptical Gaussian beam using the corresponding beam waists. We obtain

$$U_\mathrm{dip}(x, y, z) \simeq -U_0 \left[1 - 2\left(\frac{x}{w_{0,x}}\right)^2 - 2\left(\frac{y}{w_{0,y}}\right)^2 - \left(\frac{z}{z_\mathrm{R}}\right)^2\right], \tag{3.30}$$

where for the Rayleigh range of the elliptical focus the average of both individual Rayleigh ranges is taken to obtain a good approximation of the axial trap frequency.

By comparing Equation 3.30 to the energy of an harmonic oscillator given by

$$U = -U_0 + \frac{1}{2}mw_x^2x^2 + \frac{1}{2}mw_y^2y^2 + \frac{1}{2}mw_z^2z^2, \tag{3.31}$$

we find the trap frequencies

$$\Omega_x = \sqrt{\frac{4U_0}{mw_{0,x}^2}}, \tag{3.32}$$

$$\Omega_y = \sqrt{\frac{4U_0}{mw_{0,y}^2}}, \tag{3.33}$$

and

$$\Omega_z = \sqrt{\frac{2U_0}{mz_\mathrm{R}^2}}. \tag{3.34}$$

The characteristics of the ODT used in the experiment are given in Table 3.1.

The focus dimensions $w_{0,x}$ and $w_{y,0}$ are obtained from the experimental setup, discussed in the next section.

Property	Symbol	Value
Wavelength	λ	1070.6 nm
Resonance frequency	ω_0	$2\pi \cdot 384$ THz
Laser frequency	ω_L	$2\pi \cdot 280$ THz
Average laser power	P	10.4 W
Horizontal beam waist	$w_{0,x}$	40 µm
Vertical beam waist	$w_{0,y}$	23.5 µm
Horizontal Rayleigh range	$z_{\mathrm{R},x}$	4.7 mm
Vertical Rayleigh range	$z_{\mathrm{R},y}$	1.6 mm
Trap depth	U_0	-1.03 mK
Scattering rate	Γ_sc	3.5 Hz
Trap frequency (x-direction)	$\Omega_x/2\pi$	2.5 kHz
Trap frequency (y-direction)	$\Omega_y/2\pi$	4.3 kHz
Axial trap frequency	$\Omega_z/2\pi$	22.4 Hz

Table 3.1: Typical ODT characteristics for our experimental conditions.

3.2 Experimental setup

The experimental setup consists of two layers of optics. It includes the optics for the ODT used for the transport of the atoms as well as a second beam to use in a crossed-beam configuration. This is required if we need to cool to sub-10 µK temperatures. To make a clear distinction between the two ODTs, we refer to the ODT used for the horizontal movement of the atoms as the "main beam". The ODT that is used for the configuration of the crossed-beam trap is referred to as the "cross beam". Note that the cross beam is currently not used in the experiment.

In this subsection we will explain the elements on both layers of the experimental setup. This is done by first explaining the bottom layer from which we follow the laser beam to the top layer.

3.2.1 Bottom layer

The function of the bottom layer is to achieve a collimated Gaussian beam on the top layer with a controllable power. This allows us to control the depth of the trap which is required for future evaporative cooling. In Figure 3.1 the top view of the bottom layer is given.

In Figure 3.1, the laser beam is introduced into the experiment by the out-coupler. At the out-coupler, the beam has a waist of $w = 0.8$ mm. The beam height on the bottom layer is 48.1 ± 0.5 mm. Directly after the out-coupler, the laser light passes through a $\lambda/2$ waveplate. This waveplate is used to change the polarization of the

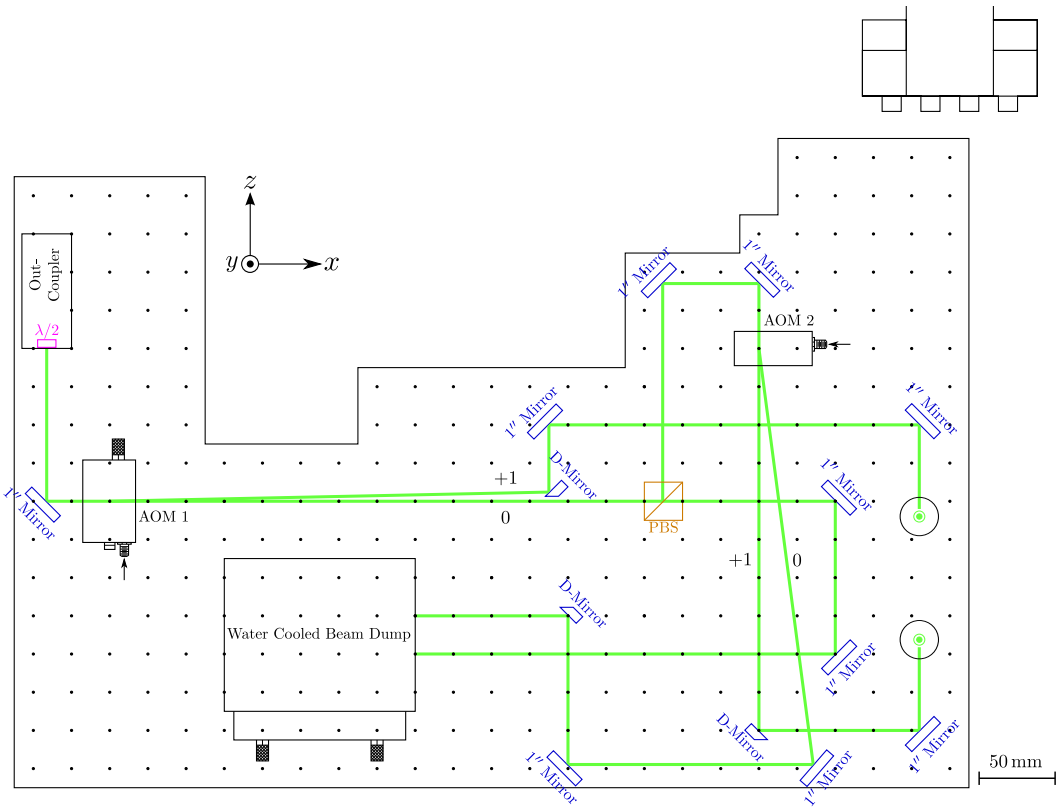

Figure 3.1: Top view of the bottom layer. Mirrors are depicted in blue, waveplates in pink, polarizing beam splitting (PBS) cubes in brown, and the Gaussian laser beam in green. The black circles are used to indicate that the beam is either coming from a different level or propagates towards one.

light. This will play a role when splitting the laser light into a part for the main beam and a part for the cross beam. After the waveplate the light passes through acousto-optic modulator (AOM) 1.

An AOM can be used to control the power, frequency and spatial direction of a laser beam using an electronic radio frequency driving signal (RF). In an AOM, a piezo-electric transducer is connected to a crystal through which the laser light propagates. By applying a RF signal to the transducer, a running acoustic wave is generated in the crystal. The sound wave generates a periodic grating of the refractive index. Under the right angle, the laser light can experience Bragg diffraction. Changing the frequency of the acoustic wave, the frequency of the diffracted laser beam can be controlled. By changing the amplitude of the RF signal, the power or intensity of the laser can be controlled. The diffraction efficiency of an AOM indicates the percentage of the incident beam that can be deflected into the first diffraction order.

AOM 1 is a M1135-T80L from ISOMET, which has a separation angle of 21.0 mrad

between the zeroth and the first diffraction order. AOM 1 is able to withstand optical powers up to 100 W and RF powers up to 6 W. It is water cooled to minimize thermal lensing [23]. The zeroth order Bragg diffraction of AOM 1 propagates towards a polarizing beam splitter (PBS) cube. The amount of light that is transmitted and reflected by the cube depends on the polarization of the light. This is controlled by the waveplate located directly behind the out-coupler. The part of the zeroth order which is transmitted by the PBS is directed into a water cooled beam dump. The deflected zeroth order is directed towards AOM 2. This is a MTS80-A3-1064Ac from AA Optic Electronic, which has a separation angle of 130.0 mrad. The zeroth order of AOM 2 is also directed towards the water-cooled beam dump. Important to note is that the crystal of AOM 2 has been cut such that the zeroth order is deflected by the separation angle while the first order comes out undeflected. The diffraction efficiency for both AOM 1 and AOM 2 can be $> 85\,\%$. In order to achieve this diffraction efficiency, AOM 1 and AOM 2 need to be driven by $f \cong 80\,\text{MHz}$ and $f \cong 110\,\text{MHz}$, respectively.

Whenever an object is placed too close to the center of a Gaussian beam, truncation occurs which causes diffraction of the Gaussian beam. This diffraction is negligible when the separation between the object and the center of the Gaussian beam is $> 3w$, where w denotes the beam waist [26–28]. This means that in our experiment with a separation angle of 21.0 mrad and a beam waist of 1.61 mm, the zeroth and first order of AOM 1 can be separated at a minimum distance of 243 mm from AOM 1. For AOM 2 the minimum distance is 39 mm using a separation angle of 130.0 mrad and beam waist of 1.61 mm.

Both first orders of AOM 1 and AOM 2 are directed towards the top layer of the setup. As indicated in Figure 3.1, the first orders will propagate through holes drilled in the top layer. The first order of AOM 1 is used for the main beam whereas the first order of AOM 2 is used for the cross beam.

3.2.2 Top layer

Before we reach the top layer, both first orders pass through a pair of lenses, located in the vertical path between the bottom and top layer. These lenses are required to compensate for the divergence of the beam coming out of the out-coupler. The pair of lenses consists of a meniscus lens and a convex lens with focal lengths of -400 mm and 400 mm, respectively. The beam waist of the main beam after the vertical pair of lenses is $w = 1.1 \pm 0.1$ mm. The beam height on the top layer is 54.8 ± 0.5 mm. The bottom and top layer are separated by a distance of 131.5 ± 0.5 mm. In Figure 3.2 the top view of the top layer is given.

On the top layer, the first order of the main beam passes through a $\lambda/2$ waveplate and a PBS. Using the waveplate we are able to control how much light falls on a

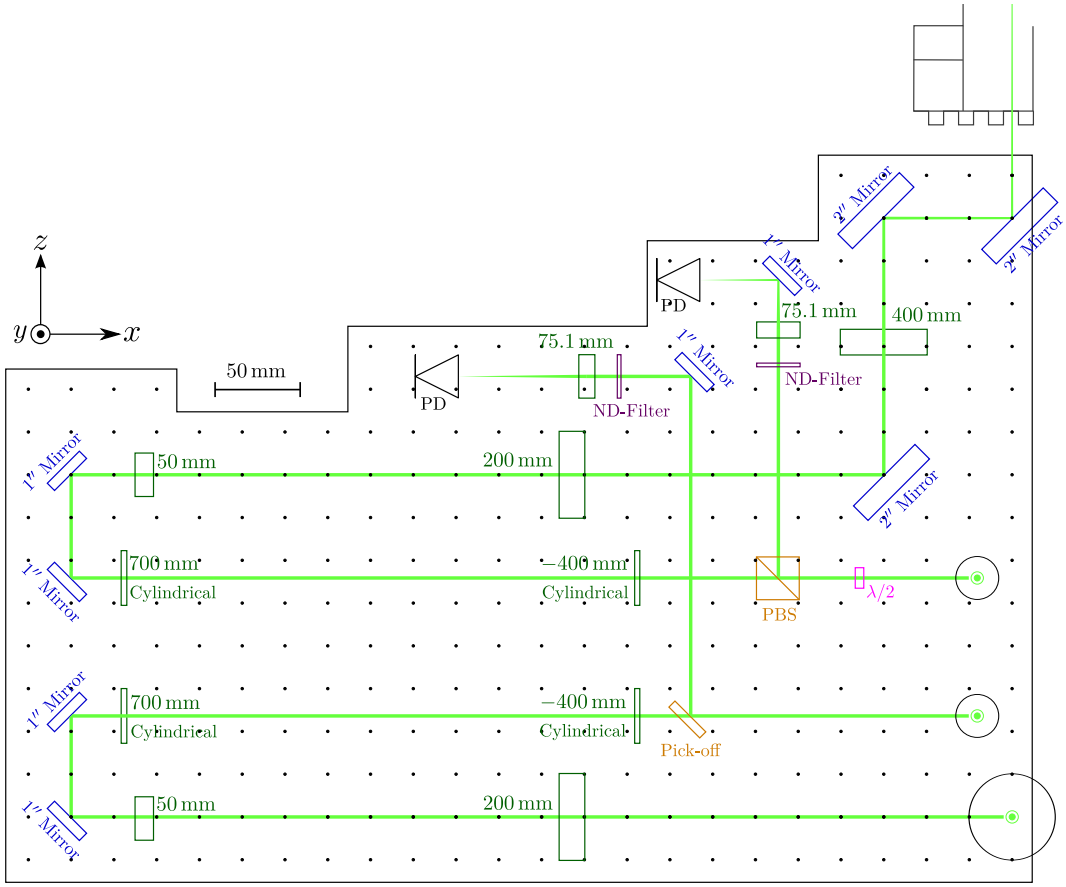

Figure 3.2: Top view of the top layer. Mirrors are depicted in blue, waveplates in pink, beam splitting elements in brown, ND-filters in purple, lenses in dark green, and the Gaussian laser beam in light green. The black circles are used to indicate that the beam is either coming from a different level or propagates towards one.

photodiode. The signal from the photodiode can be used as an error signal when controlling the power of the laser light. Even after the PBS, the laser intensity will saturate the photodiode. Hence, neutral density (ND) filters are used to further reduce the measured power.

The transmitted part of the light beam after the PBS passes through the first telescope. This telescope is cylindrical, increasing the beam waist only in one direction. For the cylindrical telescope a set of concave and convex lenses is used with focal lengths of $-400\,\mathrm{mm}$ and $700\,\mathrm{mm}$, respectively. This results in a lens separation of $300\,\mathrm{mm}$ and a magnification of 1.75. The lenses are placed such that the beam waist is increased in the y-direction.

Subsequently, the main beam is passed through a normal telescope increasing the beam waist in both directions equally. This is achieved using a pair of achromatic

lenses with focal lengths of 50 mm and 200 mm, respectively. The lens combination results in a lens separation of 250 mm and a magnification of 4. Using a final lens, a focus at the position of the MOT is obtained. The focal length of the final lens is 400 mm. With the theoretical magnifications of 1.75 and 4, a beam waist of $w_x = 4.4\,\text{mm}$ in the x-direction and $w_y = 7.7\,\text{mm}$ in the y-direction is obtained before the final lens. This would result in a focus of $w_{0,x} = 31\,\mu\text{m}$ in the x-direction and $w_{0,y} = 17.7\,\mu\text{m}$ in the y-direction. Note that these numbers indicate beam waists. The focus that we obtain experimentally has a beam waist of $w_{0,x} = 40\,\mu\text{m}$ in the x-direction and $w_{0,y} = 23.5\,\mu\text{m}$ in the y-direction. This is acceptable for the experiment. The mismatch between the theoretical and experimental foci is because the magnifications of the telescopes are not reached. This could either be due to alignment, because the focal lengths of the lenses differ from their theoretical values, or because the M^2 of the beam has deteriorated along the beam path. As the beam waists were good enough, no time was invested in investigating this further.

The error-signal for the cross beam is obtained using a beam pick-off. Since the polarization is fixed due to the PBS on the bottom layer, an additional wave-plate is not required. To ensure the photodiode is not saturated, a ND-filter is used. After the beam pick-off, the transmitted beam passes through two sets of telescopes; a cylindrical telescope, and a normal telescope. Since the focus of the cross beam is also elliptically shaped, it is important to rotate it such that it is perpendicular to that of the main beam. Atoms escaping the focus of the main beam in the axial direction are trapped in the radial direction of the focus of the cross beam. To this end, the beam waist of the cross beam is thus increased in the x-direction. For the cross beam a similar focus is obtained with respect to the main beam. This will enable us to achieve a high atom density in the focus of the main beam before displacing the atoms, which will enable efficient evaporative cooling, should it be necessary.

Until this point we have been talking about a horizontal movement of atoms using an ODT. The horizontal movement of the atoms is achieved by rotating the last mirror in front of the 3D-chamber. The rotation of the mirror will displace the focus and thus the atoms towards the sample stage. In Figure 3.2 the rotation stage is not included since the focus of this thesis is on the preliminary measurements of the main beam. These do not include any movement of atoms. Hence, a static mirror suffices. However, the basic idea of the movement is illustrated in Figure 3.3. It will be achieved using a MI-660.45 rotation stage from Physik Instrumente. The atoms will be positioned at the sample stage.

While writing this thesis, the atoms have been successfully moved horizontally and back with high efficiency. The results are discussed by Meyer Viol [28].

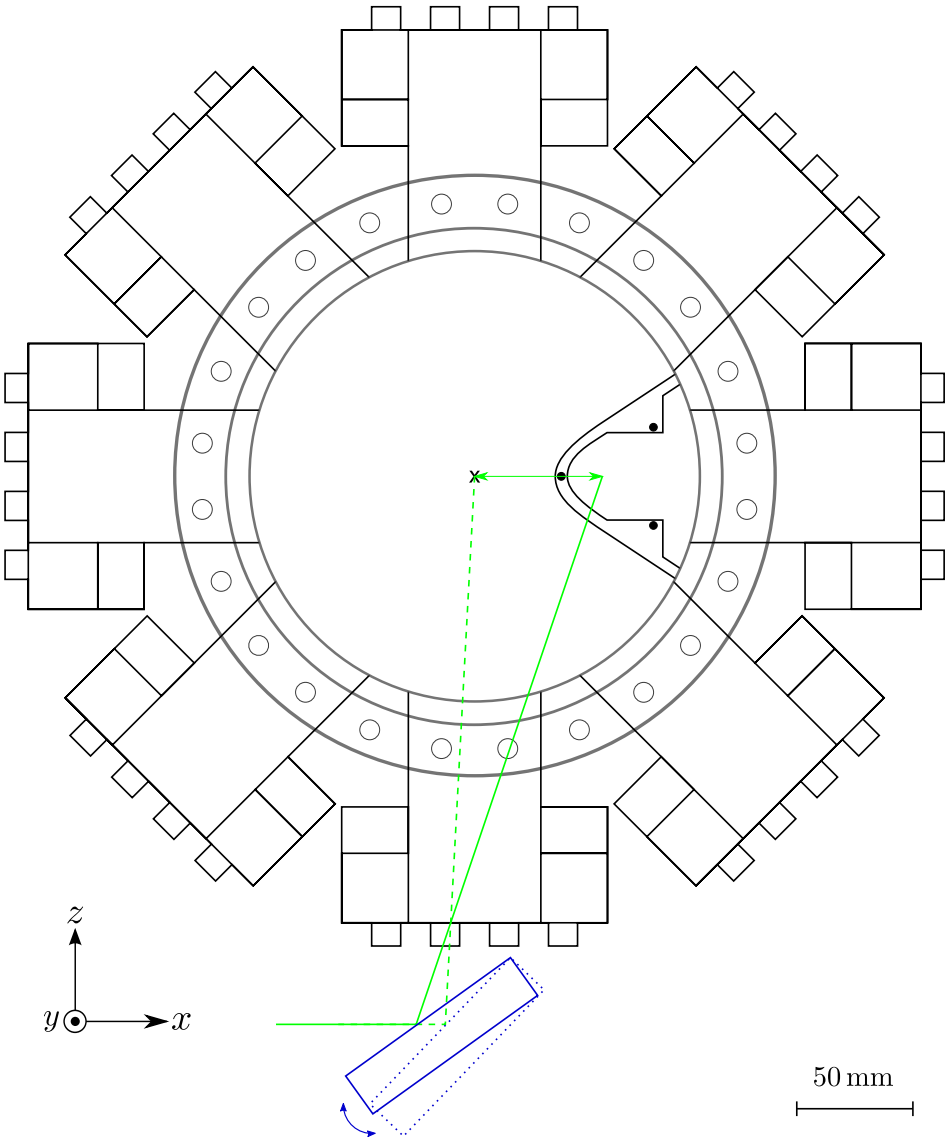

Figure 3.3: Top view of a schematic representation of the rotation stage. The rotation stage is denoted by a single mirror which is rotated.

3.3 Experiment

With the experimental setup described in Section 3.2, the lifetime of the atoms in the ODT is measured for different laser powers ranging from 5.9 W to 10.4 W. Also, the influence of different parameters on the lifetime is investigated. The parameters are explained in more detail in Section 3.3.4.

In this subsection the experiment is described, explaining which imaging techniques

are used and how the images are obtained. Also, the experimental control sequence is discussed.

3.3.1 Imaging techniques

With our imaging setup, discussed in Section 3.3.3, we are able to perform both fluorescent- and absorption imaging. Both can be used to determine the number of atoms in the ODT. As will be explained in this section, the signal obtained using fluorescent imaging is weak compared to that of absorption imaging. Therefore, the number of atoms in the ODT is determined using absorption imaging. The number of atoms in the MOT is obtained from their fluorescence. Since the fluorescent signal of the MOT is non-destructive, this allows us to measure the number of atoms in the MOT before loading the ODT and the atoms loaded into the ODT.

In fluorescent imaging an atom cloud is excited using near resonant light such that the scattering rate is maximal. As explained in Section 2.1.1, the scattering of photons is isotropic. Therefore, only a small fraction of the entire fluorescent signal can be captured under a solid angle. This results in a weak signal that can be captured compared to the total fluorescent signal. To determine the number of atoms in the ODT and MOT simultaneously, the fluorescent signal is captured using a photodiode. The measured voltage on the photodiode can be converted into a number of atoms. This is discussed in more detail in Section 4.1.2.

In absorption imaging a cloud of atoms is illuminated with resonant light e.g. the probe beam. Atoms present in the probe beam scatter photons out of this beam. This results in a shadow which can be imaged on a CCD camera. The amount of light absorbed gives the optical column density (ρ_{O}) of the cloud. It can can be written as $\rho_{\mathrm{O}} = \sigma l N$, where σ denotes the absorption cross section, l the path length i.e. the distance travelled by the light through the atoms, and N the density of absorbed atoms. The relation between the optical column density and transmission T is given by Lambert-Beers law

$$T = \frac{I}{I_0} = \mathrm{e}^{-\rho_{\mathrm{O}}}, \tag{3.35}$$

where I denotes the transmitted intensity, and I_0 the intensity of the probe beam.

For the optical column density it is important not to saturate the atoms with the probe beam as atoms scatter less light when saturated. To this end, the on-resonance saturation parameter $s_0 = I_0/I_{\mathrm{sat}}$ needs to be much smaller than one. For a probe beam with a beam waist of $w = 7.4\,\mathrm{mm}$, a power of $P = 150\,\mu\mathrm{W}$, and a saturation intensity for the atoms of $I_{\mathrm{sat}} = 1.7\,\mathrm{mW/cm^2}$, the on-resonance saturation parameter equals $s_0 = 0.05$.

To obtain the optical column density, three images are taken with a CCD camera for each run of the experiment. The first shot we take is of the transmitted probe

beam and the atoms in the ODT. The second shot is of only the probe beam. The third and final shot is without probe beam and atoms, which serves as a background image.

By combining the three different shots and Equation 3.35, the optical column density per pixel is given by

$$\rho_{\mathrm{O}} = -\ln\left(\frac{I_{\mathrm{atoms}} - I_{\mathrm{dark}}}{I_{\mathrm{flat}} - I_{\mathrm{dark}}}\right), \tag{3.36}$$

where I_{atoms} denotes the intensity of shot one with atoms and probe beam, I_{flat} the intensity of only the probe beam, and I_{dark} the intensity without atoms and probe beam. By taking the summation of the optical column density over all pixels the number of atoms can be related to a number of atoms.

3.3.2 CCD camera

For future experiments, a couple of thousand of atoms will be positioned above a gold sample. To measure such weak signals a very sensitive detector is required. To this end, the iXon 885 from Andor was acquired. We used this camera to determine the number of atoms in the ODT. The camera has a on-chip electron multiplier and can be cooled to $-90\,^{\circ}\mathrm{C}$ using a combination of thermoelectric and water cooling. For the measurements performed on the ODT, the temperature of the camera was set to $-70\,^{\circ}\mathrm{C}$. This was achieved using a combination of thermoelectric and forced air cooling.

The camera has a charged-coupled-device (CCD) chip with 1004 x 1002 active pixels. The pixels have an active area pixel well depth of 30.000 electrons and a dynamic range of 14 bits. This means that one graylevel of the camera corresponds to about two electrons. With a quantum efficiency (QE) of 50 % this corresponds to four photons which are required to register a "click". Given the energy of a photon at $\lambda = 780\,\mathrm{nm}$ and a pixel area of $8 \times 8\,\mu\mathrm{m}^2$, the click of the pixel corresponds to a fluence of $0.40\,\mathrm{pJ/cm^2}$. With an exposure time of $200\,\mu\mathrm{s}$, this is equal to a minimum intensity of $1.99 \times 10^{-6}\,\mathrm{mW/cm^2}$. The maximal intensity is given by the intensity at which a pixel is saturated. As we have seen, two photons are required per electron. With an electron well depth of 30.000 electrons this corresponds to 60.000 photons which are required to saturate a pixel. The corresponding fluence is given by $2.39 \times 10^{-2}\,\mu\mathrm{J/cm^2}$. This results in an intensity of $1.19 \times 10^{-1}\,\mathrm{mW/cm^2}$ for an exposure time of $200\,\mu\mathrm{s}$. The intensity of the probe beam is thus 36 % of the intensity required to saturate a pixel.

The images, discussed in Section 3.3.1, are taken using the built-in kinetics mode. This mode is able to capture a sequence of single images, or a sequence of accumulated images, and transfer them into the memory of the camera. Note that this mode is equivalent to manually taking single or accumulated images. With the kinetics

mode however, all images can be read out simultaneously instead of reading them out separately. The kinetics mode thus allows for a faster operation. For a kinetic acquisition, the exposure time, number of images, and the delay between the images are required. In the experiment, the delay between images is controlled using an external trigger. The timing of this trigger is discussed in Section 3.3.4.

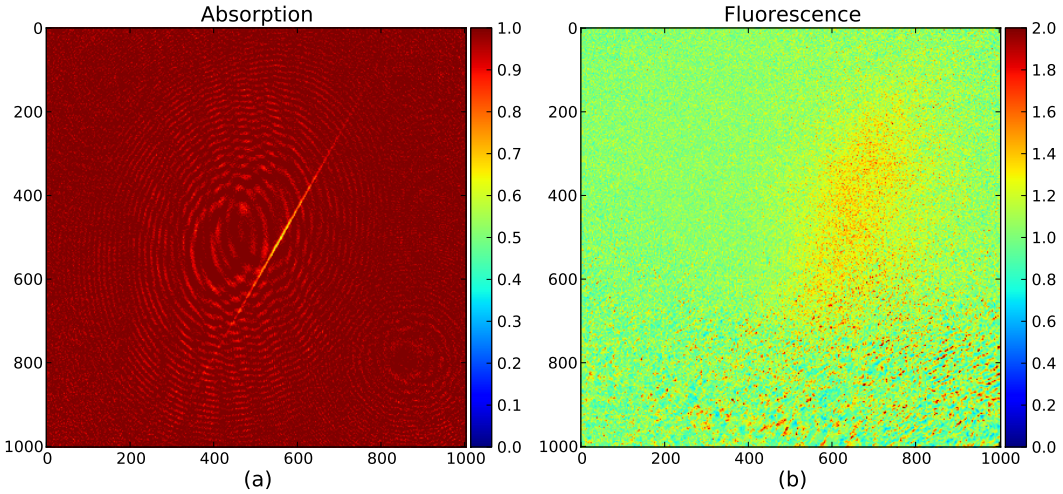

Figure 3.4: Images taken with the CCD camera. (a) Absorption image of atoms in the ODT. Note that the atoms have a higher intensity, the rings in the background of the image are optical artifacts. (b) Fluorescence image of the atoms trapped by the ODT. Note that with respect to the absorption image, the cloud of atoms is expanding.

As discussed in Section 3.3.1, the CCD camera is used for absorption imaging while a photodiode is used to measure the fluorescent signal of the MOT. However, we are also able to do fluorescence imaging of the atoms in the ODT using the CCD camera. The results can be seen in Figure 3.4(b). For the fluorescent image, the atoms in the ODT are illuminated using the MOT beams. The light of the MOT beams is controlled using a mechanical shutter which takes 35 ms to open. The fluorescent image is purely to illustrate the principle. We did not invested time in the sequence for taking the image which results in an expanding cloud of atoms, as can be seen in Figure 3.4(b). The rings visible in the absorption image are fringes due to dust in the imaging path. The region of high intensity at the bottom of the fluorescent image is due to unwanted reflections. Since we are using absorption imaging, the origin of the reflections was not investigated.

3.3.3 Imaging setup

The imaging setup is shown in Figure 3.5. The probe beam is introduced into the imaging setup via a single mode fiber with a mean field diameter of 4.9 µm. Note

that the out-coupler of the probe beam is not included in Figure 3.5. After the out-coupler, the probe beam is collimated by a lens placed a focal length away. The focal length of the lens is 75 mm. This results in a collimated beam waist of 7.4 mm. The resulting beam is used to illuminate the atoms in the ODT. The probe beam is directed from underneath the chamber through the center of the chamber, thus hitting the atoms in the ODT. Note that the probe beam makes a slight angle. This is inevitable because the vertical optical axis through the center of the chamber is utilized for the MOT beams. Above the chamber the probe beam and the shadow of the atoms are imaged on the CCD camera using a lens with a focal length of $f = 150\,\text{mm}$. Note that a magnification of the atoms is obtained because the lens is not placed a focal length from the atoms in the ODT. The exact magnification is discussed in Section 4.1.1.

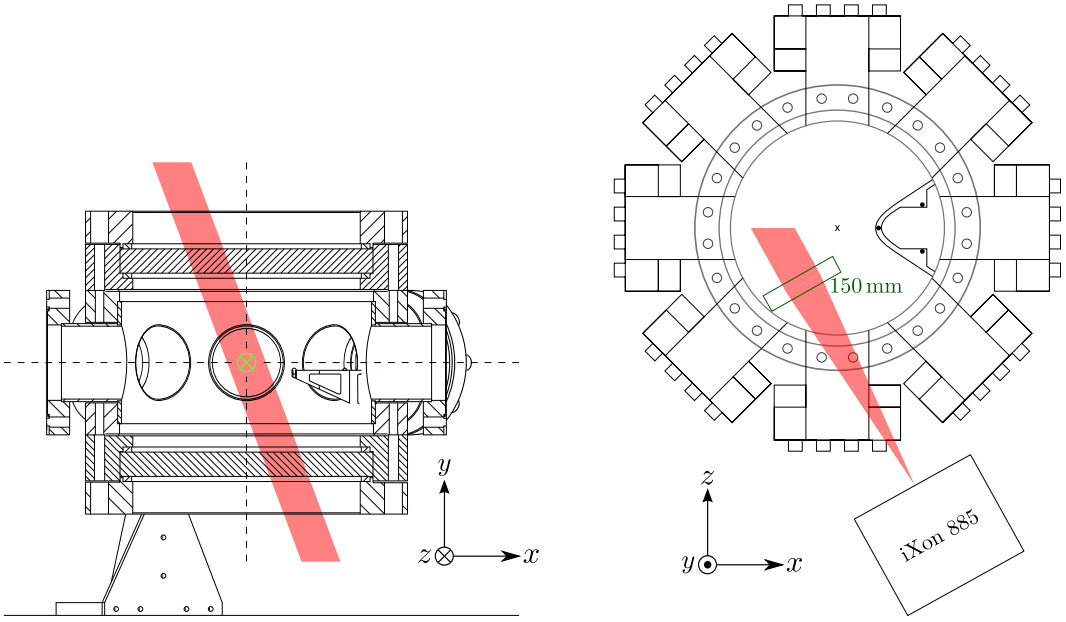

Figure 3.5: Imaging setup not to scale. (a) Side view of the imaging setup, where the path of the probe beam is denoted in red. The ODT beam, trapping the atoms, is denoted by light green. (b) Top view of the imaging setup from which we are able to see the probe beam being focused onto the CCD camera..

3.3.4 Experimental control

For the experimental control we are using a computer controlled sequence board, which we refer to as "The Puppet Master". The Puppet Master has twenty-four digital channels. Six channels are used for the experiments described in this thesis.

In Figure 3.6, the six channels are shown schematically. Note that this figure is not to scale. In Table 3.2, the parameters and times are given as an indication of their order of magnitude.

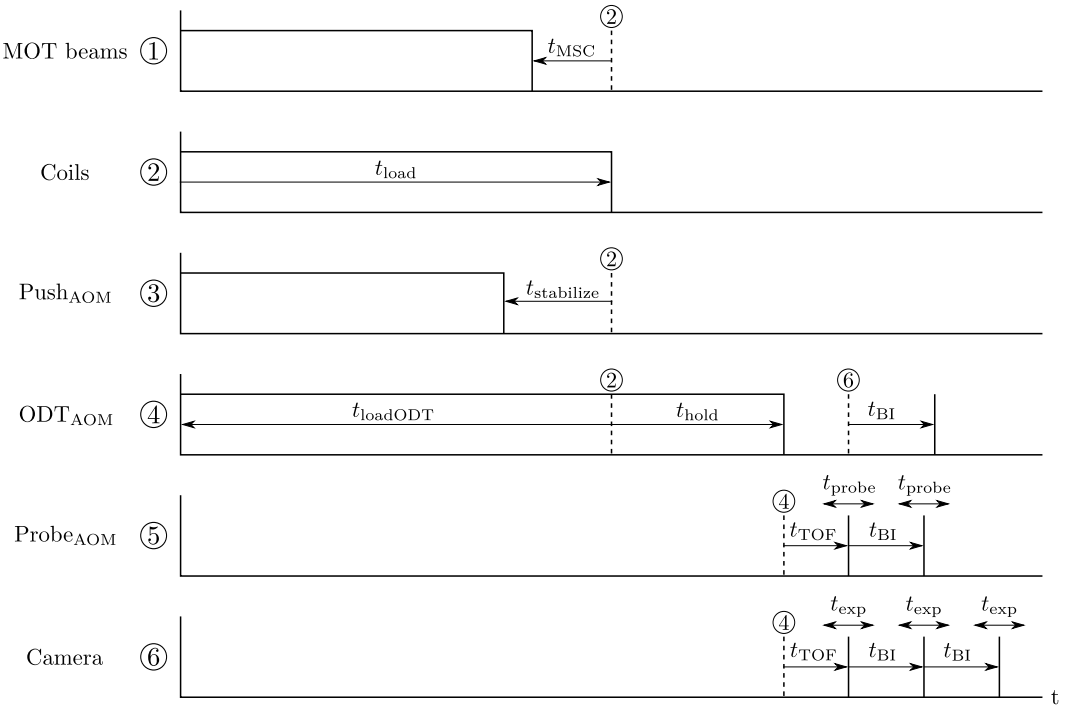

Figure 3.6: Experimental sequence for absorption imaging. With the arrows, the times are indicated. The channels of "The Puppet Master" are denoted by the numbers one to six. The numbers are also used to indicate linked events.

We start the experiment by turning both the MOT beams and the coils on, thus creating a MOT. This is indicated in Figure 3.6 by Channels 1 and 2 of the puppet master, respectively. Note that the light of the MOT beams is regulated via a mechanical shutter. The MOT is loaded for a time t_{load}, after which it is turned off and the atoms are only trapped by the ODT. To turn the MOT off, the MOT beams and the coils are turned off simultaneously. Since the mechanical shutter takes 15 ms to fully close, the signal given to the shutter is sent 15 ms before the signal for the coils. The closing time of the shutter is indicated by t_{MSC} and is linked to turning the coils off.

As indicated in Section 2.2.4, the reference laser was split up into two parts: a reference beam, and a beam which is split once more into a push- and probe beam. The beam that is split off from the reference beam passes through an AOM to shift the frequency by 105 MHz. This AOM is referred to as the main AOM. After the main AOM, the first order is split further into two parts for the push- and probe

beam. Both beams pass through AOMs which are referred to as the push- and probe AOM. They are both operated at 106.8 MHz in order to shift the frequency of both the push- and probe beam to resonance ($F' = 3$).

Property	Symbol	Value
Time to close the MOT shutter	t_{MSC}	$-15\,\mathrm{ms}$
Loading time MOT	t_{load}	$2500\,\mathrm{ms}$
MOT stabilization time	$t_{\mathrm{stabilize}}$	$-500\,\mathrm{ms}$
Time of flight	t_{TOF}	$2\,\mu\mathrm{s}$
Loading time ODT	t_{loadODT}	$-2500\,\mathrm{ms}$
Holding time ODT	t_{hold}	$100\,\mathrm{ms}$
Time probe beam on	t_{probe}	$100\,\mu\mathrm{s}$
Exposure time camera	t_{exp}	$200\,\mu\mathrm{s}$
Time between images	t_{BI}	$60\,\mathrm{ms}$

Table 3.2: Example of the times used in the control sequence of the experiment.

While loading the MOT, the push beam is required for a faster loading rate. To this end, the push AOM is turned on and off by Channel 3 of the puppet master. Note that for the duration of the experiment, the main AOM is not turned off. Also, during loading of the MOT, the ODT is operated by turning AOM 1 on using Channel 4. By turning the ODT on while loading the MOT, atoms are already loading into the ODT. The loading time of the ODT t_{loadODT} is linked to turning the coils off and thus turning off the MOT. Therefore, t_{loadODT} uses negative times. We are also able to link a positive time to turning the MOT off. For the ODT this will be the holding time t_{hold}, which denotes the time the atoms are solely trapped by the ODT. Typical times for t_{loadODT} and t_{hold} are $-2500\,\mathrm{ms}$ and $100\,\mathrm{ms}$ to $4500\,\mathrm{ms}$, respectively.

After the atoms are released from the trap, the three images are taken as described in Section 3.3.1. Before the first image however, a short delay is introduced denoted by t_{TOF}, where "TOF" denotes time-of-flight. This delay is to prevent the absorption frequency of the atoms to shift due to the ac Stark shift, induced by the ODT beam [24]. This delay is $2\,\mu\mathrm{s}$ long. For the images, the probe beam and camera are turned on using Channels 5 and 6, respectively. The probe beam is pulsed twice, first for the atoms image and the second time for the flat image. In both cases the probe time equals $t_{\mathrm{probe}} = 100\,\mu\mathrm{s}$. The camera is triggered three times, the first two times to capture the probe light and the last time background image. The exposure time of the camera is set to $t_{\mathrm{expose}} = 200\,\mu\mathrm{s}$. Due to the frame rate of the camera, the time in between consecutive images is chosen to be $t_{\mathrm{BI}} = 60\,\mathrm{ms}$. Note that to include possible stray light from the ODT, the ODT is flashed on for the flat image.

4 Optical Dipole Trap: Results

In this section the results of the ODT are discussed. This section is divided into two parts. In Section 4.1, the number of atoms from both the absorption imaging with the CCD camera and the fluorescent signal on the photodiode are calculated to calibrate the measurements. In Section 4.2, the results of the lifetime of the atoms in the ODT are discussed.

4.1 Analysis

4.1.1 Number of atoms in the optical dipole trap

As mentioned in Section 3.3.1, the number of atoms can be derived from the optical column density. To obtain the optical column density, the intensity was measured using a CCD camera. The optical column density is defined by Lambert-Beers law

$$\rho_{\mathrm{O}} = -\ln(T) = -\ln\left(\frac{I_{\mathrm{atoms}} - I_{\mathrm{dark}}}{I_{\mathrm{flat}} - I_{\mathrm{dark}}}\right), \tag{4.1}$$

where I_{atoms} denotes the intensity of the image with atoms and probe beam, I_{flat} the intensity of only the probe beam, and I_{dark} the intensity without the probe beam.

An image of the atoms after applying Equation 4.1 is shown in Figure 4.1(a). Ideally, the negative logarithm of the transmission T is zero for the background. By summing over all the pixels, the optical column density of the light path trough the atom cloud is obtained.

However, the images obtained in the experiment show fringes and shot-to-shot background fluctuations. The influence of the fringes and background fluctuations on the optical column density is reduced by placing a mask over the atoms. For an accurate mask, both the angle that the atom cloud makes with respect to the image and the width of the atom cloud need to be determined.

The angle is found by locating the x- and y-coordinates of the first 1000 maximal optical column density values of the atom cloud in Figure 4.1(a). Due to the width of the atom cloud, multiple x-coordinates exist for one y-coordinate. The multiple x-coordinates are weightedly averaged by

$$x_{\mathrm{weighted}} = \frac{\sum_i \rho_{\mathrm{O},i} y_i}{\sum_i \rho_{\mathrm{O},i}}, \tag{4.2}$$

where y_i and $\rho_{\mathrm{O},i}$ denote the y-coordinate and the optical column density value of pixel i, respectively.

By fitting a linear line to the obtained weighted x- and y-coordinates the angle is determined. In this case the angle is found to be $60.37° \pm 0.11°$.

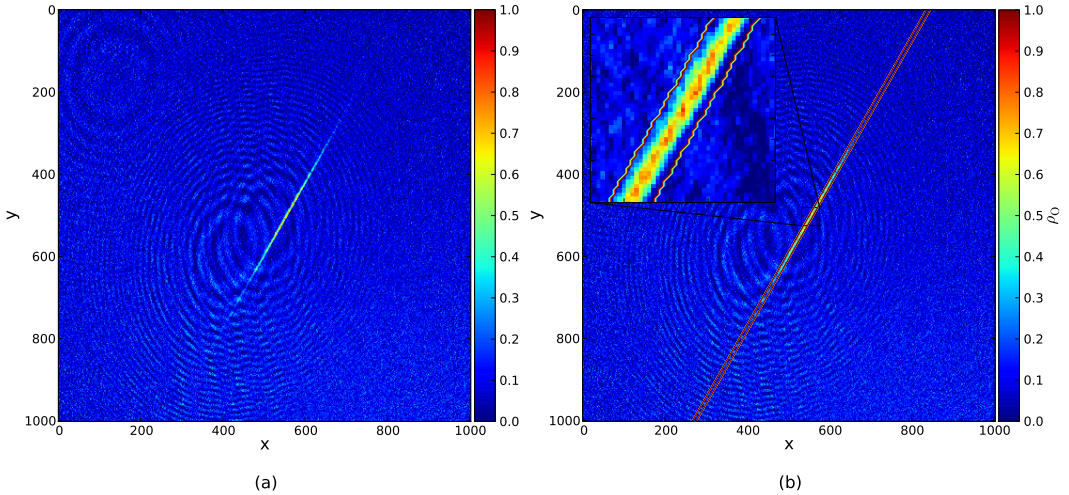

Figure 4.1: Absorption images obtained with the CCD camera. (a) Optical column density of the absorption image obtained via minus the logarithm of the transmission. (b) A mask is placed over the atom cloud in (a) to obtain the optical column density by excluding shot-to-shot optical artifacts and background fluctuations.

From the 1000 maximal optical column density values we also note that the atom cloud spans 8 pixels. The mask width is therefore chosen to be 11 pixels. In Figure 4.1(b), the mask is placed over the atoms from Figure 4.1(a). As observed during different experiments, the angle does not change without changing alignment. Therefore, the angle of the atom cloud is determined once for all measurements. This saves 10 s to 15 s of computation time for each determination of the number of atoms in the ODT.

The mask is placed over the pixels with the highest optical column density. However, for long holding times i.e. 3.5 s and higher, the number of atoms becomes so low that the maximum could be given by the fringes or the background fluctuations. To this end, each measurement is taken five times. By averaging these images, the fringes and background influences are decreased. Using the averaged image, the center of the atom cloud can now be determined for long holding times.

With the center of the atom cloud now known, the mask is placed over this center for each of the five individual images. The optical column density of each image is determined by summing the optical column density per pixel over the number of pixels in the mask. Besides determining the center of the atom cloud, the five measurements are also used to obtain the statistical error in our measurement.

The background signal is unequal to zero. It thus introduces an offset with respect to the optical column density of the atoms. Therefore, the background signal is determined and is subtracted from the optical column density of the atoms. Hence, the optical column density of the atoms is normalized to zero. The background signal

is also determined using a mask. This mask is required to exclude regions where the fringes and background fluctuations occur most frequently. The mask stretches from the lower left corner to the upper right corner of the absorption image. It utilizes the same angle as the mask placed over the atoms. The background signal of each pixel is summed over all the pixels in the mask. By scaling the total background signal to the number of pixels in the atom mask, the optical column density of the atoms can be normalized.

With the normalized optical column density of the atoms now known, the number of atoms can be obtained by

$$N_{\mathrm{ODT}} = \frac{M A_{\mathrm{pixel}}}{\sigma} \sum_n \rho_{\mathrm{O}} \left(x_n, y_n\right), \tag{4.3}$$

where n denotes the number of pixels, A_{pixel} the pixel area, M the magnification, and σ the absorption cross-section.

The absorption cross-section is a measure for the probability of an absorption process. It thus depends on the detuning of the probe beam and the on-resonance saturation parameter. Since the probe beam is operated at resonance the detuning equals $\Delta = 0$. The absorption cross-section is given by [29–31]

$$\sigma = \frac{\sigma_0}{1 + s_0}, \tag{4.4}$$

where $s_0 = 0.05$, and $\sigma_0 = 3\lambda^2/2\pi$ denotes the resonant absorption cross-section [22, 32].

The images taken with the camera are magnified. This is because the atoms are not imaged at a focal length distance from the lens and the camera. The magnification can be expressed by

$$M = \frac{u}{u'}, \tag{4.5}$$

where $u = 277.5 \pm 0.5\,\mathrm{mm}$ denotes the distance from the imaging lens to the chip of the CCD camera, and u' the distance of the atom cloud to the imaging lens.

An expression for u' is obtained using the object-image relationship [33]

$$\frac{1}{u} + \frac{1}{u'} = \frac{1}{f}, \tag{4.6}$$

where $f = 150\,\mathrm{mm}$ denotes the focal length of the imaging lens.

Combining Equations 4.5 and 4.6, the magnification can be expressed as

$$M = \frac{u - f}{f}. \tag{4.7}$$

From this, we find that $M = 0.85$.

From the five measurements, the standard deviation is calculated as the square root of the average of the squared deviations from the mean [34]. Thus

$$\sigma_N = \sqrt{\frac{1}{P}\sum_{i=1}^{P}(N_i - \bar{N})^2}, \tag{4.8}$$

where N denotes the number of atoms for a measurement P, and $\bar{N}$ the mean number of atoms.

4.1.2 Number of atoms in the magneto-optical trap

As explained in Section 3.3.1, the number of atoms in the MOT is determined from the fluorescence signal, captured by a photodiode. The strength of a fluorescence signal depends on the number of atoms and the photon scattering rate γ_p. As discussed in Section 2.1.1, the photon scattering rate is given by

$$\gamma_\mathrm{p}(\Delta) = \left(\frac{\gamma}{2}\right)\frac{s_0}{1 + s_0 + 4\left(\Delta/\gamma\right)^2}. \tag{4.9}$$

As can be seen from Equation 4.9, the photon scattering rate saturates to $\gamma/2$ for high intensities. For a given detuning, the fluorescence signal captured by the photodiode is given by

$$N_\mathrm{p} = \gamma_\mathrm{p}(\Delta) t_\mathrm{exp} N_\mathrm{MOT}, \tag{4.10}$$

where N_p denotes the number of photons perceived by the photodiode, N_MOT the number of atoms in the MOT, and t_exp the exposure time of the photodiode.

The number of photons perceived by the photodiode for a time t_exp can be expressed by dividing the total power of the photons by the energy of a single photon $E_\mathrm{p} = \frac{hc}{\lambda}$, where $\lambda = 780\,\mathrm{nm}$. The total power can be determined by dividing the measured voltage V by the responsivity η and the gain ζ of the photodiode [35]. We obtain

$$\frac{N_\mathrm{p}}{t_\mathrm{exp}} = \frac{1}{\eta\zeta E_\mathrm{p}} V. \tag{4.11}$$

As mentioned in Section 3.3.1, the fluorescent signal of the atoms is isotropic. Only a small fraction of the photons is captured by the photodiode under a solid angle. To take this into account, the lens that focusses the fluorescent signal onto the photodiode is approximated by a two-dimensional circle. The area of the lens equals $A_\mathrm{lens} = \pi r^2$, where $r = 12.7\,\mathrm{mm}$ denotes the radius of the lens. The area of the total fluorescent signal is given by $A_\mathrm{shell} = 4\pi R^2$, where $R = 145.5 \pm 7.3\,\mathrm{mm}$ denotes the distance from the center of the MOT to the lens. The number of atoms in the MOT can thus be described by

$$N_\mathrm{MOT} = \frac{A_\mathrm{shell}}{A_\mathrm{lens}}\frac{1}{\eta\zeta E_\mathrm{p}}\frac{1}{\gamma_\mathrm{p}} V. \tag{4.12}$$

The photodiode has a responsivity of $\eta = 0.52 \pm 0.02\,\mathrm{A/W}$ and the photodiode amplifier has a gain of $\zeta = (2.38 \pm 0.05) \times 10^5\,\mathrm{V/A}$ [35]. The values for the detuning and the on-resonance saturation parameter are given by $\Delta = -17.99\,\mathrm{MHz}$ and $s_0 = 23.9$, respectively. The number of atoms in the MOT as a function of the measured voltage V on the photodiode is thus expressed as

$$N_{\mathrm{MOT}}(V) = (1.38 \pm 0.07) \times 10^{10} \times V. \tag{4.13}$$

Note that the number given by Equation 4.13 is the lower limit of the number of atoms in the MOT. When the atom cloud is very dense, the outer atoms will shield the fluorescent signal of the inner atoms.

4.2 Atomic lifetime in the optical dipole trap

In this subsection the lifetime of the atoms in the ODT is discussed. This subsection is divided into two parts. In Section 4.2.1, the experimental conditions are described under which the lifetime of the atoms in the ODT was measured. In Section 4.2.2, the number of atoms in the ODT are measured as a function of the holding time. The resulting decay of the atoms is referred to as the "lifetime" of the atoms in the ODT.

4.2.1 Experimental conditions

During the lifetime measurement of the atoms in the ODT, the 2D-MOT was operated at laser powers of $P_{\mathrm{2D,cool}} = 182.6\,\mathrm{mW}$ and $P_{\mathrm{2D,rep}} = 4.5\,\mathrm{mW}$ for the cool- and re-pump laser, respectively. The atoms from the 2D-MOT are transferred into the 3D-MOT using a push beam with a laser power of $P_{\mathrm{push}} = 257.6\,\mu\mathrm{W}$. With this laser power the loading time for the 3D-MOT equals $t_{\mathrm{load}} = 2\,\mathrm{s}$. The cool- and re-pump laser of the 3D-MOT are $P_{\mathrm{3D,cool}} = 70.4\,\mathrm{mW}$ and $P_{\mathrm{3D,rep}} = 3.2\,\mathrm{mW}$, respectively. The experimental conditions are summarized in Table 4.1.

For the magnetic field of the 2D-MOT, a current of 2.03 A was applied to the coils, resulting in a magnetic field gradient of 7.70 G/cm. The current applied to the 3D-coils was 15.00 A, yielding a magnetic field gradient of 16.01 G/cm. The current applied to the compensation coils was 2.3 A.

The probe beam has a power of $P_{\mathrm{probe}} = 147.6\,\mu\mathrm{W}$, resulting in an on-resonance parameter of $s_0 = 0.05$. The temperature for the camera was set at $T_{\mathrm{camera}} = -70.8\,^{\circ}\mathrm{C}$ which was achieved using a combination of thermoelectric- and forced air cooling.

In Section 4.1.2, the number of atoms in the MOT was derived as a function of the voltage measured by a photodiode. With the experimental conditions described in

Property	Symbol	Value
Camera temperature	T_{camera}	$-70.8\,^{\circ}\text{C}$
2D-MOT cooling laser power	$P_{\text{2D,cool}}$	188.9 mW
2D-MOT repump laser power	$P_{\text{2D,rep}}$	4.5 mW
3D-MOT cooling laser power	$P_{\text{3D,cool}}$	70.4 mW
3D-MOT repump laser power	$P_{\text{3D,rep}}$	3.2 mW
Laser power of the push beam	P_{push}	257.6 µW
Laser power of the probe beam	P_{probe}	147.6 µW
Coil	Current	Field gradient
2D-coils	2.03 A	7.70 G/cm
3D-coils	15.00 A	16.01 G/cm

Table 4.1: Experimental conditions for the lifetime measurements of the atoms in the ODT.

this section, the photodiode measured a voltage of $V = 2.91\,\text{V}$. The resulting number of atoms in the MOT is $N_{\text{MOT}} = (4.0 \pm 0.2) \times 10^{10}$ atoms.

4.2.2 Experimental results

In Section 3.3.4, the experimental control parameters were discussed. The values of the parameters used to determine the lifetime of the atoms are listed in Table 4.2.

Property	Symbol	Value
Time to close the MOT shutter	t_{MSC}	−15 ms
Loading time MOT	t_{load}	2500 ms
MOT stabilization time	$t_{\text{stabilize}}$	−500 ms
Time of flight	t_{TOF}	2 µs
Loading time ODT	t_{loadODT}	−2500 ms
Holding time ODT	t_{hold}	100 ms
Time probe beam on	t_{probe}	100 µs
Exposure time camera	t_{exp}	200 µs
Time between images	t_{BI}	60 ms

Table 4.2: Atomic lifetime parameters.

For the lifetime measurements, the holding time of the ODT was varied between 100 ms and 4500 ms in steps of 200 ms. The holding time was varied in an achronological order to introduce a disorder in any experimental drift. For each holding time, the power of the ODT laser was varied.

In Figure 4.2, the number of atoms in the ODT is plotted as a function of the holding

time for different laser powers. The end of loading the MOT is taken at $t = 0$. As can be seen from the figure, the number of atoms in the ODT decreases over time. For higher laser powers and thus deeper trap depths, a higher number of atoms is initially trapped. For all different trap depths, the final number of atoms ($t_{\mathrm{hold}} = 4500\,\mathrm{ms}$) is around $N_{\mathrm{ODT}} = 16\,000$ atoms. The number of atoms in an "empty" measurement i.e. without atoms trapped by the ODT equals $N_{\mathrm{ODT,empty}} = 10\,159 \pm 4876$ atoms.

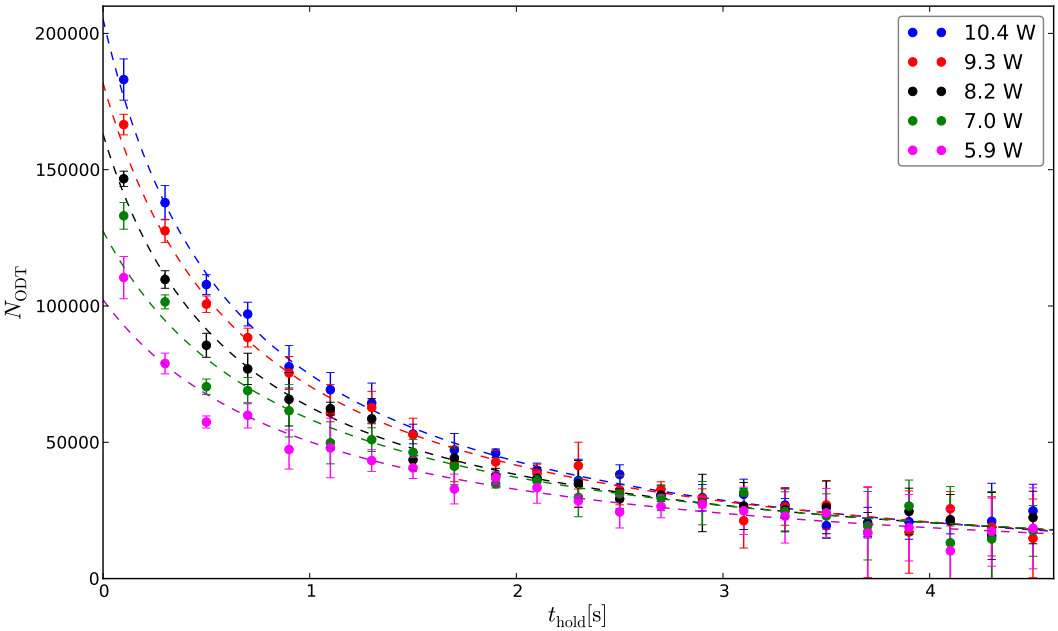

Figure 4.2: Lifetime of the atoms in the ODT for different trap depths. The dashed curves denote fits to the data by $\frac{dN}{dt} = -\alpha N - \beta' N^2$, where α denotes an exponential loss rate, and β' a collisional loss coefficient as compared to density dependent losses.

A differential equation to describe the atomic losses in an ODT can be given by [13, 36, 37]

$$\frac{dN}{dt} = -\alpha N - \beta' N^2, \tag{4.14}$$

where N denotes the number of atoms, α the rate coefficient for atomic losses due to collisions with untrapped atoms e.g. the background gas, and $\beta' = \beta V_{\mathrm{eff}}$ the two-body losses e.g. collisions between two trapped atoms as compared to density dependent losses. The rate coefficient for two-body collisions is given by β and the effective volume by V_{eff}.

The effective volume can be determined by [37]

$$\frac{1}{V_{\mathrm{eff}}} \equiv \int d^3\vec{r}\,\rho\,(\vec{r})^2, \tag{4.15}$$

where $\rho\,(\vec{r})$ denotes the single-atom density distribution.

For temperatures far above the Bose-Einstein condensation temperatures, the density distribution can be expressed using classical statistics. It can be given by [37, 38]

$$\rho\left(\vec{r}\right) = \frac{1}{\pi^{3/2} R_x R_y R_z} \mathrm{e}^{-x^2/R_x^2} \mathrm{e}^{-y^2/R_y^2} \mathrm{e}^{-z^2/R_z^2}, \tag{4.16}$$

where R_i denotes the widths of the atom cloud. The widths are given by [37, 38]

$$R_i^2 = \frac{2k_\mathrm{B}T}{m\Omega_i^2}, \tag{4.17}$$

where Ω_i denotes the trap frequency. Note that the density distribution depends on the temperature T.

Combining Equations 4.15 and 4.16, the effective volume becomes

$$V_\mathrm{eff} = (8\pi)^{3/2} R_x R_y R_z. \tag{4.18}$$

Solving the differential equation given by Equation 4.14 yields

$$\int dt = \int dN \frac{1}{N\left(-\alpha - \beta' N\right)}, \tag{4.19}$$

$$t = \int dN \frac{\beta'}{\alpha\left(\alpha + \beta' N\right)} - \int dN \frac{1}{\alpha N}, \tag{4.20}$$

$$= \frac{1}{\alpha}\left[\ln\left(\frac{\alpha + \beta' N}{N}\right) + C\right], \tag{4.21}$$

where C denotes an integration constant.

The number of atoms, as a function of time is obtained by rewriting Equation 4.21

$$N(t) = \frac{\alpha}{\mathrm{e}^{\alpha(t-C)} - \beta'}, \tag{4.22}$$

$$= \frac{\alpha}{\gamma \mathrm{e}^{\alpha t} - \beta'}, \tag{4.23}$$

where for convenience $\gamma = \mathrm{e}^{-\alpha C}$.

The boundary condition is $N(t=0) = N_0$, where N_0 denotes the number of initially trapped atoms. Hence,

$$\gamma = \frac{\alpha + \beta' N_0}{N_0}. \tag{4.24}$$

Combining Equations 4.23 and 4.24 yields the number of atoms as a function of time, expressed in terms of N_0, α, and β'

$$N(t) = \frac{N_0 \mathrm{e}^{-\alpha t}}{1 + \frac{N_0 \beta'}{\alpha}\left(1 - \mathrm{e}^{-\alpha t}\right)}. \tag{4.25}$$

In Table 4.3, the fit results α, β', and N_0 are given for different trap depths.

Power	α	β'
10.4 W	$(1.57 \pm 0.74) \times 10^{-1}\,\mathrm{s}^{-1}$	$(7.05 \pm 1.76) \times 10^{-6}\,\mathrm{atoms}^{-1}\,\mathrm{s}^{-1}$
9.3 W	$(1.31 \pm 0.90) \times 10^{-1}\,\mathrm{s}^{-1}$	$(7.38 \pm 2.07) \times 10^{-6}\,\mathrm{atoms}^{-1}\,\mathrm{s}^{-1}$
8.2 W	$(5.91 \pm 6.71) \times 10^{-2}\,\mathrm{s}^{-1}$	$(9.10 \pm 1.73) \times 10^{-6}\,\mathrm{atoms}^{-1}\,\mathrm{s}^{-1}$
7.0 W	$(6.13 \pm 9.44) \times 10^{-2}\,\mathrm{s}^{-1}$	$(8.49 \pm 2.40) \times 10^{-6}\,\mathrm{atoms}^{-1}\,\mathrm{s}^{-1}$
5.9 W	$(5.06 \pm 9.51) \times 10^{-2}\,\mathrm{s}^{-1}$	$(9.38 \pm 2.68) \times 10^{-6}\,\mathrm{atoms}^{-1}\,\mathrm{s}^{-1}$
Power		N_0
10.4 W		$(2.1 \pm 0.5) \times 10^5$ atoms
9.3 W		$(1.8 \pm 0.4) \times 10^5$ atoms
8.2 W		$(1.6 \pm 0.3) \times 10^5$ atoms
7.0 W		$(1.3 \pm 0.2) \times 10^5$ atoms
5.9 W		$(1.0 \pm 0.2) \times 10^5$ atoms

Table 4.3: Fit results for the exponential loss rate α, and the collisional loss coefficient as compared to density dependent losses β' for different trap depths.

From Table 4.3, we notice that both α and β' are in the same order of magnitude for different trap depths. The order of magnitude is similar as observed in other experiments [13, 36, 37]. The high uncertainty that we observe for both loss rates is due to data limitation. For long holding times the number of atoms is in the same order of magnitude as the the number of atoms in an "empty" image. This results in large uncertainties in the calculated number of atoms for longer holding times.

As can be observed from Table 4.3, the two-body collisions depend on N. They dominate for small values of t_{hold}, whereas background collisions dominate for large values of t_{hold}. The exponential lifetime τ_{ODT} of the atoms is given by $\tau_{\mathrm{ODT}} = 1/\alpha$ [36]. For a laser power of 10.4 W we obtain a lifetime of $\tau_{\mathrm{ODT}} = 6.4 \pm 2.9\,\mathrm{s}$.

From Table 4.3 we also observe that the trap depth does not significantly influence the collisional loss coefficient β'. This indicates that the ratio of trapped atoms and the trap depth is in the same order of magnitude for all measurements. This ratio can be determined by dividing the number of initially trapped atoms by the trap depth. The results are listed in Table 4.4. Also included in the table is the ratio of initially trapped atoms over the number the number of atoms in the MOT. As can be seen from this table, the ratio N_0/U_0 is similar for different trap depths except for the lower laser powers. However, from the fit for these lower laser powers we note that the number of initially trapped atoms is estimated lower than expected when looking at the data points. A higher value for N_0 would mean that the ratio N_0/U_0 is more similar with respect to the other laser powers.

We also observe from Table 4.4 that the number of atoms that are trapped in the

Power	N_0/U_0	N_0/N_{MOT}
10.4 W	$(2.0 \pm 0.5) \times 10^5$ atoms/mK	$(5.13 \pm 0.26) \times 10^{-4}$ %
9.3 W	$(2.0 \pm 0.5) \times 10^5$ atoms/mK	$(4.55 \pm 0.23) \times 10^{-4}$ %
8.2 W	$(2.0 \pm 0.4) \times 10^5$ atoms/mK	$(4.08 \pm 0.20) \times 10^{-4}$ %
7.0 W	$(1.9 \pm 0.3) \times 10^5$ atoms/mK	$(3.19 \pm 0.16) \times 10^{-4}$ %
5.9 W	$(1.7 \pm 0.3) \times 10^5$ atoms/mK	$(2.56 \pm 0.13) \times 10^{-4}$ %

Table 4.4: Fit results for the initial number of atoms N_0, and the ratio N_0/N_{MOT} for different trap depths.

ODT from the MOT N_0/N_{MOT} is very low. For all different trap depths this ratio is in the order of 4×10^{-4} %. Note that the ODT is much smaller than the MOT.

5 Optical Conveyor: Theory and Test Setups

With the ODT, the atoms will be positioned above the sample at an estimated height of 5 mm. For the experiment, the final step remaining is to position the atoms several 100 nm above the sample surface. To this end, the atoms are transferred from the ODT into a standing-wave trap or optical conveyor. The optical conveyor is formed by two counterpropagating focused-beam traps.

This section is divided into three parts. In Section 5.1, the trap depth and the scattering rate are derived for the optical conveyor. Potential hopping or tunneling of atoms between lattice sites is also discussed. In Section 5.2, possible heating effects of the atoms in a "moving" standing-wave are investigated. With the heating effects known, the frequency sweeps are derived which can be used to displace the anti-nodes of the standing wave. In Section 5.3, the experiments used to test the performance of the optical conveyor are discussed.

5.1 Theory of atoms in moving optical lattices

By interfering two counterpropagating laser beams, which have the same frequency and intensity, a periodic intensity pattern is created. This is also referred to as an one-dimensional optical lattice [18–20]. The periodic intensity pattern is described by a standing wave. Here, the trap depth is determined by the intensity of the laser beams. As we have seen in Section 3.1.1, atoms are attracted towards regions of high intensity for red-detuned lasers. Therefore, the atoms are trapped in a 1D optical lattice with periodicity $\lambda/2$. Note that this is the case when the counterpropagating laser beams are perfectly collinear. The lattice spacing becomes larger when an angle between the beams is introduced.

In this subsection, the trap depth and the photon scattering rate are derived from the intensity distribution of the standing wave. The standing wave can be described as the sum of the two individual counterpropagating beams

$$\vec{E}(y,t) = \vec{E}_+(y,t) + \vec{E}_-(y,t), \tag{5.1}$$

where the $+$ and $-$ indices denote the direction of propagation. The propagation or axial direction of the conveyor is chosen in the y-direction. For a Gaussian beam the electric fields are given by

$$\vec{E}_\pm(y,t) = E_0 \mathrm{e}^{\frac{-\rho^2}{w(y)^2}} \mathrm{e}^{\imath(\pm k_\mathrm{L} y - \omega_\mathrm{L} t)}, \tag{5.2}$$

where E_0 denotes the amplitude of the electric field of one laser beam, $\mathrm{e}^{\frac{-\rho^2}{w(y)^2}}$ the Gaussian distribution of the electric field, $\mathrm{e}^{\imath(\pm k_\mathrm{L} y - \omega_\mathrm{L} t)}$ the propagation of the electric field in space and time, and $k_\mathrm{L} = 2\pi/\lambda$ and ω_L the wavenumber and frequency of

the laser, respectively. The propagation of the beam waist in the axial direction is denoted by $w(y)$.

For two counterpropagating Gaussian laser beams, the electric field can be written as

$$\vec{E}(y,t) = E_0 \mathrm{e}^{\frac{-\rho^2}{w(y)^2}} \left[\mathrm{e}^{\imath\left(k_{\mathrm{L},1}y - \omega_{\mathrm{L},1}t\right)} + \mathrm{e}^{-\imath\left(k_{\mathrm{L},2}y + \omega_{\mathrm{L},2}t\right)}\right]. \tag{5.3}$$

With the electric field given in Equation 5.3, the squared amplitude results in

$$\begin{aligned} |\vec{E}(y,t)|^2 &= E(y,t)E^*(y,t) && (5.4)\\ &= |E_0|^2 \mathrm{e}^{\frac{-2\rho^2}{w(y)^2}} \left[2 + 2\cos\left(\left[k_{\mathrm{L},1} + k_{\mathrm{L},2}\right] y + \left[\omega_{\mathrm{L},2} - \omega_{\mathrm{L},1}\right] t\right)\right] && (5.5)\\ &= 4|E_0|^2 \mathrm{e}^{\frac{-2\rho^2}{w(y)^2}} \cos^2\left(\left[k_{\mathrm{L},1} + \frac{\Delta k_{\mathrm{L}}}{2}\right] y + \frac{\Delta\omega_{\mathrm{L}}}{2} t\right), && (5.6) \end{aligned}$$

where $\Delta k_{\mathrm{L}} = k_{\mathrm{L},2} - k_{\mathrm{L},1}$ and $\Delta\omega_{\mathrm{L}} = \omega_{\mathrm{L},2} - \omega_{\mathrm{L},1}$ denote the difference in wavenumber and frequency between laser beam 1 and 2, respectively. Note that for equal frequency, wavelength and intensity a standing wave is obtained ($\Delta k_{\mathrm{L}} = \Delta\omega_{\mathrm{L}} = 0$).

For the optical conveyor, the detuning is very small ($\sim 20\,\mathrm{MHz}$). Therefore, Equation 5.6 can be written as

$$|\vec{E}(y,t)|^2 = 4|E_0|^2 \mathrm{e}^{\frac{-2\rho^2}{w(y)^2}} \cos^2\left(k_{\mathrm{L},1} y + \frac{\Delta\omega_{\mathrm{L}}}{2} t\right), \tag{5.7}$$

where $2k_{\mathrm{L},1} + \Delta k_{\mathrm{L}} \approx 2k_{\mathrm{L},1}$ because $\Delta k_{\mathrm{L}} \ll 2k_{\mathrm{L}}$.

As we have seen in Section 3.1.1, the intensity scales with the square of the amplitude of the electric field. Therefore, a position- and time-dependent dipole potential is obtained

$$U_{\mathrm{dip}}(\rho, y, U_0, t) = U_0 \mathrm{e}^{\frac{-2\rho^2}{w(y)^2}} \cos^2\left(k_{\mathrm{L},1} y + \frac{\Delta\omega_{\mathrm{L}}}{2} t\right). \tag{5.8}$$

In comparison to the ODT, the optical conveyor is operated at a much lower detuning. This thus means a lower laser power is needed. This lower laser power is required to not damage the sample when retro-reflecting the laser beam on it. For the optical conveyor a laser with a wavelength of $\lambda = 785\,\mathrm{nm}$ is used.

As derived in Section 3.1.2, the interaction potential for a single focused laser operated at small detunings is given by Equation 3.23. For the optical conveyor with linear polarized light ($\mathcal{P} = 0$), the maximum trap depth U_0 thus results in

$$U_0 = \frac{\pi c^2 \gamma}{2\omega_0^3} \left(\frac{2}{\Delta_2} + \frac{1}{\Delta_1}\right) 4I_0, \tag{5.9}$$

where the factor $4I_0$ comes from the derivation of the electric field given by Equation 5.7. The square of the amplitude of the electric field has been written as $|E_0|^2 = \frac{2}{\epsilon_0 c} I_0$.

Analogously to the interaction potential, the photon scattering rate is obtained. We find

$$\Gamma_{\mathrm{sc}}(\rho, y) = \frac{\pi c^2 \gamma^2}{2\hbar\omega_0^3}\left(\frac{2}{\Delta_2^2} + \frac{1}{\Delta_1^2}\right) 4I_0 \mathrm{e}^{\frac{-2\rho^2}{w(y)^2}} \cos^2\left(k_{\mathrm{L},1} y + \frac{\Delta\omega_{\mathrm{L}}}{2} t\right). \tag{5.10}$$

Up to this point, we have not yet considered displacing the atoms within the optical conveyor. Displacement with high precision can be achieved by displacing the anti-nodes over a distance Δy, effectively "walking" the standing wave. "Walking" of the standing wave is achieved by changing the phase between the two beams. As can be seen from Equation 5.6, a phase difference $\Delta\phi = \frac{\Delta\omega_{\mathrm{L}}}{2} t$ is obtained by using different frequencies for both lasers. The resulting displacement equals

$$\Delta y = \frac{\Delta\omega_{\mathrm{L}} t}{2k_{\mathrm{L},1}}. \tag{5.11}$$

As can be seen from Equation 5.11, the anti-nodes and thus the atoms are displaced over a distance Δy. This is achieved by changing the frequency of one laser with respect to the other. In Section 5.2, the frequency sweeps are derived with which a certain displacement can be achieved.

5.1.1 Trap parameters of a 1D optical lattice

As we have seen in Section 5.1, the intensity distribution of the standing-wave is given by

$$I(\rho, y) = 4I_0 \mathrm{e}^{\frac{-2\rho^2}{w(z)^2}} \cos^2\left(k_{\mathrm{L}} y + \frac{\Delta\omega_{\mathrm{L}}}{2} t\right). \tag{5.12}$$

The trap frequencies are derived by approximating the dipole potential as a harmonic oscillator potential, analogously to Section 3.1.3. The approximation is given by

$$U_{\mathrm{dip}}(\rho, y) \simeq -U_0 \left[1 - 2\left(\frac{\rho}{w_0}\right)^2 - (k_{\mathrm{L}} y)^2\right]. \tag{5.13}$$

By now comparing Equation 5.13 to the energy of a harmonic oscillator, the axial and radial trap frequencies are derived. They result in

$$\Omega_{\mathrm{rad}} = \sqrt{\frac{4U_0}{m w_0^2}}, \tag{5.14}$$

and

$$\Omega_{\mathrm{ax}} = 2\pi\sqrt{\frac{2U_0}{m\lambda^2}}. \tag{5.15}$$

The characteristics of the optical conveyor used in the experiment are listed in Table 5.1.

Property	Symbol	Value
Wavelength	λ	785 nm
Resonance frequency	ω_0	$2\pi \cdot 384$ THz
Laser frequency	ω_L	$2\pi \cdot 382$ THz
Average laser power	P	50 mW
Beam waist in focus	w_0	37.5 µm
Rayleigh range	z_R	5.63 mm
Trap depth	U_0	-3.73 µK
Scattering rate	Γ_sc	9.21 mHz
Radial trap frequency	$\Omega_\mathrm{rad}/2\pi$	160.25 Hz
Axial trap frequency	$\Omega_\mathrm{ax}/2\pi$	34.01 kHz

Table 5.1: Typical optical conveyor characteristics for our experimental conditions.

5.1.2 Hopping time between lattice sites

Atoms in the anti-nodes of a standing wave or the sites of an optical lattice are able to hop between sites with some quantum mechanical hopping (or tunneling) amplitude. During the experiment it is important that the atoms in a lattice site are not able to tunnel to another lattice site in timescales at which the experiment takes place. The time it takes atoms to tunnel from one lattice site into another is calculated using

$$\tau_\mathrm{t} = \frac{h}{t_\mathrm{hop}}, \tag{5.16}$$

where τ_t denotes the tunneling time, h the constant of Planck, and t_hop the hopping parameter. The hopping parameter for an optical lattice has been derived by Van Oosten [32]

$$t_\mathrm{hop} = \frac{\hbar\omega}{8}\left[1 - \left(\frac{2}{\pi}\right)^2\right]\left(\frac{a}{l}\right)^2 e^{-\frac{1}{4}(a/l)^2}, \tag{5.17}$$

where $a = \lambda/2$ denotes the lattice constant, l the width of the potential, and ω the level splitting in the potential. The width and the level splitting in the potential are given by [32]

$$l = \left(-\frac{3\hbar^2}{8mU_0k^2}\right)^{1/4}, \qquad \omega = \sqrt{-\frac{8U_0k^2}{3m}}, \tag{5.18}$$

where U_0 denotes the trap depth in Joule.

With the optical conveyor characteristics in Table 5.1, we obtain $t_\mathrm{hop} = 1.39 \times 10^{-51}$ J. This corresponds to a hoping time of $\tau_\mathrm{t} = 1.51 \times 10^{10}$ yr. Hopping or tunneling of atoms between neighboring sites can thus be neglected.

5.2 Frequency sweep

In this subsection the frequency sweeps, required for the displacement of the atoms in the standing-wave trap are derived. To this end, the subsection is divided in three parts. In Section 5.2.1, we will investigate heating effects due to the displacement of the atoms, trapped in the anti-nodes of the standing-wave. In Sections 5.2.2 and 5.2.3, two frequency sweep functions are constructed using a block signal and cosine signal, respectively.

5.2.1 Heating due to frequency sweep

When introducing a frequency difference $\Delta\omega_{\mathrm{L}}$, the standing wave starts to move along the axis of propagation. The atoms are located at the anti-nodes. Due to the movement, the atoms will gain a velocity and acceleration. Their energy and thus their temperature will increase. As we have seen in Table 5.1 our trap depth equals $-3.73\,\mu\mathrm{K}$. The frequency sweep parameters need to be chosen such that the energy increase is kept well below the trap depth to ensure the atoms do not escape the trap. The energy increase can be determined by locally approximating the anti-nodes of the standing-wave trap by a harmonic oscillator. Newton's formulas for such a system at rest ($\Delta\omega_{\mathrm{L}} = 0$) are given by [39]

$$F = m\ddot{x} = -kx, \tag{5.19}$$

$$m\ddot{x} + kx = 0, \tag{5.20}$$

$$\ddot{x} + \omega_{\mathrm{HO}}^2 x = 0, \tag{5.21}$$

where $-kx$ denotes the restoring force, and $\omega_{\mathrm{HO}} = \sqrt{k/m}$ the trap frequency of the harmonic oscillator where k denotes the spring constant, and m the mass of the oscillating object. By solving the differential equation given in Equation 5.21 for $x(t)$, the energy of the harmonic oscillator can be obtained. The solution equals

$$x(t) = C_1 \cos(\omega_{\mathrm{HO}} t) + C_2 \sin(\omega_{\mathrm{HO}} t), \tag{5.22}$$

$$= \sqrt{C_1^2 + C_2^2}\cos(\omega_{\mathrm{HO}} t + \arctan(C_2/C_1)), \tag{5.23}$$

$$\equiv B\cos(\omega_{\mathrm{HO}} t + \phi), \tag{5.24}$$

$$v(t) = -\omega_{\mathrm{HO}} B \sin(\omega_{\mathrm{HO}} t + \phi), \tag{5.25}$$

where $B = \sqrt{C_1^2 + C_2^2}$ denotes the amplitude or maximum displacement from the equilibrium position, and $\phi = \arctan(C_2/C_1)$ the phase of the cosine wave. The total energy of the harmonic oscillator can be obtained, using Equations 5.24 and 5.25

$$E_{\mathrm{tot}} = \frac{1}{2}mv^2 + \frac{1}{2}kx^2 \tag{5.26}$$

$$= \frac{1}{2}m\omega_{\mathrm{HO}}^2 B^2 \tag{5.27}$$

5.2.1.1 Heating due to acceleration

In the non-inertial frame of reference, e.g. the reference frame of the atoms, the atoms are subjected to a fictitious force when displacing the standing wave or harmonic oscillator. This fictitious force is in the opposite direction of motion of the standing wave. The force increases the energy of the atoms by ΔE with respect to Equation 5.27. In the reference frame of the atoms, the system is described by

$$F = m\ddot{x} = -kx - ma_{\mathrm{a}}, \tag{5.28}$$

$$\ddot{x} + \omega_{\mathrm{HO}}^2 x + a_{\mathrm{a}} = 0, \tag{5.29}$$

$$\ddot{x} + \omega_{\mathrm{HO}}^2 \left(x + \frac{a_{\mathrm{a}}}{\omega_{\mathrm{HO}}^2} \right) = 0, \tag{5.30}$$

$$\ddot{x}_{\mathrm{eff}} + \omega_{\mathrm{HO}}^2 x_{\mathrm{eff}} = 0, \tag{5.31}$$

where $\ddot{x}$ denotes the acceleration of the harmonic oscillator, a_{a} the "external" acceleration of the atoms, and $x_{\mathrm{eff}} = x + \frac{a_{\mathrm{a}}}{\omega_{\mathrm{HO}}^2}$. An expression for $x(t)$ is obtained by solving the differential equation, given by Equation 5.31, for $x_{\mathrm{eff}}(t)$. We obtain

$$x_{\mathrm{eff}}(t) = C_1 \cos(\omega_{\mathrm{HO}} t) + C_2 \sin(\omega_{\mathrm{HO}} t), \tag{5.32}$$

$$x(t) = C_1 \cos(\omega_{\mathrm{HO}} t) + C_2 \sin(\omega_{\mathrm{HO}} t) - \frac{a_{\mathrm{a}}}{\omega_{\mathrm{HO}}^2}, \tag{5.33}$$

$$= \sqrt{C_1^2 + C_2^2} \cos(\omega_{\mathrm{HO}} t + \arctan(C_2/C_1)) - \frac{a_{\mathrm{a}}}{\omega_{\mathrm{HO}}^2}, \tag{5.34}$$

$$\equiv B \cos(\omega_{\mathrm{HO}} t + \phi) - \frac{a_{\mathrm{a}}}{\omega_{\mathrm{HO}}^2}, \tag{5.35}$$

$$v(t) = -\omega_{\mathrm{HO}} B \sin(\omega_{\mathrm{HO}} t + \phi). \tag{5.36}$$

From the comparison between Equations 5.24 and 5.35 and between Equations 5.25 and 5.36, we observe an increase in energy associated with the acceleration. This increase ΔE_a is caused by the displacement of the standing wave. An expression for the total energy of the harmonic oscillator is obtained using the expressions from Equations 5.35 and 5.36 in Equation 5.26. By comparing the total energy of the harmonic oscillator with the total energy for a system at rest, we observe that the energy increase is to the potential energy. It is given by

$$\Delta E_a = -m a_{\mathrm{a}}^2 B \cos(\omega_{\mathrm{HO}} t + \phi) + \frac{1}{2} m \left(\frac{a_{\mathrm{a}}}{\omega_{\mathrm{HO}}} \right)^2. \tag{5.37}$$

Since the time average of a cosine function over a single period equals zero, Equation 5.37 reduces to

$$\Delta E_a = \frac{1}{2} m \left(\frac{a_{\mathrm{a}}}{\omega_{\mathrm{HO}}} \right)^2. \tag{5.38}$$

We assume the redistribution of ΔE_a over the individual atoms is due to collisions. These occur frequently because of the displacement of the standing wave. The temperature increase ΔT_a associated with the acceleration can thus be written as

$$\Delta T_a = \frac{\Delta E_a}{k_\mathrm{B}}. \tag{5.39}$$

With the formula for temperature increase now known, increases in temperature are calculated for different accelerations of the atoms in the standing wave. As mentioned earlier, ω_HO in Equation 5.38 denotes the trap frequency for the harmonic oscillator approximation. For the energy increase of the atoms in the optical conveyor, the trap frequency is given by $\omega_\mathrm{HO} = \Omega_\mathrm{ax} = 2\pi \cdot 34.01\,\mathrm{kHz}$. With a mass of $\sim$87 u and accelerations of g and $10g$, where $g = 9.81\,\mathrm{m/s^2}$ denotes the acceleration due to gravity, the atoms are heated by 11.01 pK and 1.10 nK, respectively. The atoms are heated very little compared to the trap depth.

5.2.1.2 Heating due to jerk

Besides the acceleration it is also possible to see whether the jerk, which is the time derivative of the acceleration, causes an increase in energy. This is done with the same equation of motion as given by Equation 5.28. The acceleration of the atoms a_a is now written as $j_\mathrm{a}\,t$. From the resulting differential equation, a solution for $v(t)$ is obtained which can be used to determine the energy of the system. In the reference frame of the atoms the system can now be described by

$$F = m\ddot{x} = -kx - ma_\mathrm{a}, \tag{5.40}$$
$$m\ddot{x} = -kx - mj_\mathrm{a}t, \tag{5.41}$$
$$\ddot{x} + \omega_\mathrm{HO}^2 x = -j_\mathrm{a}t, \tag{5.42}$$
$$\dddot{x} + \omega_\mathrm{HO}^2 \dot{x} = -j_\mathrm{a}, \tag{5.43}$$
$$\ddot{v} + \omega_\mathrm{HO}^2 v = -j_\mathrm{a}, \tag{5.44}$$
$$\ddot{v} + \omega_\mathrm{HO}^2 \left(v + \frac{j_\mathrm{a}}{\omega_\mathrm{HO}^2} \right) = 0, \tag{5.45}$$
$$\ddot{v}_\mathrm{eff} + \omega_\mathrm{HO}^2 v_\mathrm{eff} = 0, \tag{5.46}$$

where $\ddot{v}$ denotes the jerk of the harmonic oscillator, j_a the "external" jerk of the atoms, and $v_\mathrm{eff} = (v + \frac{j_\mathrm{a}}{\omega_\mathrm{HO}^2})$. By solving the differential equation in Equation 5.46

for $v_{\text{eff}}(t)$, an expression for $v(t)$ can be obtained. We find

$$v_{\text{eff}}(t) = C_3 \cos(\omega_{\text{HO}} t) + C_4 \sin(\omega_{\text{HO}} t), \tag{5.47}$$

$$v(t) = C_3 \cos(\omega_{\text{HO}} t) + C_4 \sin(\omega_{\text{HO}} t) - \frac{j_{\text{a}}}{\omega_{\text{HO}}^2}, \tag{5.48}$$

$$= \sqrt{C_3^2 + C_4^2} \cos(\omega_{\text{HO}} t + \arctan(C_4/C_3)) - \frac{j_{\text{a}}}{\omega_{\text{HO}}^2}, \tag{5.49}$$

$$\equiv D \cos(\omega_{\text{HO}} t + \phi) - \frac{j_{\text{a}}}{\omega_{\text{HO}}^2}, \tag{5.50}$$

$$x(t) = -\omega_{\text{HO}} D \sin(\omega_{\text{HO}} t + \phi) - \frac{a_{\text{a}}}{\omega_0^2}, \tag{5.51}$$

where $D = \sqrt{C_3^2 + C_4^2}$ denotes the amplitude or maximum displacement from the equilibrium position, and $\varphi = \arctan(C_4/C_3)$ the phase of the cosine wave. Compared to Equations 5.35 and 5.36, we obtain an additional increase in energy ΔE_j to the kinetic energy of the system. It is given by

$$\Delta E_j = \frac{1}{2} m \left(\frac{j_{\text{a}}}{\omega_{\text{HO}}^2} \right)^2. \tag{5.52}$$

With the formula for the energy increase due to the jerk now known, temperature increases are calculated for different jerks of the atoms in the standing wave. This is done by assuming the redistribution of energy is still due to collisions. With jerks of $1\,\text{m/s}^3$ and $10^6\,\text{m/s}^3$, the atoms are heated by $2.51 \times 10^{-12}\,\text{pK}$ and $2.51\,\text{nK}$, respectively. The temperature increases are again extremely small compared to the trap depth.

The energy increase due to both the acceleration and jerk is given by

$$\Delta E = \frac{1}{2} m \left(\frac{a_{\text{a}}}{\omega_{\text{HO}}} \right)^2 + \frac{1}{2} m \left(\frac{j_{\text{a}}}{\omega_{\text{HO}}^2} \right)^2. \tag{5.53}$$

5.2.2 Block signal

As can be seen from Equation 5.53, the energy increase depends on both the acceleration and jerk. To this end, the frequency sweep is constructed considering both a maximum acceleration a_{max} and a maximum jerk j_{max}. These values denote the acceleration and jerk for which the temperature increase becomes too large. In the algorithm used generate the frequency sweep, both values can be set at any desired value. In order to have as fast a frequency sweep as possible, the absolute value of the jerk is maximum at all times. This will result in a linear change in the acceleration. The frequency sweep is therefore constructed using a block function. For the block function it is necessary to define time intervals as it consists of multiple splines.

This subsection is divided into two parts. In Section 5.2.2.1, we derive a frequency sweep for which the acceleration we reach with the sweep, a_{reached}, is below or equal to $a_{\max}$. In this case the temperature increase is accepted. In Section 5.2.2.2, we construct a frequency sweep for which we consider a_{reached} to be larger than $a_{\max}$. In this case the temperature increase would be too large. Adjustments to the frequency sweep are made by keeping the acceleration constant as soon as a_{reached} would exceed $a_{\max}$. The acceleration is kept constant for a time $\Delta\tau$.

This part is based on the work by Visser [40].

5.2.2.1 Frequency sweep without acceleration limit

Since we do not exceed $a_{\max}$, no adjustments are needed. The intervals required to construct the frequency sweep are thus equal in duration. For this simple case, a total of three time intervals are required. The jerk $j(t)$ is given by

$$j(t) = \begin{cases} j_{\max} & \text{if } 0 \leq t \leq \tau/4, \\ -j_{\max} & \text{if } \tau/4 \leq t \leq \frac{3}{4}\tau, \\ j_{\max} & \text{if } \frac{3}{4}\tau \leq t \leq \tau, \end{cases} \tag{5.54}$$

where τ denotes the total time of the sweep.

By integrating the splines in Equation 5.54 over their respected time intervals, the acceleration $a(t)$ is obtained. We obtain

$$a(t) = \begin{cases} j_{\max} t & \text{if } 0 \leq t \leq \tau/4, \\ -\frac{1}{2} j_{\max}(2t - \tau) & \text{if } \tau/4 \leq t \leq \frac{3}{4}\tau, \\ j_{\max}(t - \tau) & \text{if } \frac{3}{4}\tau \leq t \leq \tau, \end{cases} \tag{5.55}$$

The splines for $v(t)$ are obtained by integrating the splines in Equation 5.55 over their respected time intervals. Hence,

$$v(t) = \begin{cases} \frac{1}{2} j_{\max} t^2 & \text{if } 0 \leq t \leq \tau/4, \\ -\frac{1}{16} j_{\max}(8t^2 - 8\tau t + \tau^2) & \text{if } \tau/4 \leq t \leq \frac{3}{4}\tau, \\ \frac{1}{2} j_{\max}(t - \tau)^2 & \text{if } \frac{3}{4}\tau \leq t \leq \tau, \end{cases} \tag{5.56}$$

where the frequency sweep is obtained via $\Delta\omega_{\text{L}}(t) = \frac{2\pi v(t)}{\lambda}$.

Finally, the splines for $x(t)$ are obtained by integrating the splines in Equation 5.56. This results in

$$x(t) = \begin{cases} \frac{1}{6} j_{\max} t^3 & \text{if } 0 \leq t \leq \tau/4, \\ -\frac{1}{192} j_{\max}(32t^3 - 48\tau t^2 + 12\tau^2 t - \tau^3) & \text{if } \tau/4 \leq t \leq \frac{3}{4}\tau, \\ \frac{1}{96} j_{\max}(16t^3 - 48\tau t^2 + 48\tau^2 t - 13\tau^3) & \text{if } \frac{3}{4}\tau \leq t \leq \tau. \end{cases} \tag{5.57}$$

In Figure 5.1, the jerk, acceleration, velocity and displacement are plotted as a function of time.

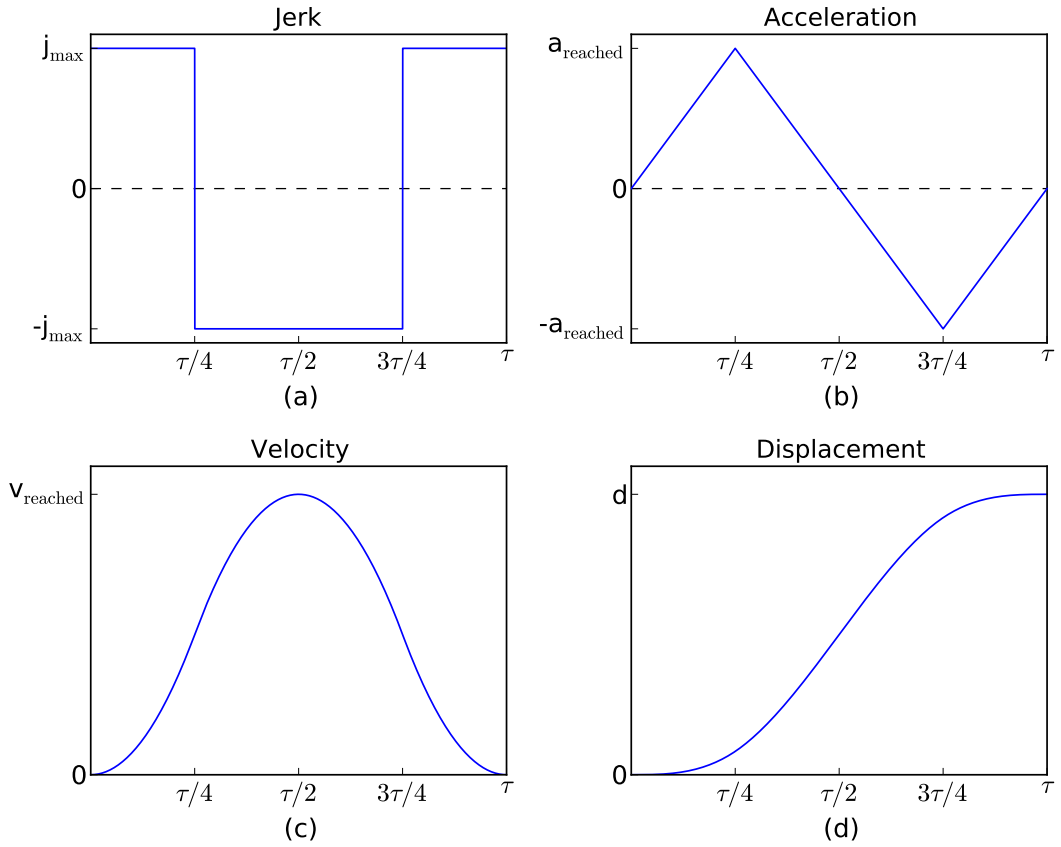

Figure 5.1: The sweep function using a block signal for the case the maximum acceleration is not exceeded: (a) The jerk as a function of time; (b) the acceleration as a function of time; (c) the velocity as a function of time; (d) the position as a function of time.

The parameters to generate the sweep are $j_{\max}$ and d. The distance travelled by the atoms after a time τ is defined by d. Note that by solving $x(\tau) = d$, an expression for τ can be obtained

$$\tau = \left(\frac{32d}{j_{\max}}\right)^{1/3}. \tag{5.58}$$

The discretization of the frequency sweep is determined by the time intervals between each frequency. The intervals are generated using a direct digital synthesizer (DDS). The length of each time interval is denoted by the number of idlers N_{idlers}. Both the DDS and the number of idlers are discussed by Visser [40].

By definition, the acceleration is maximal for $\tau/4$. Hence, $a(\tau/4) = a_{\text{reached}}$. This can also be seen in Figure 5.1. The expression for a_{reached} depends on the jerk and

the displacement of the atoms. It is given by

$$a_{\text{reached}} = \left(\frac{dj_{\max}^2}{2}\right)^{1/3}. \tag{5.59}$$

Note from Equation 5.59 that by choosing d and $j_{\max}$ carefully, the temperature increase can be controlled. When the temperature increase is too large, adjustments need to be made.

5.2.2.2 Frequency sweep with acceleration limit

When the temperature increase is too large, the maximum value for the acceleration is exceeded. In this case, the temperature increase is limited by keeping the acceleration constant for a time $\Delta\tau$. This is done as soon as the acceleration reaches $a_{\max}$. The expression for $\Delta\tau$ is given by Equation 5.71. It is determined such that the displacement of the frequency sweep is the same as when $a_{\max}$ would not exceeded.

Note that for this frequency sweep, two additional time intervals are required. The intervals are defined by

$$\tau_1 = \frac{a_{\max}}{j_{\max}}, \tag{5.60}$$
$$\tau_2 = \tau_1 + \Delta\tau, \tag{5.61}$$
$$\tau_3 = 3\tau_1 + \Delta\tau, \tag{5.62}$$
$$\tau_4 = 3\tau_1 + 2\Delta\tau, \tag{5.63}$$
$$\tau_{\text{c}} = 4\tau_1 + 2\Delta\tau, \tag{5.64}$$

where τ_{c} denotes the total time of the sweep. The subscript c indicates the change in total sweep time with respect to the frequency sweep where $a_{\max}$ is not exceeded.

To obtain a frequency sweep as fast as possible, the absolute value of the jerk is again maximal. At least, this will be case in the odd time intervals. In the even time intervals the acceleration is kept constant. The jerk thus equals zero

$$j(t) = \begin{cases} j_{\max} & \text{if } 0 \le t \le \tau_1, \\ 0 & \text{if } \tau_1 \le t \le \tau_2, \\ -j_{\max} & \text{if } \tau_2 \le t \le \tau_3, \\ 0 & \text{if } \tau_3 \le t \le \tau_4, \\ j_{\max} & \text{if } \tau_4 \le t \le \tau_{\text{c}}. \end{cases} \tag{5.65}$$

The acceleration results in

$$a(t) = \begin{cases} j_{\max} t & \text{if } 0 \le t \le \tau_1, \\ j_{\max} \tau_1 & \text{if } \tau_1 \le t \le \tau_2, \\ -j_{\max}(t - 2\tau_1 - \Delta\tau) & \text{if } \tau_2 \le t \le \tau_3, \\ -j_{\max} \tau_1 & \text{if } \tau_3 \le t \le \tau_4, \\ j_{\max}(t - 4\tau_1 - 2\Delta\tau) & \text{if } \tau_4 \le t \le \tau_c, \end{cases} \tag{5.66}$$

the velocity in

$$v(t) = \begin{cases} \frac{1}{2} j_{\max} t^2 & \text{if } 0 \le t \le \tau_1 \\ \frac{1}{2} j_{\max} \tau_1 (2t - \tau_1) & \text{if } \tau_1 \le t \le \tau_2 \\ -\frac{1}{2} j_{\max}(t^2 - 2t(2\tau_1 + \Delta\tau) + 2\tau_1^2 + \Delta\tau^2 + 2\tau_1\Delta\tau) & \text{if } \tau_2 \le t \le \tau_3 \\ -\frac{1}{2} j_{\max} \tau_1 (2t - 7\tau_1 - 4\Delta\tau) & \text{if } \tau_3 \le t \le \tau_4 \\ \frac{1}{2} j_{\max}(t - 4\tau_1 - 2\Delta\tau)^2 & \text{if } \tau_4 \le t \le \tau_c \end{cases} \tag{5.67}$$

and finally, the displacement in

$$x(t) = \begin{cases} \frac{1}{6} j_{\max} t^3 & \text{if } 0 \le t \le \tau_1 \\ \frac{1}{6} j_{\max} \tau_1 (3t^2 - 3\tau_1 t + \tau_1^2) & \text{if } \tau_1 \le t \le \tau_2 \\ -\frac{1}{6} j_{\max}(t^3 - 3t^2(2\tau_1 + \Delta\tau) + 3t(2\tau_1^2 + \Delta\tau^2 & \text{if } \tau_2 \le t \le \tau_3 \\ \quad +2\tau_1\Delta\tau) - (\tau_1 + \Delta\tau)^3 - \tau_1^3) & \\ -\frac{1}{6} j_{\max} \tau_1 (3t^2 - 3t(7\tau_1 + 4\Delta\tau) + 25\tau_1^2 & \text{if } \tau_3 \le t \le \tau_4 \\ \quad +6\Delta\tau^2 + 24\tau_1\Delta\tau) & \\ \frac{1}{6} j_{\max}(t^3 - 6t^2(2\tau_1 + \Delta\tau) + 6t(8\tau_1^2 + 2\Delta\tau^2 & \text{if } \tau_4 \le t \le \tau_c \\ \quad +8\tau_1\Delta\tau) - 52\tau_1^3 - 8\Delta\tau^3 & \\ \quad -78\tau_1^2\Delta\tau - 42\Delta\tau^2\tau_1) & \end{cases} \tag{5.68}$$

In Figure 5.2, the jerk, acceleration, velocity and displacement are plotted as a function of time.

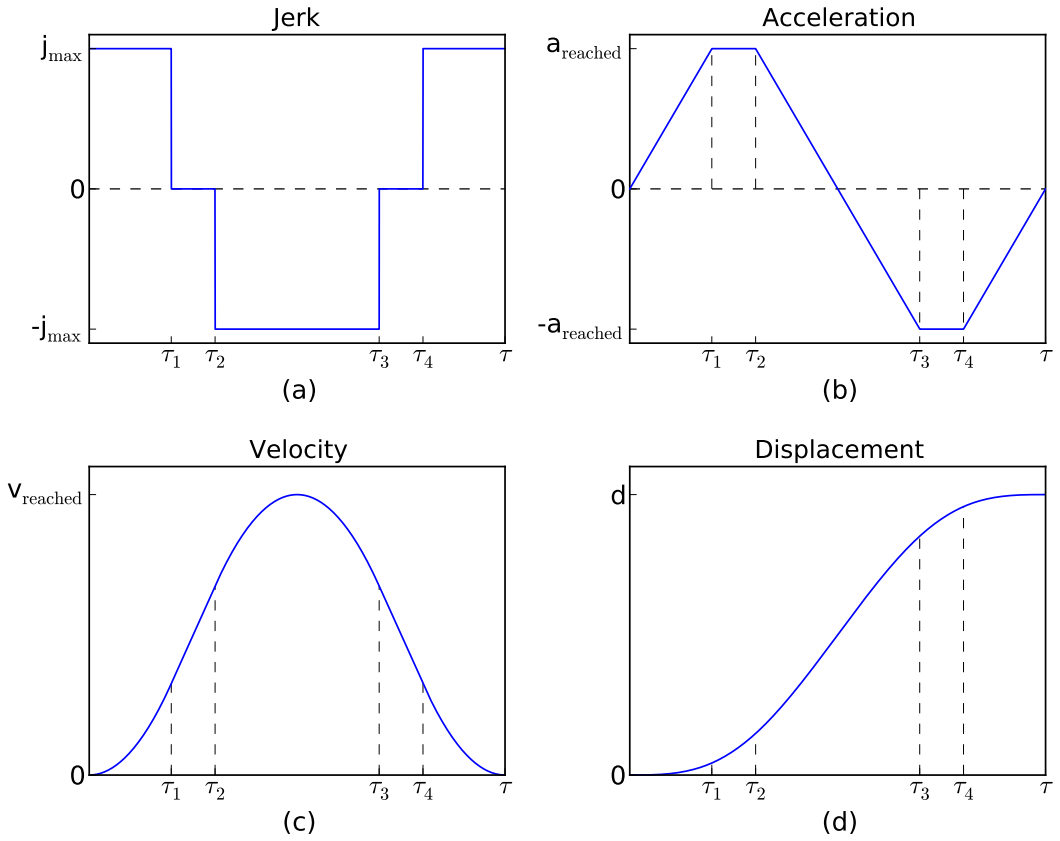

Figure 5.2: The sweep function using a block signal for the case the maximum acceleration would be exceeded: (a) The jerk as a function of time; (b) the acceleration as a function of time; (c) the velocity as a function of time; (d) the position as a function of time.

With all the splines determined, an expression for $\Delta\tau$ can be obtained. The condition for $\Delta\tau$ is that the displacement is equal for both frequency sweeps. The displacement for the sweep where $a_{\max}$ is not exceeded is obtained by rewriting Equation 5.58. We obtain

$$d = \frac{1}{32} j_{\max} \tau^3. \tag{5.69}$$

The displacement when $a_{\max}$ would be exceeded is obtained by integrating each spline of $v(t)$ in Equation 5.67 over their respected time interval. This results in

$$d = j_{\max}\tau_1(\tau_1 + \Delta\tau)(2\tau_1 + \Delta\tau). \tag{5.70}$$

The expression for $\Delta\tau$ is thus given by

$$\Delta\tau = -\frac{3}{2}\frac{a_{\max}}{j_{\max}} + \frac{1}{2}\frac{a_{\max}}{j_{\max}}\sqrt{1 + \frac{4dj_{\max}^2}{a_{\max}^3}}. \tag{5.71}$$

With the formula now known for $\Delta\tau$ we are able to construct the frequency sweep such that the displacement is equal for both cases.

5.2.3 Cosine signal

In order to have as fast a frequency sweep as possible, the sweep is constructed using a block signal. However, to test the optical conveyor the measured displacement needs to be compared to the theoretical displacement. As can be seen from Equations 5.57 and 5.68, the displacement functions consists of multiple splines making the comparison tedious. To this end, the optical conveyor is tested using a frequency sweep that was constructed with a cosine signal. For a cosine signal, the displacement is a continuous function. Note that this holds when $a_{\max}$ would not be exceeded.

5.2.3.1 Frequency sweep without acceleration limit

For this frequency sweep the jerk is described by a cosine. Note that in order to sweep as fast as possible, the amplitude of the cosine equals $j_{\max}$. The jerk can thus be described by

$$j(t) = j_{\max} \cos\left(\frac{2\pi}{\tau} t\right) \quad \text{if } 0 \leq t \leq \tau, \tag{5.72}$$

where $2\pi/\tau$ denotes the period of the cosine, and τ the total time of the sweep.

With the expression for the jerk, the acceleration is given by

$$a(t) = \frac{j_{\max}}{2\pi} \tau \sin\left(\frac{2\pi}{\tau} t\right) \quad \text{if } 0 \leq t \leq \tau, \tag{5.73}$$

the velocity by

$$v(t) = \frac{j_{\max}}{4\pi^2} \tau^2 \left[1 - \cos\left(\frac{2\pi}{\tau} t\right)\right] \quad \text{if } 0 \leq t \leq \tau, \tag{5.74}$$

and the displacement by

$$x(t) = \frac{j_{\max}}{8\pi^2} \tau^2 \left[2t - \frac{\tau}{\pi} \sin\left(\frac{2\pi}{\tau} t\right)\right] \quad \text{if } 0 \leq t \leq \tau. \tag{5.75}$$

The jerk, acceleration, velocity and displacement are plotted as a function of time in Figure 5.3.

For this frequency sweep, the total sweep time is given by

$$\tau = \left(\frac{4\pi^2 d}{j_{\max}}\right)^{1/3}. \tag{5.76}$$

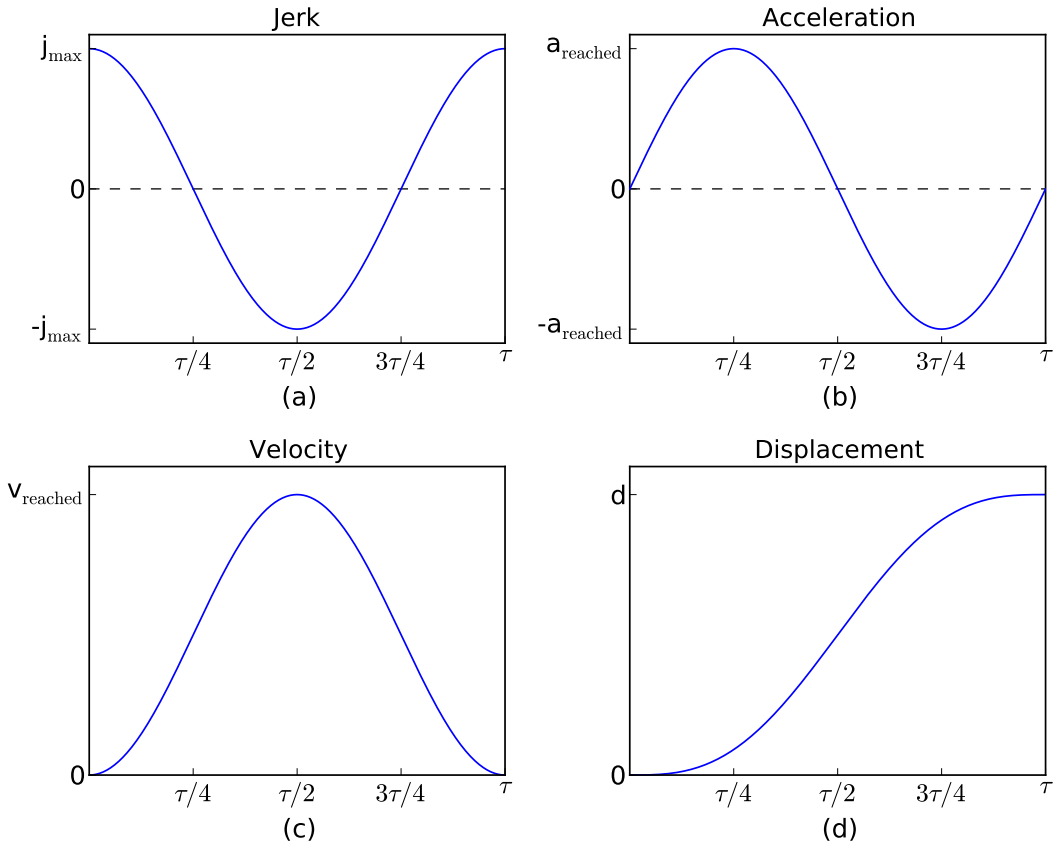

Figure 5.3: The sweep function using a cosine signal without exceeding the maximum acceleration: (a) The jerk as a function of time; (b) the acceleration as a function of time; (c) the velocity as a function of time; (d) the displacement as a function of time.

By definition, the acceleration is maximal for $\tau/4$. Hence, $a(\tau/4) = a_{\text{reached}}$. This can also be seen in Figure 5.3. The expression for a_{reached} depends on the jerk and the displacement of the atoms. It is given by

$$a_{\text{reached}} = \left(\frac{d j_{\text{max}}^2}{2\pi}\right)^{1/3}. \tag{5.77}$$

5.3 Experimental setups

In this subsection, two different experimental setups are discussed. These were used to test the optical conveyor. In Section 5.3.1, the electronic setup used to test the direct digital synthesizer (DDS) is discussed. In Section 5.3.2, a prototype of the optical conveyor is discussed. This prototype is used to test the displacement using laser beams. The results obtained using these experimental setups are discussed in

Section 6.

5.3.1 Electronic setup

The function of the electronic setup was to test the DDS. The DDS is discussed extensively by Visser [40]. As indicated in Figure 5.4, two channels of the DDS are used. One channel generates a 80 MHz signal. The second channel generates the same signal with an additional frequency sweep $\Delta\omega_{\mathrm{L}}(t)$. Both signals are mixed by a frequency mixer, which as output gives the difference. The output of the mixer is sent to the data acquisition (DAQ). From the measured difference frequency the displacement can be determined. This is discussed in more detail in Section 6.1.

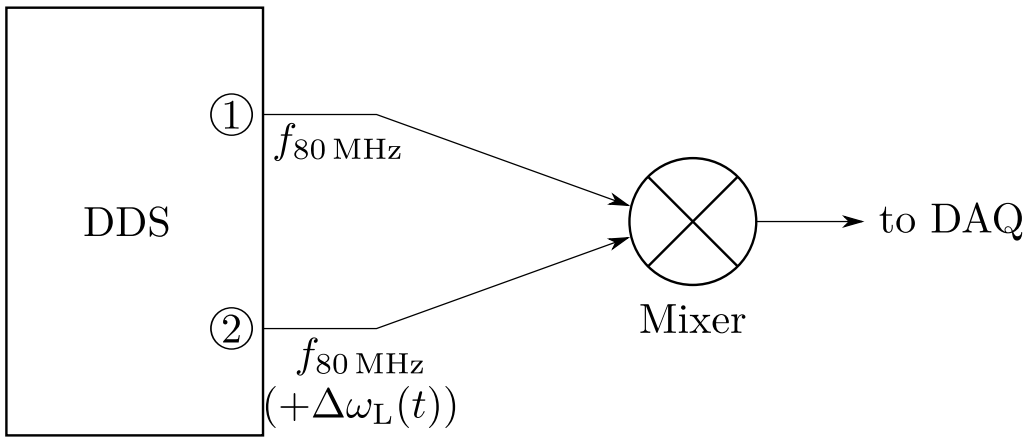

Figure 5.4: Schematic overview of the electronic setup. Two frequency signals, generated by the DDS are mixed and measured. A displacement is introduced by adding a frequency difference to channel 2 with respect to channel 1 which generates a 80 MHz signal.

The experimental setup was tested with signals of 80 MHz. This is because the AOMs that will be used for the optical conveyor setup are the ATM-801A2 from IntraAction. The center frequency of these AOMs is 80 MHz.

5.3.2 Optical conveyor prototype

After the successful test of the electronic setup, a prototype of the optical conveyor was build. An overview of the setup is given in Figure 5.5. In this setup, a beam is introduced by the out-coupler. After the out-coupler it is split into two beams using a 50/50 beam splitter cube. The transmitted beam is considered the counter-clockwise (ccw) propagating beam, while the reflected beam is referred to as the clockwise (cw)

propagating beam. Both the clockwise and counter-clockwise propagating beams pass through their respective AOMs, indicated by $\mathrm{AOM_{cw}}$ and $\mathrm{AOM_{ccw}}$, respectively.

The clockwise propagating beam is directed towards the third AOM in the setup denoted by $\mathrm{AOM_{pilot}}$. From $\mathrm{AOM_{pilot}}$ the zeroth- and both the positive- and negative first orders are obtained for both the clockwise and the counter-clockwise propagating beams. For the clockwise propagating beam, the positive order of $\mathrm{AOM_{pilot}}$ is used, while the negative first order is used for the counter-clockwise propagating beam. The counter-clockwise propagating beam is retro-reflected towards $\mathrm{AOM_{pilot}}$. Both the clockwise and retro-reflected counter-clockwise propagating beam are overlapped in the positive first order of $\mathrm{AOM_{pilot}}$. The beat note of the overlapped beams is measured using a fast photodiode (PD). From this beat note the difference frequency is obtained.

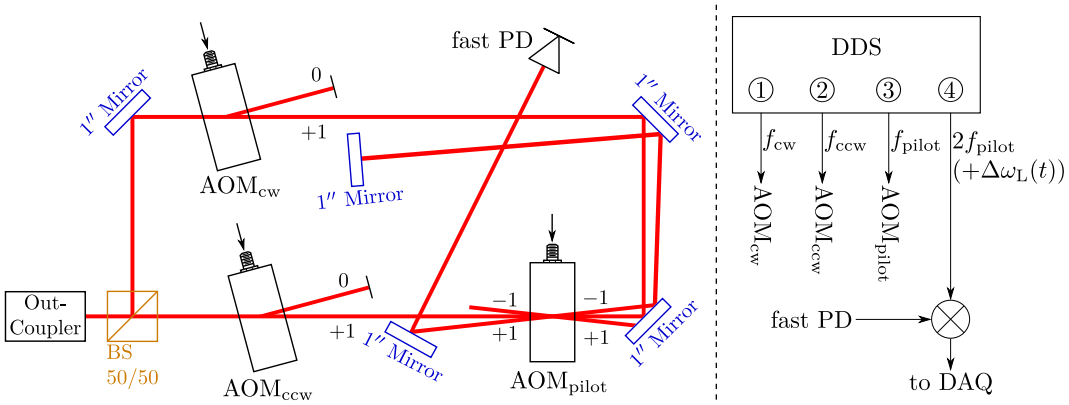

Figure 5.5: Schematic overview of the optical conveyor prototype. The laser beam is denoted in red, the beam splitter cube in brown, and the mirrors by blue. With $\mathrm{AOM_{pilot}}$ two beams are overlapped of which one beam contains a frequency sweep $\Delta\omega_\mathrm{L}(t)$. The resulting beat note is measured by a fast photodiode.

As can be seen from Figure 5.5, $\mathrm{AOM_{ccw}}$ and $\mathrm{AOM_{cw}}$ are operated by two channels of the DDS. The driving frequencies are $f_\mathrm{ccw} = 80\,\mathrm{MHz}$ and $f_\mathrm{cw} = 80\,\mathrm{MHz} + \Delta\omega_\mathrm{L}(t)$, respectively. $\mathrm{AOM_{pilot}}$ is driven using a third channel of the DDS with $f = 85\,\mathrm{MHz}$. Due to mechanical vibrations in the setup, a phase difference between the beams is introduced. This phase difference can be obtained using another channel of the DDS. This channel is used to generate the frequency that is expected without the extra phase. Since, both the counter-clockwise and the clockwise propagating beams pass through $\mathrm{AOM_{pilot}}$, the frequency of the fourth channel is $2f_\mathrm{pilot} + \Delta\omega_\mathrm{L}(t)$. By mixing this frequency with the signal measured by the fast photodiode, the phase difference can be obtained. This phase difference can be minimized using an error feedback mechanism.

6 Optical Conveyor: Test Results

In this section, the results of both experimental setups are discussed. It is divided into three parts. In Section 6.1, we discuss how the displacement of the anti-nodes is obtained from the experimental data. In Sections 6.2 and 6.3 the results of the electronic setup and the optical conveyor prototype are discussed, respectively.

6.1 Analysis

Data from the electronic setup and the prototype of the optical conveyor is acquired via a National Instruments USB-6211 data acquisition module (DAQ). This module has a sampling rate of 250 kS/s. In Figure 6.1(a), a typical signal recorded by the DAQ module is plotted. The increase and decrease of the frequency is clearly visible at the beginning of the sweep ($t = 0.1$) and at the end of the sweep ($t = 0.9$), respectively. In Figure 6.1(b), a spectrogram of the measured signal is plotted. This is a visual representation of the frequency spectrum. In the figure, the frequency sweep and its harmonics are visible.

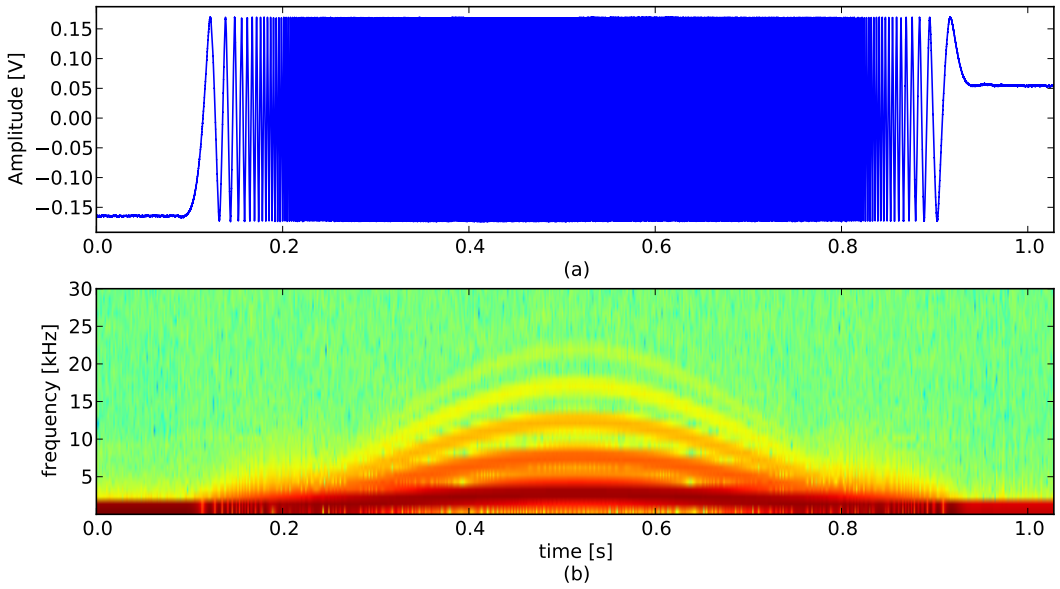

Figure 6.1: (a) Signal acquired by the National Instruments USB-6211 data acquisition module with a sampling rate of $250\,\mathrm{kS\,s^{-1}}$. (b) Spectrogram of the measured signal. The frequency sweep and its harmonics are visible.

To determine the displacement from the signal in Figure 6.1(a), the zero-crossings are determined. By definition, the intensity maxima will move one wavelength for every two zero-crossings of the measured signal. Thus, for ever zero-crossing the atoms are

displaced by $\lambda/2$.

A zero-crossing occurs when the amplitude flips sign. Four points in total, two before and two after each sign flip, are fitted to a linear function $y = at + b$. The points in time where a zero-crossings occurs t_0 are then determined via $t_0 = -b/a$. Although the signal acquired with the DAQ module is proportional to $\cos(\phi(t))$, the linear approximation around the zero-crossings is justified. This is because the time steps are in the order 1 µs compared to the period of the cosine wave which is in the order of 1 ms. In Figure 6.2, six zero-crossings are plotted in red.

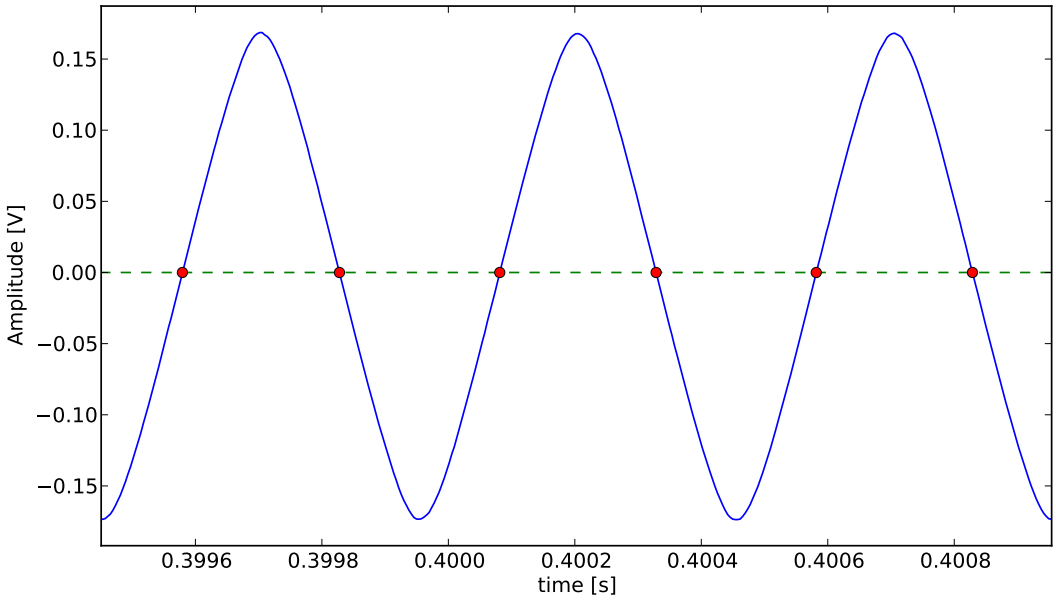

Figure 6.2: Part of the signal obtained with the National Instruments USB-6211 data acquisition module. The zero line is depicted by the dashed green line, and the obtained zero-crossings by red dots.

To determine the accuracy of the displacement of an anti-node, the theoretical displacement derived in Section 5.2.3.1 is fitted to the experimental displacement. For the theoretical fit we introduce two parameters. An offset in time t_{off} is introduced to account for the fact that we do not exactly know when the frequency sweep starts. The other parameter is a displacement offset d_{off}. This offset is introduced because the measured signal might not start and end exactly at a zero-crossing. This in turn would mean that we do not take the full displacement of the anti-node into account. This would thus introduce a mismatch between the experimental and theoretical displacement. The theoretical fit is given by

$$d(t) = \frac{j_{\max}\tau^2}{8\pi^2}\left[2\left(t - t_{\text{off}}\right) - \frac{\tau}{\pi}\sin\left(\frac{2\pi}{\tau}\left[t - t_{\text{off}}\right]\right)\right] + d_{\text{off}}. \tag{6.1}$$

In Figures 6.3 and 6.4 a fit is made to the experimental displacement using Equation 6.1.

6.2 Electronic setup

In the electronic setup, two signals were generated by the DDS. As indicated in Figure 5.4, one channel was set at 80 MHz while the other channel was set at 80 MHz+ $\Delta\omega_{\mathrm{L}}(t)$, where $\Delta\omega_{\mathrm{L}}(t)$ denotes the frequency sweep. Both signals were mixed using a frequency mixer to obtain the difference frequency. The frequency sweep used in the electronic setup was generated using a cosine signal without exceeding $a_{\max}$. Hence, the experimental displacement can be fitted using Equation 6.1. The parameters with which the sweep was generated are listed in Table 6.1.

Property	Symbol	Value
Displacement	d	$800\,\mu\mathrm{m}$
Maximum jerk	$j_{\max}$	$0.05\,\mathrm{m/s^3}$
Maximum acceleration	$a_{\max}$	$0.02\,\mathrm{m/s^2}$
Number of idlers[1]	N_{idlers}	62

Table 6.1: Frequency sweep parameters for the electronic setup measurement.

The generated frequency sweep has a maximal frequency of $\Delta\omega_{\mathrm{L,max}} = 2\pi \cdot 2.41\,\mathrm{kHz}$ and a maximum acceleration of $a_{\mathrm{reached}} = 6.92 \times 10^{-3}\,\mathrm{m/s^2}$. The maximal frequency corresponds to a maximal velocity of $v_{\max} = 1.87\,\mathrm{mm/s}$. The sweep would cause the atoms to heat by $\Delta T = 6.17 \times 10^{-3}\,\mathrm{pK}$.

As discussed in Section 6.1, the displacement of the atoms in the anti-node is determined with the zero-crossings of the measured signal. The displacement obtained with the electronic setup is plotted in Figure 6.3, where each red dot indicates a zero-crossing, the black dashed line the theoretical fit, and in blue the residual. The residual indicates the fitting error which can be obtained by subtracting the theoretical fit from the experimental displacement.

As can be seen from Figure 6.3, the residual is in the order 1 nm, indicating a good agreement between the experimental displacement and the theoretical fit. As can be seen from the acquired signal, indicated by Figure 6.1(a), the number of zero-crossings, and thus the displacement, has a broader spread at the beginning and end of the sweep. Therefore, one could expect the residual to be larger at the beginning and end of the theoretical fit due to less data points. As observed in Figure 6.3, this is not the case. The residual is therefore most likely due to the electronic noise of the DDS or the DAQ module.

[1] The concept of the number of idlers is explained in Section 5.2.2.1.

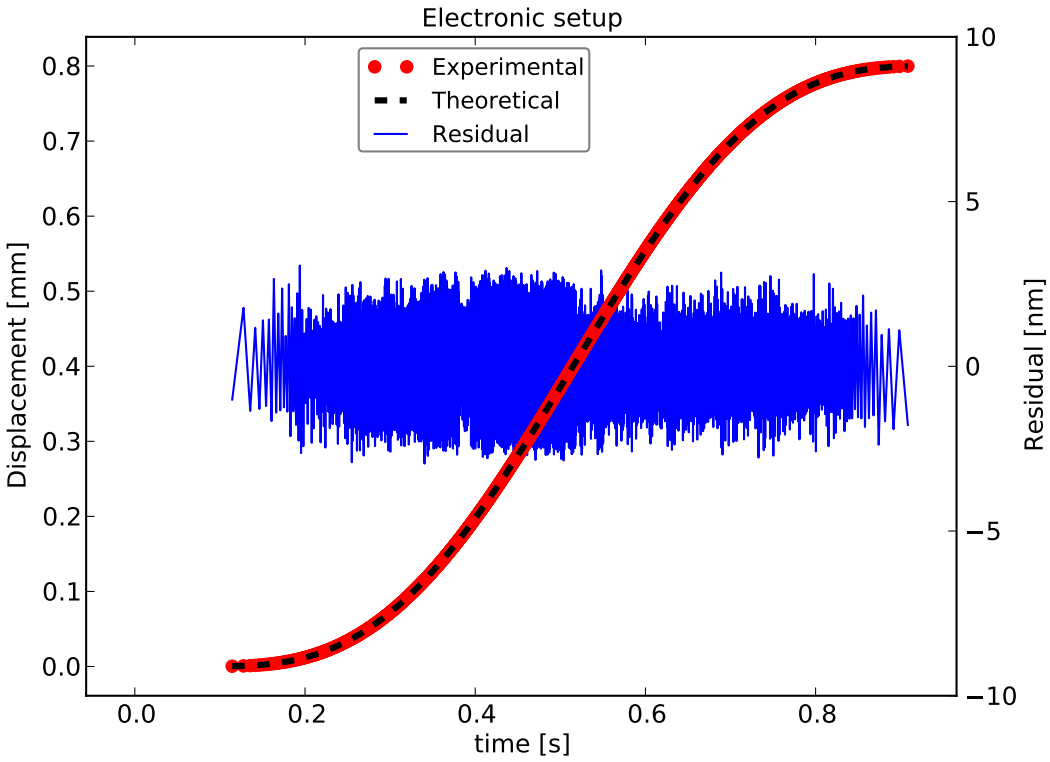

Figure 6.3: Displacement of the electronic setup due to the applied frequency sweep. The red dots indicate the displacement, dependent on the number of zero-crossings. The theoretical displacement fit is indicated by the dashed black line, and the residuals are depicted in blue.

With the results of the electronic setup, we can conclude that the DDS is able to accurately generate both the frequencies and the frequency sweep required for the optical conveyor. More importantly, we can conclude that our method of locating the zero crossings of the real signal is a good way to measure the displacement of the standing wave. The next step for the optical conveyor is to test the displacement of the anti-nodes by overlapping two laser beams with each other. The results of this experiment are discussed in the next section.

6.3 Optical conveyor prototype

In the prototype setup of the optical conveyor, two laser beams are overlapped. The resulting beat note, i.e. the signal with the difference frequency of the two beams, is measured using a fast photodiode. In the conveyor prototype, three channels of the DDS are used to drive $\mathrm{AOM_{cw}}$, $\mathrm{AOM_{ccw}}$, and $\mathrm{AOM_{pilot}}$. $\mathrm{AOM_{cw}}$ is driven with $f_{\mathrm{cw}} = 80\,\mathrm{MHz}$, $\mathrm{AOM_{pilot}}$ with $f_{\mathrm{pilot}} = 85\,\mathrm{MHz}$, and $\mathrm{AOM_{ccw}}$ with $f_{\mathrm{cw}} + \Delta\omega_{\mathrm{L}}(t)$.

The frequency sweep used in the optical conveyor prototype was generated using a cosine signal without exceeding $a_{\max}$. The parameters with which the sweep was generated are listed in Table 6.2. Note that with respect to the parameters for the frequency sweep in the electronic setup, a longer displacement and different number of idlers were used. This is done to test the performance of the DDS further.

As indicated in Section 5.2.3.1, the sweep time is related to the displacement. By choosing a longer displacement the sweep time is thus increased. With the difference in number of idlers, the time interval with which each frequency is generated is halved. By doing so, the number of frequencies send to the DDS is thus increased drastically compared to the electronic setup. The operation of the DDS while sending larger amounts of data can now be investigated.

Property	Symbol	Value
Displacement	d	$2300\,\mu\text{m}$
Maximum jerk	$j_{\max}$	$0.05\,\text{m/s}^3$
Maximum acceleration	$a_{\max}$	$0.02\,\text{m/s}^2$
Number of idlers	N_{idlers}	32

Table 6.2: Frequency sweep parameters for the optical conveyor prototype measurement.

The generated frequency sweep has a maximal frequency of $\Delta\omega_{\text{L,max}} = 2\pi \cdot 4.83\,\text{kHz}$ and a reached acceleration of $a_{\text{reached}} = 9.71 \times 10^{-3}\,\text{m/s}^2$. The maximal frequency corresponds to a maximal velocity of $v_{\max} = 3.77\,\text{mm/s}$. The sweep would cause the atoms to heat by $\Delta T = 1.22 \times 10^{-2}\,\text{pK}$.

The displacement obtained with the conveyor prototype is plotted in Figure 6.4. Here the red dots indicate the displacement due to the number of zero-crossings, the black dashed line the theoretical fit of the experimental displacement, and in blue the residual.

We note that the residual is considerably larger than that of the electronic setup. At the end of the sweep, the displacement of the anti-node is off by 150 nm. When positioning atoms at a distance of $\lambda/2$ above the sample surface, the residual and displacement are in the same order of magnitude. Therefore, with the current experimental and theoretical displacement mismatch, the atoms cannot be positioned precisely enough. From Figure 6.4, we do observe that the residual is dependent on the number of zero-crossings. The zero-crossing distribution varies in time due to the frequency sweep. A low number of zero-crossings results in a larger residual at the beginning and end of the sweep. In the center of the sweep the zero-crossing distribution is the smallest. Hence, the theoretical fit is more accurate resulting in a smaller residual.

From the results obtained in Section 6.2, we are able to exclude the DDS and the

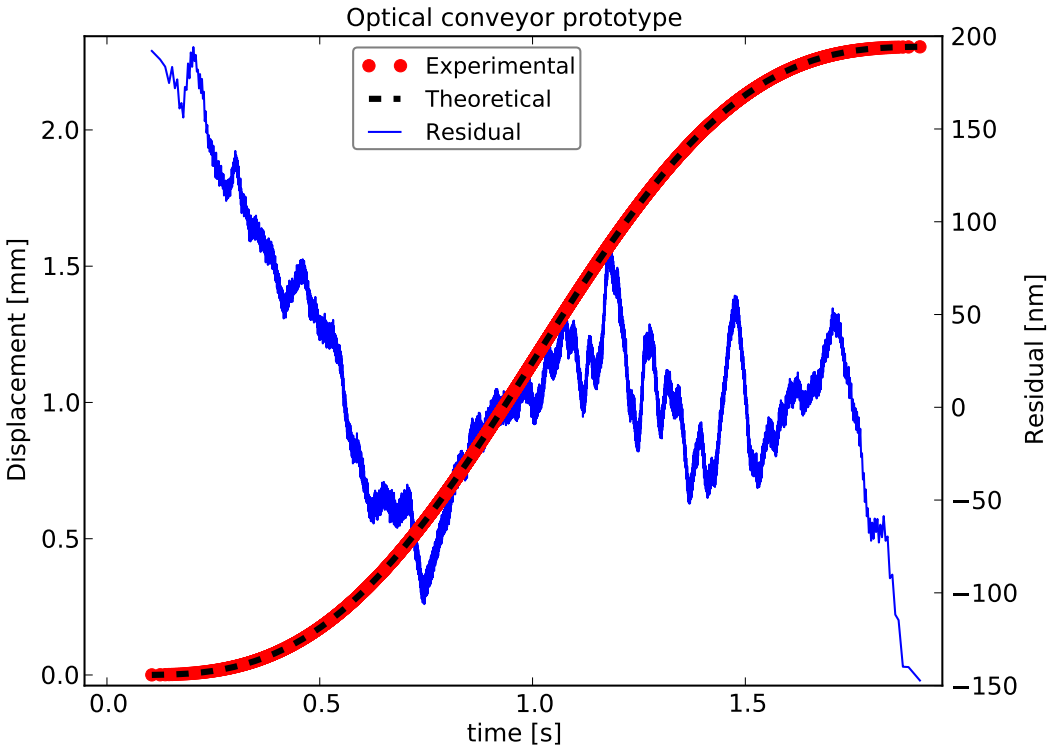

Figure 6.4: Displacement of the optical conveyor prototype due to the applied frequency sweep. The red dots indicate the displacement, dependent on the number of zero-crossings. The theoretical displacement fit is indicated by the dashed black line, and the residuals are depicted in blue.

frequency mixer. The residual in the electronic setup was small. The origin of the residual in the conveyor prototype must thus be optical. The conveyor prototype was also tested using the same frequency sweep that was used in the electronic setup. The result obtained with this frequency sweep was similar to that of Figure 6.4. The visible differences were the total displacement and sweep time.

As discussed in Section 5.3.2, an additional phase ϕ is obtained due to mechanical vibrations. This phase is included in the signal of the fast photodiode. It is likely the reason for the larger residual compared to the electronic setup. As we want to compensate for these mechanical vibrations, we need a real time method of measuring the phase ϕ as opposed to the data analysis method used above. To that end, a fourth channel of the DDS is utilized to generate a frequency equal to $f_{\mathrm{DDS}} = 2f_{\mathrm{pilot}} + \Delta\omega_{\mathrm{L}}(t)$. The factor two is due to the fact that both the clockwise and counter-clockwise propagating beams are deflected by $\mathrm{AOM}_{\mathrm{pilot}}$. The overlapped beam thus contains twice f_{pilot}. By electronically mixing f_{DDS} with f_{cw}, the phase noise $\phi(t)$, is obtained. In Figure 6.5, the phase noise is plotted in purple against the residual, in blue. The residual is shifted upward by 200 nm to obtain a good

comparison. Note that these traces obtained by the different methods were obtained in different runs of the experiment.

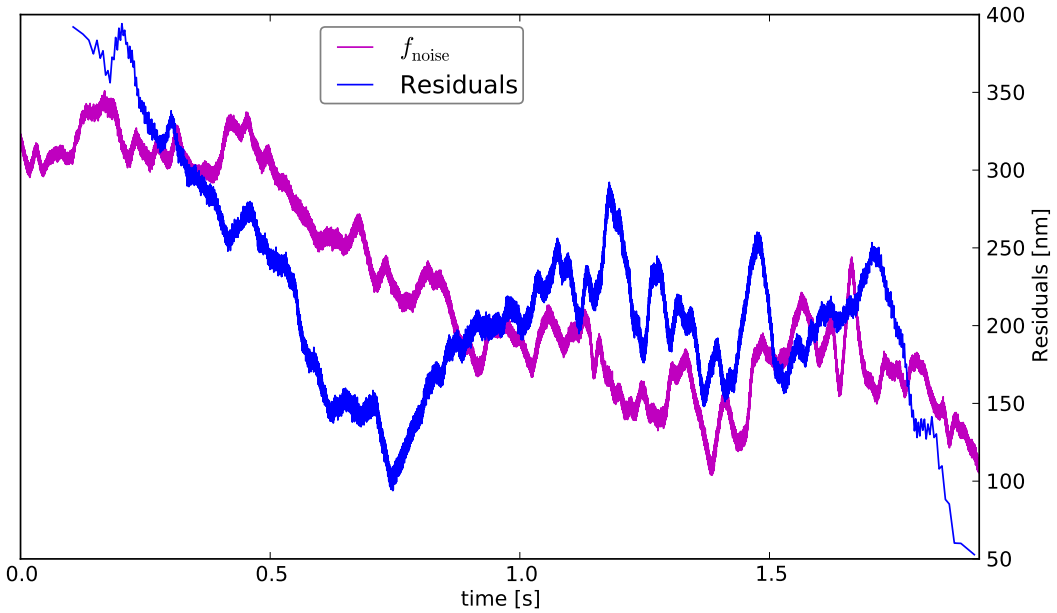

Figure 6.5: Comparison between f_{noise} in purple and the residuals in blue. f_{noise} is obtained by mixing $f_{\mathrm{DDS}} = 2f_{\mathrm{pilot}} + \Delta\omega_{\mathrm{L}}(t)$ with the signal measured via a fast photodiode. The residuals are obtained by comparing the experimental displacement with the theoretical displacement. For a good comparison, the residuals are shifted upwards by $200\,\mathrm{nm}$. Note that the traces are obtained in different runs of the experiment.

From Figure 6.5, similar characteristics can be found between the phase noise and the residual of the conveyor prototype. Both deviate more at the beginning and end of the sweep with respect to their values at the center of the sweep. The overall trend of both the phase noise and the residual is similar. From this we conclude that the phase noise could be used as an error signal for a feedback mechanism. Using this mechanism, the additional phase can be minimized. Reducing the additional phase, would thus reduce the error in the position of the atom cloud with respect to the sample surface.

With the displacement from the optical conveyor prototype we can conclude that we are able to move the anti-nodes of the standing-wave. To this end, a setup for the optical conveyor is designed. This setup could readily be implemented into the experiment. It is discussed in the following section.

7 Optical Conveyor: Final Design

In this section the final setup for the optical conveyor is presented. This setup was designed after the promising results obtained for the optical conveyor prototype and tests of mirror galvanometers, discussed by Kluit [21].

In the experiment, atoms will be transferred from the ODT into the optical conveyor. With the conveyor, the atoms can be positioned to a height of $\lambda/2$ above the sample surface. As discussed by Kluit, from this point the atoms still need to be moved over the sample surface [21]. This can be achieved by translating the optical conveyor in two-dimensions. The device which translates the optical conveyor will be referred by as the "scanner", which consists of four mirror galvanometers, two for each beam of the optical conveyor.

Each mirror galvanometer consists of a galvanometer with a mirror mounted to its shaft. The galvanometer rotates the mirror when an electric current is applied. Using two mirror galvanometers, a laser beam reflected on the mirrors can thus be translated in two-dimensions. The theory, setup and results of a single scanner consisting of two mirror galvanometers are discussed by Kluit [21].

As explained in Section 5.1, two counterpropagating beams interfere with each other to form the optical conveyor. Both beams enter the 3D-MOT chamber; one from the bottom and one from the top. Hence, the anti-nodes can be displaced along the y-axis. Each beam will be steered by two mirror galvanometers. Next to the beam used for the optical conveyor, a second beam enters the 3D-MOT chamber from the top. This beam can be used to probe the position of the sample with respect to the optical conveyor. The lowest level, responsible for the beam entering the 3D-MOT chamber from the bottom is referred to as the "lower arm". The lower arm is discussed in Section 7.1. The highest level, responsible for the beams entering the 3D-MOT chamber from the top is referred to as the "upper arm", which is discussed in Section 7.3.

With the setup it will also be possible to introduce a different beam to the setup. This beam can be used for pumping or probing. For both arms, the beam included will be referred to as the probe beam. For the lower and upper arm they are discussed in Sections 7.2 and 7.3, respectively. In Section 7.4, the side view of the setup is discussed indicating the heights of the previous discussed levels [2].

[2] The images, without caption, of the design are also included in Appendix B on a slightly bigger scale.

7.1 Lower arm

The displacement of the standing-wave is achieved by introducing a frequency difference between the two laser beams which form the optical conveyor. To this end, a laser beam is passed through an AOM. Note that this AOM is not indicated in Figure 7.1. The frequency of the beam can be controlled via the AOM and a DDS. After the beam passed the AOM, it is coupled into a fiber and subsequently coupled out in the setup of the lower arm given in Figure 7.1. The beam waist after the out-coupler is $w_0 \approx 1100\,\mu\text{m}$.

As we have seen in Section 3.2.2, the focus we achieved with the ODT had a beam waist of $w_x = 40.0\,\mu\text{m}$ in the x-direction. Due to the steep trap depth of the ODT ($U_0 = -1.03\,\text{mK}$), the atoms are localized at the bottom of their potential trap. This means that the atoms are located in a region smaller than the focus of the ODT. For an efficient transfer of the atoms from the ODT into the optical conveyor, the focus of the optical conveyor can therefore be smaller than that of the ODT. The focus will have a waist of $w = 37.5\,\mu\text{m}$, which is achieved using a $f = 30\,\text{mm}$ lens.

For a Gaussian beam, the beam waist propagation in space is given by [23]

$$w(z) = w_0\sqrt{1 + (z/z_\text{R})^2}. \tag{7.1}$$

Using Equation 7.1, we find that a beam waist of $200\,\mu\text{m}$ is required to obtain a focus of $37.5\,\mu\text{m}$ using a $f = 30\,\text{mm}$ lens. The beam waist after the out-coupler is decreased using a telescope, consisting of a set of achromatic lenses with focal lengths of 100 mm and $-20\,\text{mm}$, respectively. This results in a lens separation between the principal planes of 80 mm and a magnification of 0.2. The half-waveplate ($\lambda/2$) in front of the telescope is used to control the polarization of the beam. It thus determines the fraction of light that is transmitted and reflected by the polarizing beam splitting cube (PBS) in Figure 7.1. The PBS will be used to introduce the probe beam into the lower arm, which is discussed in Section 7.2.

As mentioned earlier, mirror galvanometers are used for the displacement of the laser beams that form the optical conveyor. The displacement is achieved by introducing an angle to the beam via the rotation of a mirror galvanometer. This is achieved by placing the first mirror galvanometer focal length away from the first lens $f = 100\,\text{mm}$. The first mirror galvanometer is referred to as "Galvo 1". It is placed such that the axis of rotation is along the y-axis. The angle introduced to the beam is therefore in the x-direction. By placing another $f = 100\,\text{mm}$ lens a focal length away from Galvo 1, this angle is translated into a displacement of the focus. The described configuration is known as a $4f$-imaging system. Such systems are commonly used in scanning confocal microscopy [41].

For the displacement of the beam in the y-direction another $4f$-imaging system in combination with a mirror galvanometer is utilized. The second mirror galvanometer

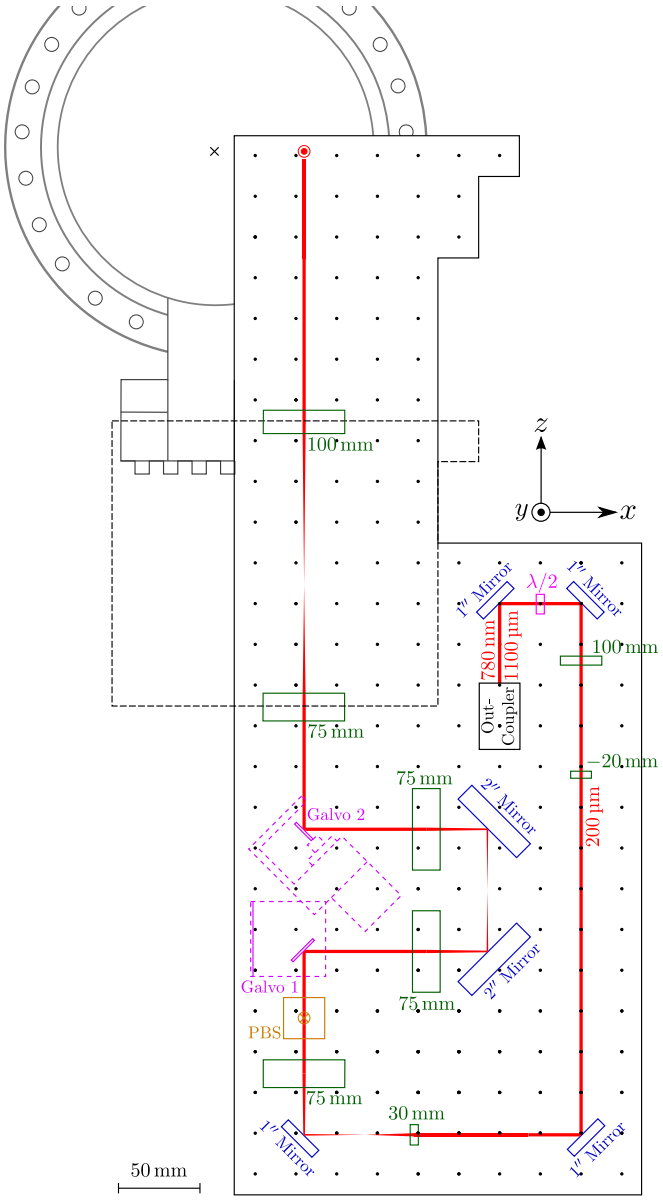

Figure 7.1: Schematic overview of the lower arm. The laser is depicted in red, polarizing beam splitting (PBS) cubes in brown, lenses in dark green, mirrors in blue, waveplates in pink, and Galvo 1 and 2 with their mount in purple.

is referred to as "Galvo 2". Due to spatial constraints, Galvo 2 is placed such that the axis of rotation lies in the same plane as the beam. Therefore, an additional unwanted displacement in the x-direction is obtained. The unwanted displacement is discussed in Section 7.1.1.

Indicated in Figure 7.1 by the dashed line, is the platform that is used to mount the rotation stage. This stage is required for the movement of the ODT as discussed in Section 3.2.2. The platform introduces a height constraint, both Galvo 1 and 2 cannot be placed there. Therefore, a third and final $4f$-imaging system is used to image the focus into the chamber after the second $4f$-imaging system. Note that the second lens for the final $4f$-imaging system is indicated in Figure 7.5. The focal lengths of the final $4f$-imaging system of the lower arm are 100 mm. With these focal lengths, the focus is obtained ≈ 5 mm above the sample holder. This is the estimated position at which the ODT will position the atoms.

7.1.1 Displacement deviation

As mentioned in Section 7.1, the axis of rotation of Galvo 2 is in the same plane as the beam. When rotating the mirror of Galvo 2, the displaced beam thus describes an arc. This introduced an unwanted displacement in the x-direction on the lens located after Galvo 2. To determine this deviation, we will calculate the displacement in both directions at the principle plane of the lens.

To describe the system, a spherical coordinate system is used. The cartesian coordinates of an arbitrary unit vector are given by

$$x^2 + y^2 + z^2 = 1 \tag{7.2}$$
$$x = \sin(\theta)\cos(\phi), \tag{7.3}$$
$$y = \sin(\theta)\sin(\phi), \tag{7.4}$$
$$z = \cos(\theta), \tag{7.5}$$

Using Figure 7.2(a) and Equations 7.3, 7.4, and 7.5 we are able to describe the unit vectors in Figure 7.2(a) using spherical coordinates as (ρ, θ, ϕ). We obtain

$$\hat{n} = \left(1, \frac{\pi}{2}, 0\right), \tag{7.6}$$
$$\hat{n}' = \left(1, \frac{\pi}{2} - \alpha, 0\right), \tag{7.7}$$
$$\hat{i} = \left(1, \frac{\pi}{2}, \pi - \beta\right), \tag{7.8}$$
$$\hat{o} = \left(1, \frac{\pi}{2}, \beta\right), \tag{7.9}$$

where α denotes the angle between the displaced normal unit vector $\hat{n}'$ of Galvo 2 and the x-axis, and β the angle between the incident beam $\hat{i}$ on Galvo 2 and the x-axis. In the neutral position of Galvo 2, the normal unit vector $\hat{n}$ of the mirror is along the x-axis. In this case, the reflected beam is denoted by $\hat{o}$. Rotating the mirror of Galvo 2, changes α which introduces φ. Due to the law of reflection, φ denotes the angle under which $\hat{o}'$ is reflected.

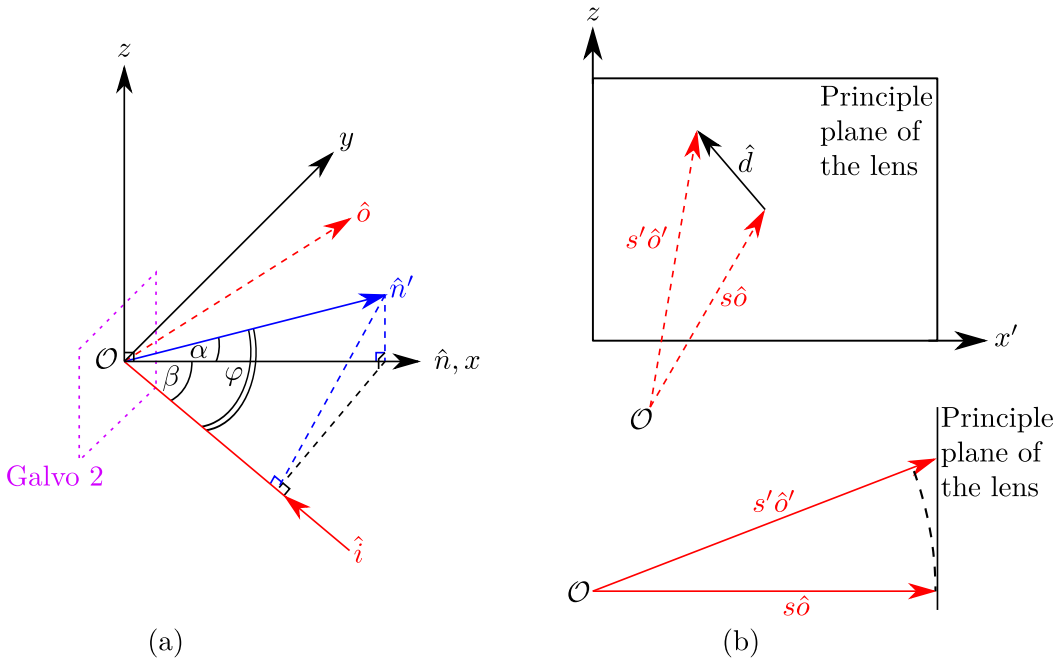

Figure 7.2: (a) An incident beam $\hat{i}$ is reflected on Galvo 2, resulting in $\hat{o}'$ when the normal of Galvo 2 $\hat{n}'$ is displaced out of the plane of $\hat{i}$. The reflected beam describes an arc, resulting in an unwanted displacement. (b) The displacement of the reflected beam on the principle plane of a lens.

As can be observed from Figure 7.2(a), the relation between the incident beam $\hat{i}$, the displaced reflected beam $\hat{o}'$, and the displaced normal unit vector $\hat{n}'$ of the mirror can be given by

$$\hat{n}' = \frac{\hat{o}' - \hat{i}}{||\hat{o}' - \hat{i}||}. \tag{7.10}$$

The displaced beam $\hat{o}'$ results in

$$\hat{o}' = ||\hat{o}' - \hat{i}||\hat{n}' + \hat{i}, \tag{7.11}$$

where $||\hat{o}' - \hat{i}||$ denotes the length of $\hat{o}' - \hat{i}$.

From trigonometry, an expression for $||\hat{o}' - \hat{i}||$ is obtained

$$||\hat{o}' - \hat{i}|| = \sqrt{2 + 2\cos(2\varphi)}, \tag{7.12}$$

$$= 2\cos(\varphi). \tag{7.13}$$

In the neutral position of Galvo 2 we have $\varphi = \beta$. When the mirror is rotated, this generally no longer holds. From Figure 7.2(a), we obtain relations for α and β. These

are given by $\cos(\alpha) = \hat{n} \cdot \hat{n}'$ and $\cos(\beta) = \hat{i} \cdot \hat{n}$. The angle φ can be expressed by

$$\cos(\varphi) = \hat{i} \cdot \hat{n}', \tag{7.14}$$
$$= \cos(\alpha)\cos(\beta). \tag{7.15}$$

The expression for the displaced beam $\hat{o}'$ can thus be written using cartesian coordinates as

$$\hat{o}' = 2\cos(\varphi)\hat{n}' + \hat{i}, \tag{7.16}$$
$$= \begin{pmatrix} 2\cos(\varphi)\cos(\alpha) - \cos(\beta) \\ \sin(\beta) \\ 2\cos(\varphi)\sin(\alpha) \end{pmatrix}. \tag{7.17}$$

To obtain the displacement on the lens, the expression in Equation 7.17 is projected onto the principle plane of a lens. The principle plane is "placed" perpendicular to $\hat{o}$ at a distance s from the origin. The displaced reflected beam $\hat{o}'$ is thus projected onto the principle plane. The following relation is obtained

$$s'\hat{o}' \cdot \hat{o} = s, \qquad \hat{o} = \begin{pmatrix} \cos(\beta) \\ \sin(\beta) \\ 0 \end{pmatrix}, \tag{7.18}$$

where s' denotes the distance from the mirror to the principle plane for the displaced reflected beam $\hat{o}'$.

From Equation 7.18, an expression for s' can be obtained

$$\frac{s}{s'} = \cos(\beta)\left[2\cos(\varphi)\cos(\alpha) - \cos(\beta)\right] + \sin^2(\beta), \tag{7.19}$$
$$= 2\cos(\varphi)\cos(\alpha)\cos(\beta) - \cos(2\beta) \equiv Q(\alpha, \beta, \varphi), \tag{7.20}$$

where for convenience the ratio s/s' is denoted by Q.

In Figure 7.2(b), the displacement of the beam on the principle plane is indicated. With the expression for s' in Equation 7.20, the expression for $\hat{d}$ can be given by

$$s'\hat{o}' - s\hat{o} = s\left[\frac{\hat{o}'}{Q} - \hat{o}\right] \equiv \hat{d}, \tag{7.21}$$
$$= s\begin{pmatrix} \frac{2\cos(\varphi)\cos(\alpha) - \cos(\beta)}{Q} - \cos(\beta) \\ \frac{\sin(\beta)}{Q} - \sin(\beta) \\ \frac{2\cos(\varphi)\sin(\alpha)}{Q} \end{pmatrix}. \tag{7.22}$$

By decomposing $\hat{d}$ into components in the x'- and z-direction, both the horizontal and vertical components of the displacement of the beam are obtained. These components

are functions of α and β. For the x'-direction we obtain

$$\frac{d_{x'}^2}{s^2} = \left[\frac{2\cos(\varphi)\cos(\alpha) - \cos(\beta)}{Q} - \cos(\beta)\right]^2 + \left[\frac{\sin(\beta)}{Q} - \sin(\beta)\right]^2, \tag{7.23}$$

$$= \cos^2(\beta)\left[\frac{2\cos^2(\alpha) - 1}{2\cos^2(\alpha)\cos^2(\beta) - \cos(2\beta)} - 1\right]^2 + \sin^2(\beta)\left[\frac{1}{2\cos^2(\alpha)\cos^2(\beta) - \cos(2\beta)} - 1\right]^2. \tag{7.24}$$

For the displacement in the z-direction we obtain

$$\frac{d_z}{s} = \frac{2\sin(\alpha)\cos(\alpha)\cos(\beta)}{2\cos^2(\alpha)\cos^2(\beta) - \cos(2\beta)}. \tag{7.25}$$

On the lower- and upper arm of the setup for the optical conveyor, the angle between the incident and reflected beam on Galvo 2 is $\beta = 45°$. The distance from the mirror to the principle plane of the lens is by definition $s \equiv f$. Equations 7.24 and 7.25 thus simplify to

$$d_{x'} = f\tan^2(\alpha), \tag{7.26}$$

and

$$d_z = \sqrt{2} f \tan(\alpha). \tag{7.27}$$

The maximum angle for both Galvo 1 and Galvo 2 is 5° [21]. With angles of 2.5° and 5° we obtain a vertical displacement of $d_z = 4.63\,\text{mm}$ and $d_z = 9.28\,\text{mm}$, respectively. The horizontal displacement equals $d_{x'} = 0.14\,\text{mm}$ and $d_{x'} = 0.57\,\text{mm}$, respectively. This corresponds to deviations of 3.02 % and 6.14 % in the horizontal direction for angles of 2.5° and 5°, respectively. The unwanted deviations are small enough to be neglected as the deviation will be equal for both beams used to form the optical conveyor.

7.2 Probe level

The function of the probe level is to introduce a beam to the optical conveyor that can be used for pumping or probing. The layout of the probe level is given in Figure 7.3. Here, the beam is introduced to the setup via the out-coupler. Similar to the lower arm, the frequency of the beam is controlled by a DDS. The DDS sends the frequency to an AOM.

As mentioned earlier, a PBS is located on the lower arm. Using this PBS, the probe beam can be introduced into the lower arm. The amount of light that is transmitted

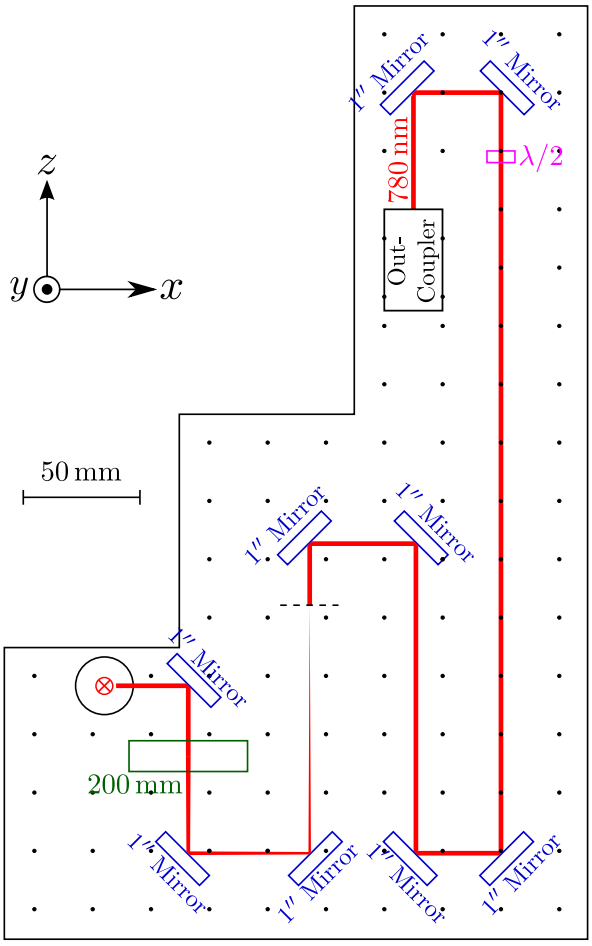

Figure 7.3: Schematic overview of the probe level. The laser is depicted in red, lenses in dark green, mirrors in blue, and waveplates in pink.

and reflected is controlled using a half wave-plate, located after the out-coupler on the probe level.

In Figure 7.3, the dashed line denotes the image plane of the $4f$-system. The beam size at the image plane will be translated by the several $4f$-systems of the lower arm towards the sample. The image plane thus determines the size of the probe beam. The space in between the wave-plate and the imaging plane can be utilized for a telescope and lens to obtain the desired beam dimensions.

After the beam has the desired dimensions, it is introduced into the first $4f$-imaging system. The first lens of the $4f$-imaging system has been replaced by a $f = 200\,\mathrm{mm}$ lens due to spatial constraints. This lens is placed a focal length away from both

the imaging plane and Galvo 1. Note that the first $4f$-imaging system consists of two lenses with unequal focal lengths. A telescope with a magnification of 0.375 is thus created. When obtaining the desired beam dimensions at the image plane, this magnification should be taken into account. When introduced by the PBS to the lower arm, the beam is directed into the 3D-MOT chamber as described in Section 7.1.

7.3 Upper arm

Similar to the beam on the lower arm, the beam first passes an AOM before introduced to the upper arm. The frequency of the beam is controlled by a DDS. In Figure 7.4 the schematic overview of the upper arm is given.

The most important difference with respect to the lower arm is the addition of an AOM on the upper arm. This AOM is used to obtain both the negative and positive first orders of both the beam introduced by the out-coupler (clockwise) and the beam that is retro-reflected on the sample surface (counter-clockwise). The negative first order of the clockwise propagating beam is used to probe the position of the sample with respect to the optical conveyor. The zeroth order of the clockwise propagating beam is used to interfere with the beam from the lower arm to construct the optical conveyor. For the counter-clockwise propagating beam, the positive first order is used for the feedback mechanism of the optical conveyor.

The lower- and upper arm are constructed under the assumption that the AOM on the upper arm will be a ATM-801A2 from IntraAction. For $\lambda = 780\,\text{nm}$, this AOM has a separation angle of 14.6 mrad between the zeroth and first order. The maximal displacement of the focus due to the rotation of Galvo 1 and 2 equals 10 mm [21]. Since the diameter of the sample will be $\approx 10\,\text{mm}$, the separation between both beams should thus be small. This will allow the scanner to move the optical conveyor over a large as possible area on the sample surface. The separation of both beams on the upper arm is determined via the separation angle of the AOM and the lens after the AOM. The lens is placed a focal length away from the AOM. This makes the zeroth and negative first order parallel. In this case, the following expression is obtained

$$\Delta x_{\text{f}} = f \tan(\theta), \tag{7.28}$$

where Δx_{f} denotes the separation between both foci, and $\theta = 14.6\,\text{mrad}$ the separation angle of the AOM.

From Equation 7.28, we observe that Δx_{f} decreases for smaller focal lengths and/or a smaller separation angle. However, a smaller focal length also means a smaller beam waist propagating through the crystal of the AOM. For a good operation, the AOM needs a minimum beam waist of 200 µm. Therefore, a $f = 30\,\text{mm}$ lens is used after the AOM. With this lens, the desired focus is obtained. The resulting foci are separated by $\Delta x_{\text{f}} = 0.36\,\text{mm}$. The focus due to the zeroth order will be used to

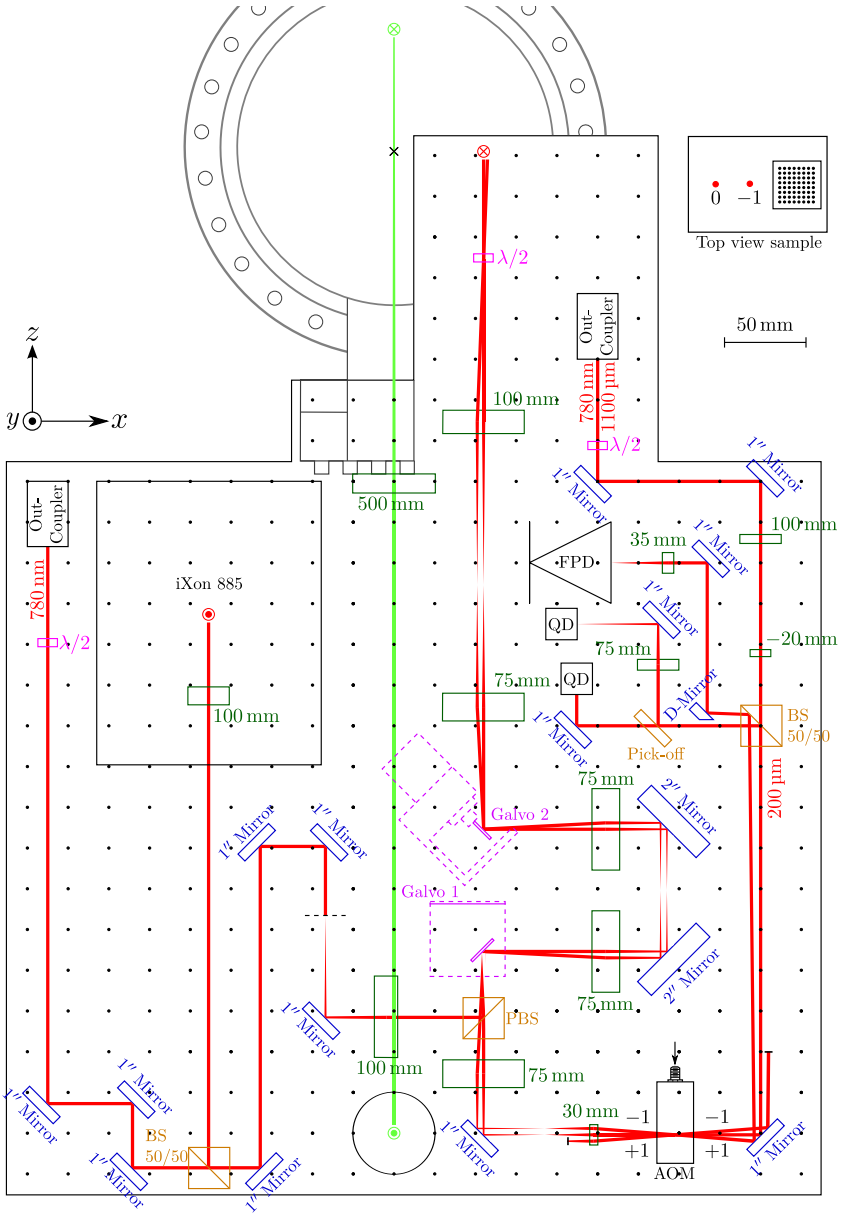

Figure 7.4: Schematic overview of the upper arm. The laser is depicted in red, polarizing beam splitting (PBS) cubes in brown, lenses in dark green, mirrors in blue, waveplates in pink, and the mirror galvanometers with their mount in purple.

trap the atoms. The focus due to the negative first order will be used to probe the position of the sample surface. We will refer to it as the pilot focus. As indicated in Section 7.1, an incident beam waist of 200 µm is required. This beam waist is sufficient for the AOM. Note that the foci separation could be further decreased

using a smaller separation angle without effecting the incident beam waist for the AOM. This however, will make it more difficult to separate both beams from each other. This is required for the feedback mechanism as indicated in Figure 7.4.

After the $f = 30\,\text{mm}$ lens, the main focus and the pilot focus are picked up by the $4f$-imaging systems containing Galvo 1 and Galvo 2. To ensure both beams for the optical conveyor remain overlapped, both Galvo 1 and Galvo 2 are mirrored on the upper arm with respect to the lower arm. Similar to the lower arm, an unwanted displacement is obtained when rotating Galvo 2. After the second $4f$-imaging system, both the main focus and the pilot focus are imaged at a distance of 5 mm above the sample holder. This is achieved via the final $4f$-imaging system. The second $f = 100\,\text{mm}$ lens for this final $4f$-imaging system is indicated in Figure 7.5.

Similar to the lower arm, a probe beam could be introduced for pumping or probing. The out-coupler of this probe beam is indicated on the left in Figure 7.4. Again, the light first passes through an AOM before coupled out into the setup of the upper arm. From the out-coupler, the polarization of the beam is controlled by a $(\lambda/2)$ half-waveplate. With the right polarization, the probe can be introduced into the first $4f$-imaging system. Similar to the probe beam for the lower arm, a magnification is obtained. When obtaining the desired beam dimension, this should be taken into account. With respect to the probe level of the lower arm an additional 50/50 beam splitting cube is introduced. With this cube, a part of the counter-clockwise propagating beam is split off towards a CCD camera. Note that therefore the counter-clockwise propagating beam first needs to be reflected by the PBS. The polarization of the counter-clockwise propagating beam is controlled via a half-waveplate located in the final $4f$-imaging system. The transmitted part is used for the feedback mechanism.

For the feedback mechanism, both the positive first- and zeroth order of the counter-clockwise propagating beam are utilized. The feedback mechanism consist of two parts; one to synchronise the galvanometers, and one to compensate for the phase noise in the optical conveyor. Note that the latter is similar to the error signal obtained with the prototype setup of the optical conveyor discussed in Section 5.3.2.

To split off the zeroth order a 50/50 beam splitting cube is used, located on the right in Figure 7.4. After the cube, the zeroth order is split once more. Both parts of the zeroth order are directed towards quadrant diodes which can measure displacement and angle errors. By focusing the beam on a quadrant diode the angle error between both beams of the optical conveyor is measured. Both signals obtained by the quadrant diodes are used as an error signal for a proportional-integral-derivative (PID) controller. The PID gives feedback to both Galvo 1 and 2 in order to minimize the error. It ensures that both beams for the optical conveyor remain overlapped during translation. The quadrant diode and PID controller are discussed extensively by Kluit [21].

Using a D-shaped mirror, the positive first order of the counter-clockwise propagating beam is reflected towards a fast photodiode. The signal obtained by the fast photodiode is mixed with a signal of the DDS equal to $f_{\mathrm{DDS}} = 2f_{\mathrm{AOM}} + \Delta\omega_{\mathrm{L}}(t)$, where f_{DDS} denotes the frequency output of the DDS, f_{AOM} the driving frequency of the AOM, and $\Delta\omega_{\mathrm{L}}(t)$ the frequency sweep. The output of the frequency mixer equals the additional phase, which can be used for an error feedback loop.

As can be seen from Figure 7.4, the level of the upper arm will also be used for the optics required to reflect the cross beam into the 3D-MOT chamber. Note that the "cross beam" is directed to this level from the top layer of the experimental setup of the ODT. The cross beam is required to form the crossed-beam trap. This trap confines the atoms to a smaller region of space but also allows us to apply evaporative cooling, should we need to. On the upper arm, the cross beam is focussed using a $f = 500\,\mathrm{mm}$ lens. With this lens, the desired dimensions for the cross beam are obtained.

7.4 Side view

In Figure 7.5, the side view of the possible setup for the optical conveyor is given. In this figure, the heights for each levels and beams are indicated. The side view has been constructed for the case of symmetry between the lower- and upper arm.

For symmetry between the lower- and upper arm, the beam height on these levels is identical. The beam height on the lower arm has been chosen such that a mirror can be mounted underneath the 3D-MOT chamber. With the space between the two arms, the beam height for the probe level has been defined to be 50 mm. This increase the accessibility of the probe level with respect to the upper arm.

In Figure 7.5, the horizontal dashed line indicates the 5 mm distance above the sample holder. Both the second lenses of the final $4f$-imaging systems of the lower- and upper arm are placed more than a focal length away from the horizontal dashed line. This is due to the glass window with a thickness of 20 mm through which the light propagates before entering the vacuum chamber. Since the refractive index of glass is higher than that of air or vacuum, the focus obtained with the lenses is thus shifted further away. The shift equals 9.9 mm.

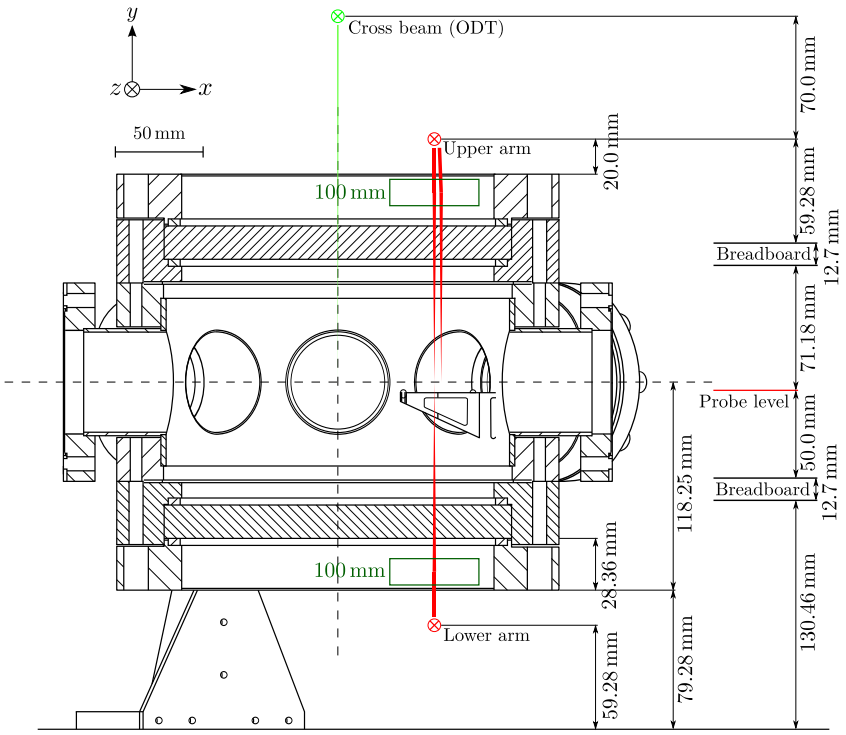

Figure 7.5: Side view of the possible setup for the optical conveyor. Depicted are beams of the lower arm, probe level, and upper arm in red. The cross beam for the ODT is depicted in light green. In the figure the beam heights are indicated for symmetry between the lower and upper arm.

8 Conclusion

In this thesis we have investigated both the trapping of atoms in an optical dipole trap and the displacement of anti-nodes in an optical conveyor. Conclusions are drawn for each of them in the following sections.

Optical dipole trap

We have successfully trapped 2.1×10^5 atoms in an ODT. We obtained an atom lifetime of up to $6.4 \pm 2.9\,\mathrm{s}$ using a laser power of $10.4\,\mathrm{W}$.

We successfully modeled the atomic density evolution in the ODT, considering losses both due to collisions with the background gas and collisions between two trapped atoms as compared to density dependent losses. We found that the trap depth does not influence the losses due to the background or due to two-body losses. The order of magnitudes we obtained for both losses are in good agreement with lifetime measurements in literature [13, 36, 37].

We found that the ratio of trapped atoms over the trap depth is in the same order of magnitude for different trap depths. A possible explanation for N_0/U_0 to be similar is that there are atoms with temperatures very close to the temperature required to escape the trap. This could imply that the atoms spill out of the trap before colliding with other trapped atoms.

Our magneto-optical trap contains $(4.0 \pm 0.2) \times 10^{10}$ atoms. We achieved a transfer efficiency from the magneto-optical trap into the optical dipole trap of $\sim 4 \times 10^{-4}\,\%$. This is mainly because the ODT is simply much smaller than the MOT. The transfer efficiency could be increased by ramping both the detuning of the cooling beams and the magnetic field of the MOT, and by ramping the re-pump power of the MOT beams [36, 42]. By ramping the detuning of the laser light of the MOT away from resonance, the velocity dependent force acting on the atoms becomes weaker. Hence, the MOT is decompressed and cooled as the hotter atoms are allowed to escape more easily. By now ramping up the magnetic field, the atoms are compressed because the force becomes more strongly dependent on position. This way, we could obtain a high density of cold atoms in the MOT.

Arnold and Barrett trapped ^{87}Rb using a crossed-beam trap configuration. By ramping both the detuning of the laser light and the magnetic field, they achieved a transfer efficiency from the MOT into the ODT of $N_0/N_{\mathrm{MOT}} = 0.7\,\%$ [42]. Since our laser parameters are comparable, we should be able to obtain a similar transfer efficiency. The aim in our experiment is thus to initially trap $\sim 2.5 \times 10^6$ atoms with the ODT. This large number is important for evaporative cooling and allows us to lose some atoms while positioning them above the sample surface. Considering the number

of atoms in our MOT and the results of Arnold and Barrett, we should be able to achieve this number. Further literature studies have shown that a reduction of the re-pump intensity of the MOT beams during loading of the ODT is required to obtain this number [36]. By reducing the re-pump power, the internal pressure of the MOT becomes weaker thus resulting in a high density of cold atoms in the MOT. This is currently being implemented.

In the future, a cross beam is required to obtain a crossed-beam trap configuration. With such a configuration we can increase the density of the atoms in the focus of the main ODT beam. This will thus increase the number of atoms transferred into the optical conveyor. With a crossed-beam trap, evaporative cooling can also be applied, cooling the atoms to sub-10 µK temperatures. This will reduce the two-body losses and thus increase the lifetime of the atoms in the ODT.

Optical conveyor

For a more precise placement atoms will be moved by a red-detuned optical conveyor, i.e. in the anti-nodes of a standing-wave. We have successfully displaced the anti-nodes of a standing wave. The method of displacement was investigated electronically and optically.

In the electronic setup, we displaced the anti-nodes over a distance of 800 µm with an accuracy of 3 nm. This deviation is due to electronic noise from either the DDS or the DAQ module. From the displacement of the anti-node we can conclude that the DDS works excellently. It will be used in future experiments to generate the frequencies required to displace the standing wave. We also conclude that our method of locating the zero crossings of the signal is a good way to measure the displacement of the standing wave.

In the optical conveyor prototype, we displaced the anti-nodes over a distance of 2300 µm with an accuracy of 150 nm. This is still too large. The difference is most likely caused by a phase noise due to mechanical vibrations. We observed similarities between the phase noise and the displacement deviation. Minimizing the phase noise using an error feedback mechanism will therefore increase the accuracy of the displacement of the anti-nodes.

A setup was designed for the optical conveyor in the experiment. With this setup we will be able to translate the optical conveyor in two-dimensions over the sample surface while keeping both beams overlapped. The setup is to be implemented into the experiment.

9 Acknowledgements

After more than a year at the group of cold atom nanophotonics my research has come to an end. I would like to thank Dries van Oosten and Ole Mussmann for supervising my work. Your knowledge and enthusiasm for experimental physics has been inspiring, which made my own grow even further. I would also like to thank Sandy Pratama and Arjon van Lange. Your door was always open whether it was physics related or just to blow of steam. Make sure you never change Sandy, your occasional "fuck this shit" can be a mood changer.

Besides spending time in the lab, playing ping-pong or training martial arts with Bruno, I also spent some time in my room. I would like to thank my room mates; Zimma Kluit, Bas Meyer Viol, Stephan Wolbers, Bruno van Albada, Christiaan Mennes and Tessa Verboven for all the fun times we had. Lunches with you can hardly be called boring with topics such as what you would do first when you would wake up as a girl or where the apple is on the fruit ladder with respect to the banana. Maybe we still need Tessa's opinion on that matter. During and outside lunch times this lead to memorable quotes such as "Wat is een Zimma?","Bij een nieuwe fiets krijg je altijd drie sleutels. Die doe ik allemaal aan mijn sleutelbos... dan verlies ik ze tenminste alle drie tegelijk", and many more.

Special thanks go out to Zimma, Bas and Stephan who have been there with me since the beginning. Well, for some at least around lunch time each day, right Stephan? Zimma, thank you for company. It was nice to have someone keeping the testosterone level of the room in check. Your daily cups of tea were a delight. I would also like to thank you for being there during the final stages of writing, while the number of people in our room kept on shrinking. Without you it would not have been the same. Bas, thank you for the countless hours we spend in the lab working on the optical dipole setup. We have had our ups and downs but I enjoyed it nonetheless. After half a year in the lab with you, some of your music preferences even rubbed off on me. Stephan, thank you for the help you gave me in coding and the many movies we have seen. I still regret the moment I let you convince me that "I Love Dries" really is the worst movie ever made. While writing this, one scene in particulary even comes to mind... Nevertheless, I have had a great time and I dare to argue this has been the most fun room the Ornstein laboratorium has ever seen. Maybe even the most fun it will ever see.

Without comments and questions, my thesis would not be what it is today. I would like to thank Ole Mussmann, Arjon van Lange, Sandy Pratama, Bruno van Albada, Dolfine Kosters, Tom Steinbusch and Maarten Dobbelaar for reading my thesis in its early stages. Special thanks go out to Ole who read faster than I thought was even possible. Without your fast and accurate comments I would not have been able to finish my thesis this fast.

Last but not least, I would like to thank the excellent technical staff of the group: Paul Jurrius, Frits Ditewig, Dante Killian en Cees de Kok. Without your expertise it would have been harder and maybe even impossible to get the setup for the optical dipole trap running.

For anyone I might have forgotten and is feeling left out, I am sure it was not my intention.

Appendix A ^{87}Rb D_2 hyperfine structure

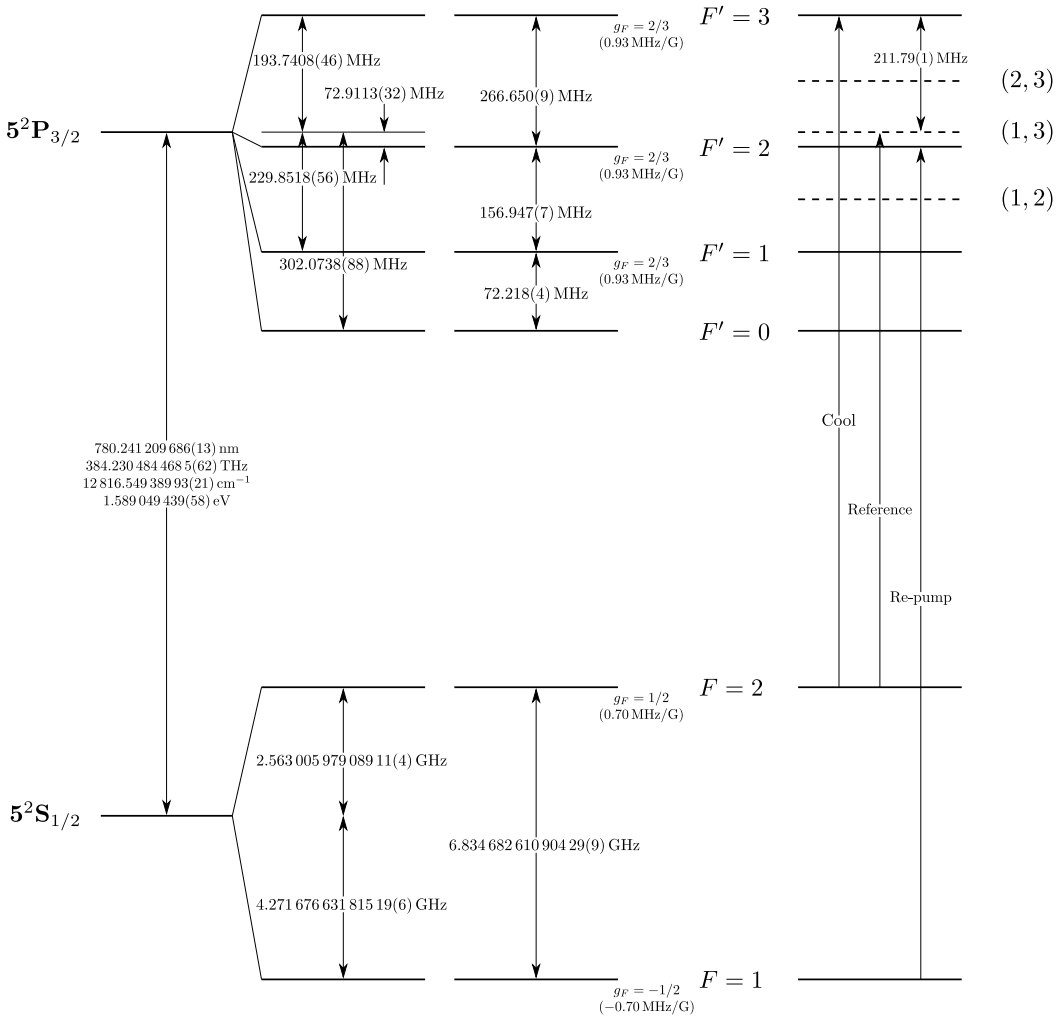

Figure A.1: Rubidium 87 D_2 transition hyperne structure, with frequency splittings between the hyperfine energy levels taken from [22]. The relative hyperfine shifts are shown to scale within each hyperfine manifold (but visual spacings should not be compared between manifolds or to the optical splitting). The approximate Landé g_F-factors for each level are also given, with the corresponding Zeeman splittings between adjacent magnetic sublevels. Included, with respect to [22], are the crossover transitions indicated by the dashed lines. The transitions used for the diode lasers in the experiment are indicated by Cool, Reference and Re-pump.

Appendix B Optical conveyor design

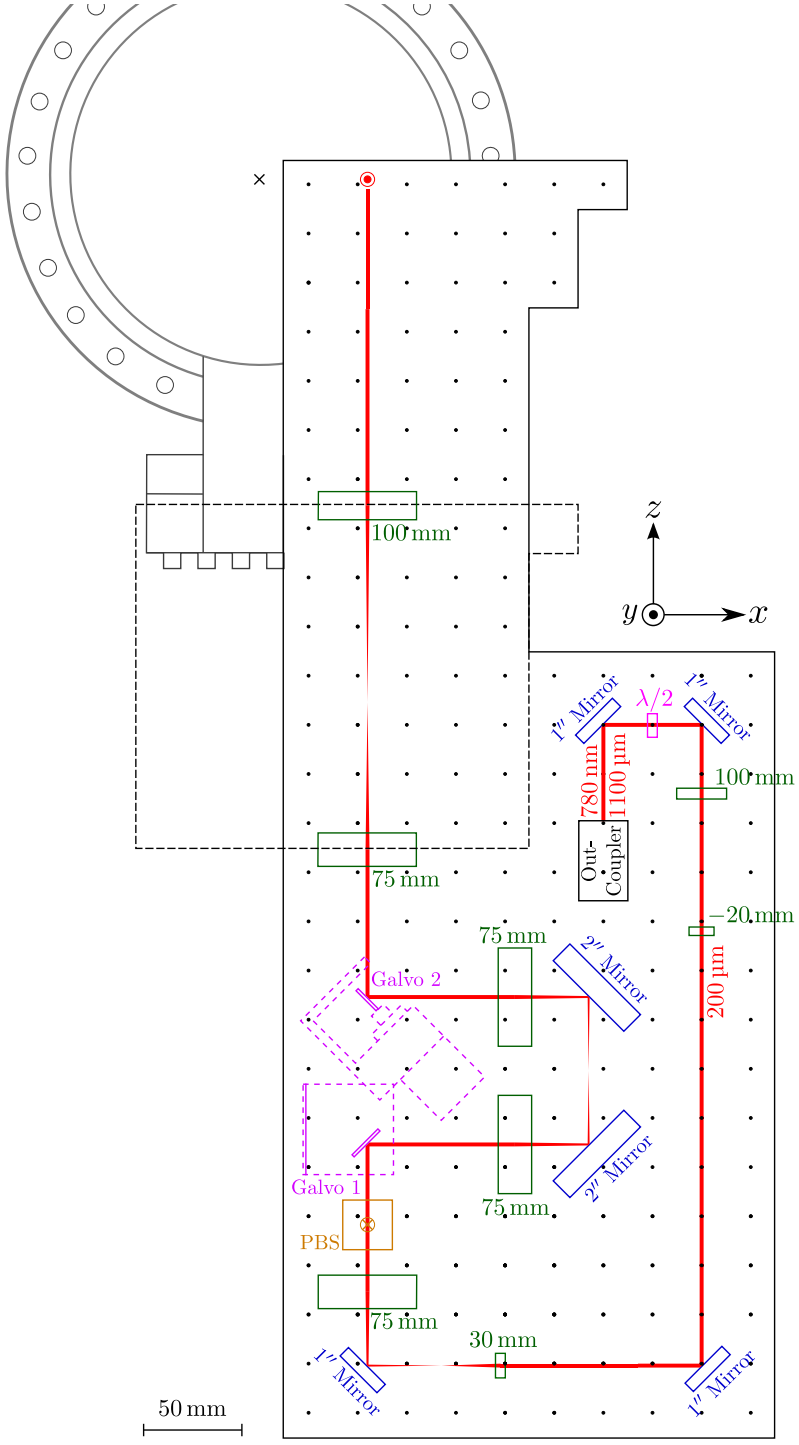

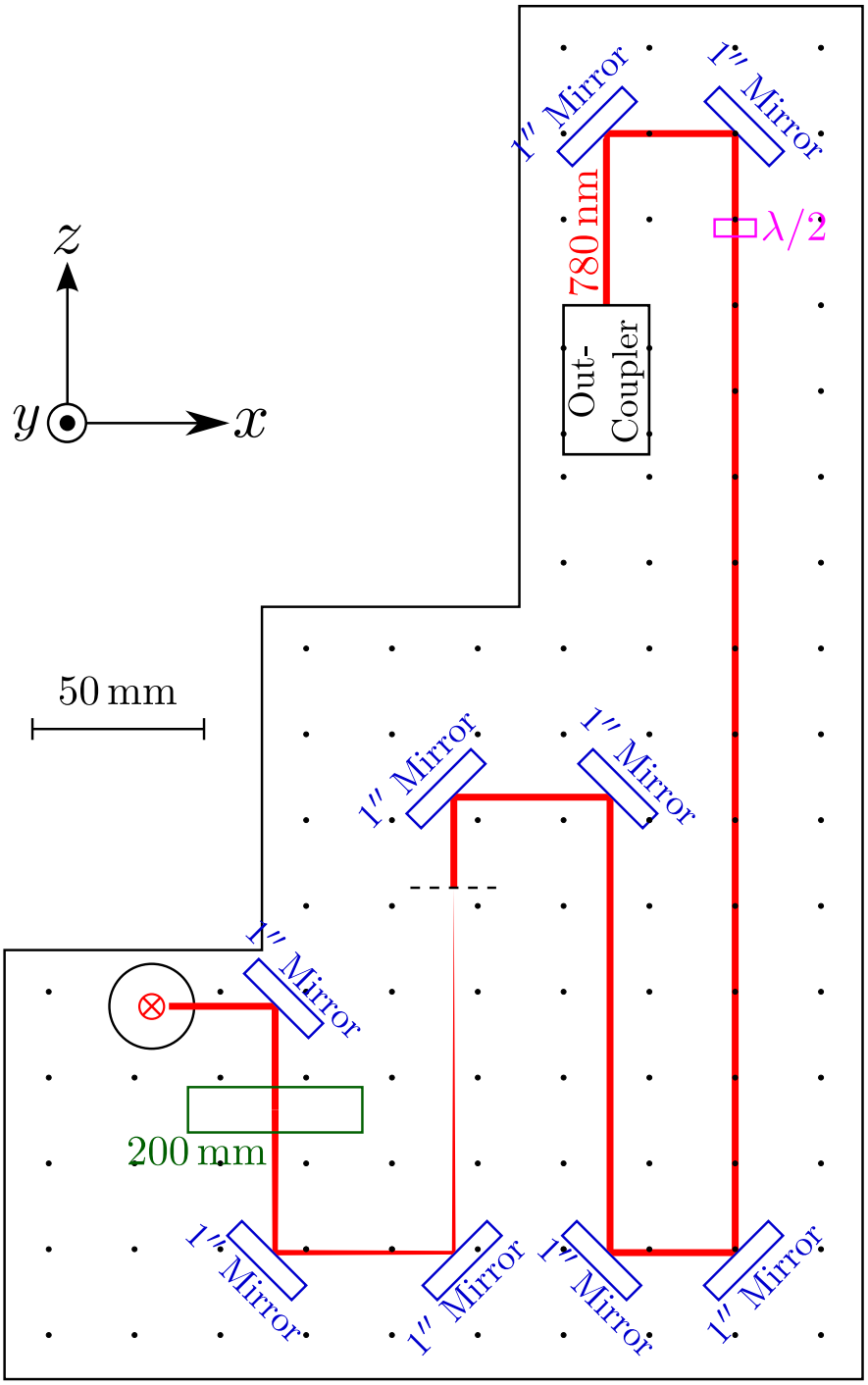
z
y
x
50 mm
1″ Mirror
1″ Mirror
780 nm
λ/2
Out-
Coupler
1″ Mirror
1″ Mirror
1″ Mirror
200 mm
1″ Mirror
1″ Mirror
1″ Mirror
1″ Mirror

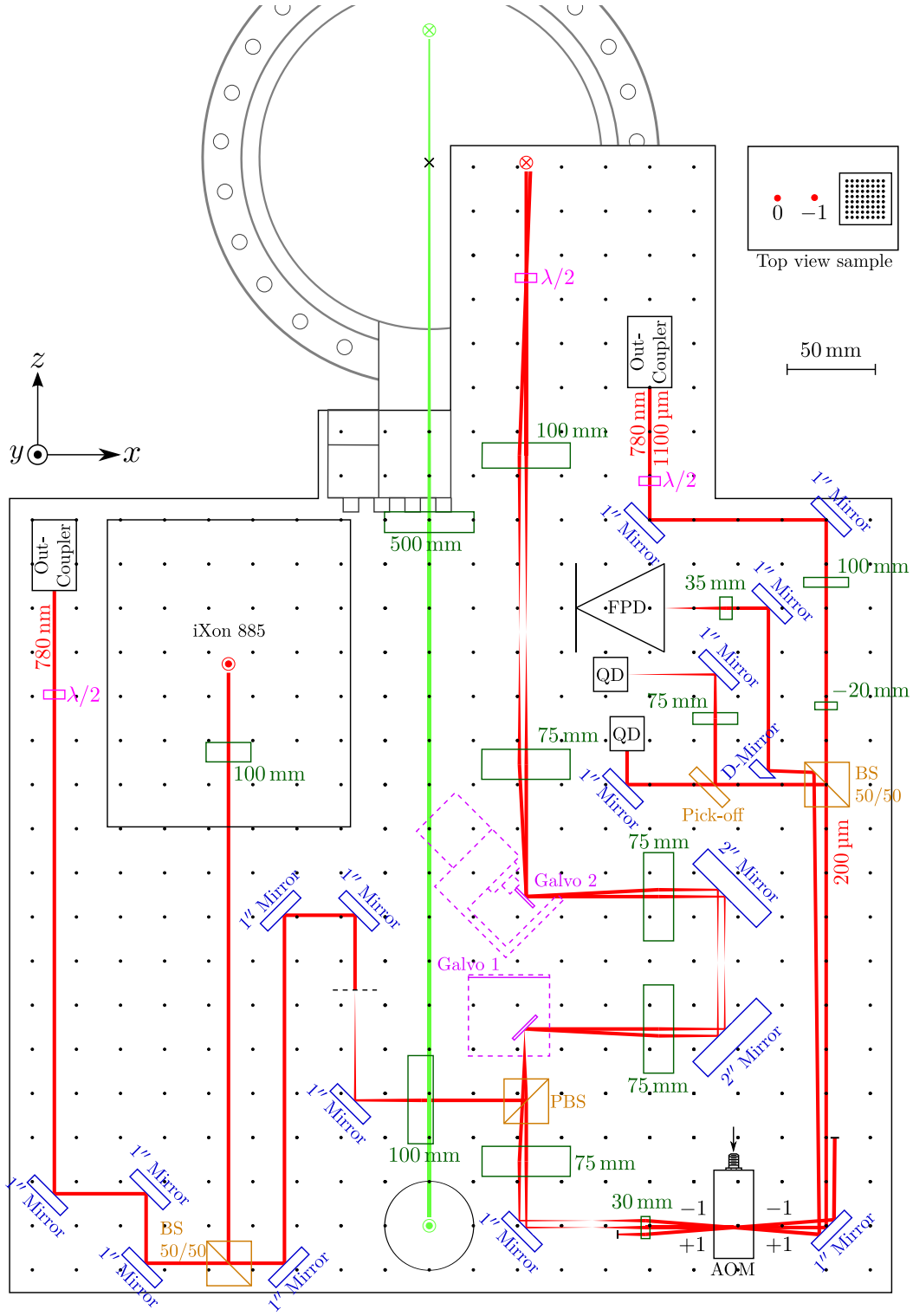
0
−1
Top view sample
50 mm
z
y
x
λ/2
Out-Coupler
780 nm
1100 µm
100 mm
500 mm
1″ Mirror
35 mm
FPD
QD
75 mm
−20 mm
D-Mirror
BS 50/50
Pick-off
200 µm
2″ Mirror
iXon 885
Galvo 2
Galvo 1
PBS
30 mm
AOM
+1
−1

References

[1] M. I. Stockman, *Nanoplasmonics: past, present, and glimpse into future*, Opt. Express **vol. 19**, no. 22, pp. 22029–22106 (2011)

[2] J. Prangsma, *Local and dynamic properties of light interacting with subwavelength holes*, Ph.D. thesis, University of Twente, Enschede (2009)

[3] E. A. Cornell and C. E. Wieman, *Bose-Einstein condensation in a dilute gas: The first 70 years and some recent experiments (Nobel lecture)*, ChemPhysChem **vol. 3**, no. 6, pp. 476–493 (2002)

[4] S. Chu, J. Bjorkholm, A. Ashkin, and A. Cable, *Experimental Observation of Optically Trapped Atoms*, Phys. Rev. Lett. **vol. 57**, no. 3, pp. 314–317 (1986)

[5] M. I. Stockman, *Nanoplasmonics: The physics behind the applications*, Physics Today **vol. 64**, no. 2, pp. 39–44 (2011)

[6] J. S. Donner, S. A. Thompson, C. Alonso-Ortega, J. Morales, L. G. Rico, S. I. C. O. Santos, and R. Quidant, *Imaging of Plasmonic Heating in a Living Organism*, ACS Nano **vol. 7**, no. 10, pp. 8666–8672 (2013)

[7] T. W. Hänsch and A. L. Schawlow, *Cooling of Gases by Laser Radiation*, Optics Communications **vol. 13**, no. 1, pp. 68–69 (1975)

[8] S. Chu, L. Hollberg, J. E. Bjorkholm, A. Cable, and A. Ashkin, *Three-Dimensional Viscous Confinement and Cooling of Atoms by Resonance Radiation Pressure*, Phys. Rev. Lett. **vol. 55**, no. 1, pp. 48–51 (1985)

[9] A. Ashkin, *Acceleration and Trapping of Particles by Radiation Pressure*, Phys. Rev. Lett. **vol. 24**, no. 4, pp. 156 – 159 (1970)

[10] K. M. O'Hara, S. L. Hemmer, M. E. Gehm, S. R. Granade, and J. E. Thomas, *Observation of a Strongly Interacting Degenerate Fermi Gas of Atoms*, Science **vol. 298**, no. 5601, pp. 2179–2182 (2002)

[11] C. Monroe, *Quantum information processing with atoms and photons*, Nature **vol. 416**, no. 6877, pp. 238–246 (2002)

[12] J. P. Burke, S.-T. Chu, G. W. Bryant, C. J. Williams, and P. S. Julienne, *Designing neutral-atom nanotraps with integrated optical waveguides*, Phys. Rev. A **vol. 65**, no. 4, p. 043411 (2002)

[13] L. Karssen, *Trapping cold atoms with ultrashort laser pulses*, Ph.D. thesis, University of Utrecht, Utrecht (2008)

[14] H. Metcalf and P. van Der Straten, *Cooling and Trapping of Neutral Atoms*, Physics Report **vol. 244**, no. 4-5, pp. 203–286 (1994)

[15] H. Metcalf and P. van Der Straten, *Laser Cooling and Trapping*, Springer-Verlag New York, Inc. (1999)

[16] H. J. Metcalf and P. van der Straten, *Laser Cooling and Trapping of Atoms*, Journal of the Optical Society of America B: Optical Physics **vol. 20**, no. 5, pp. 887–908 (2003)

[17] R. Grimm, M. Weidemüller, and Y. B. Ovchinnikov, *Optical Dipole Traps for Neutral Atoms*, Advances in Atomic, Molecular and Optical Physics **vol. 42**, no. C, pp. 95–170 (2000)

[18] D. Schrader, S. Kuhr, W. Alt, M. Müller, V. Gomer, and D. Meschede, *An optical conveyor belt for single neutral atoms*, Applied Physics B **vol. 73**, no. 8, pp. 819–824 (2001)

[19] W. Alt, D. Schrader, S. Kuhr, M. Müller, V. Gomer, and D. Meschede, *Single atoms in a standing-wave dipole trap*, Phys. Rev. A **vol. 67**, no. 3, p. 033403 (2003)

[20] Y. Miroshnychenko, W. Alt, I. Dotsenko, L. Förster, M. Khudaverdyan, D. Meschede, D. Schrader, and A. Rauschenbeutel, *An atom-sorting machine*, Nature **vol. 442**, no. 7099, p. 151 (2006)

[21] Z. Kluit, *A stereo-tweezer for ultracold atoms*, Master thesis, University of Utrecht, Utrecht (2013)

[22] D. A. Steck, *Rubidium 87 D Line Data*, available online at `http://steck.us/alkalidata` (revision 2.1.4, December 23, 2010). Accessed June 13, 2013

[23] W. T. Silfvast, *Laser Fundamentals*, Cambridge University Press, 2nd ed. (2004)

[24] D. J. Griffiths, *Introduction to Qauntum Mechanics*, Pearson Education, Inc. (2005)

[25] D. J. Griffiths, *Introduction to Electrodynamics*, Pearson Education, Inc. (2008)

[26] V. N. Mahajan, *Uniform versus Gaussian beams: a comparison of the effects of diffraction, obscuration, and aberrations*, J. Opt. Soc. Am. A **vol. 3**, no. 4, pp. 470–485 (1986)

[27] P. Belland and J. P. Crenn, *Changes in the characteristics of a Gaussian beam weakly diffracted by a circular aperture*, Appl. Opt. **vol. 21**, no. 3, pp. 522–527 (1982)

[28] S. L. Meyer Viol, *An optical dipole trap for transport of ^{87}Rubidium atoms*, Master thesis, University of Utrecht, Utrecht (2013)

[29] G. Reinaudi, T. Lahaye, Z. Wang, and D. Guéry-Odelin, *Strong saturation absorption imaging of dense clouds of ultracold atoms*, Opt. Lett. **vol. 32**, no. 21, pp. 3143–3145 (2007)

[30] D. A. Smith, S. Aigner, S. Hofferberth, M. Gring, M. Andersson, S. Wildermuth, P. Krüger, S. Schneider, T. Schumm, and J. Schmiedmayer, *Absorption imaging of ultracold atoms on atom chips*, Opt. Express **vol. 19**, no. 9, pp. 8471–8485 (2011)

[31] G. O. Konstantinidis, M. Pappa, G. Wikstrm, P. Condylis, D. Sahagun, M. Baker, O. Morizot, and W. Klitzing, *Atom number calibration in absorption imaging at very small atom numbers*, Central European Journal of Physics **vol. 10**, no. 5, pp. 1054–1058 (2012)

[32] D. van Oosten, *Quantum Gases in Optical Lattices: the Atomic Mott Insulator*, Ph.D. thesis, University of Utrecht, Utrecht (2004)

[33] H. D. Young and R. A. Freedman, *University Physics*, Pearson Education, Inc., 12th ed. (2008)

[34] J. R. Taylor, *An introduction to Error Analysis*, University Science Books (1997)

[35] Thorlabs, Hans-Boeckler-Straße 6, 85221 Dachau, Germany, *PDA36A Si Switchable Gain Detector, User Guide* (2012)

[36] S. J. M. Kuppens, K. L. Corwin, K. W. Miller, T. E. Chupp, and C. E. Wieman, *Loading an optical dipole trap*, Phys. Rev. A **vol. 62**, no. 1, p. 013406 (2000)

[37] M. Schulz, *Tightly confined atoms in optical dipole traps*, Ph.D. thesis, University of Innsbruck, Innsbruck (2002)

[38] C. J. Pethick and H. Smith, *Bose-Einstein Condensation in Dilute Gases*, Cambridge University Press, 2nd ed. (2008)

[39] J. R. Taylor, *Classical Mechanics*, University Science Books (2005)

[40] L. Visser, *Controlling an optical conveyor for neutral atoms*, Bachelor thesis, University of Utrecht, Utrecht (2012)

[41] B. R. Boruah and M. A. A. Neil, *Laser scanning confocal microscope with programmable amplitude, phase, and polarization of the illumination beam*, Review of Scientific Instruments **vol. 80**, no. 1, 013705 (2009)

[42] K. Arnold and M. Barrett, *All-optical Bose-Einstein condensation in a* $1.06\,\mu m$ *dipole trap*, Optics Communications **vol. 284**, no. 13, pp. 3288 – 3291 (2011)